อิทธิพลของชั้นแทรกแบบบางที่มีผลต่อโครงสร้างนาโนจาก InP

ที่ปลูกด้วย MBE และ MOVPE

นางสาวโซ โซ ฮาน

ศูนย์วิทยทรัพยากร
จุฬาลงกรณ์มหาวิทยาลัย

วิทยานิพนธ์นี้เป็นส่วนหนึ่งของการศึกษาตามหลักสูตรปริญญาวิศวกรรมศาสตรดุษฎีบัณฑิต
สาขาวิชาวิศวกรรมไฟฟ้า ภาควิชาวิศวกรรมไฟฟ้า
คณะวิศวกรรมศาสตร์ จุฬาลงกรณ์มหาวิทยาลัย
ปีการศึกษา 2553

ลิขสิทธิ์ของจุฬาลงกรณ์มหาวิทยาลัย

THE EFFECT OF THIN INSERTION LAYER ON INP NANOSTRUCTURES
BY USING MBE AND MOVPE

Miss Soe Soe Han

ศูนย์วิทยทรัพยากร
จุฬาลงกรณ์มหาวิทยาลัย

A Dissertation Submitted in Partial Fulfillment of the Requirements
for the Degree of Doctor of Philosophy Program in Electrical Engineering
Department of Electrical Engineering
Faculty of Engineering
Chulalongkorn University
Academic Year 2010
Copyright of Chulalongkorn University

Thesis Title	THE EFFECT OF THIN INSERTION LAYER ON INP NANOSTRUCTURES BY USING MBE AND MOVPE
By	Miss Soe Soe Han
Field of Study	Electrical Engineering
Thesis Advisor	Associate Professor Somchai Ratanathammaphan, D.Eng.
Thesis Co-advisors	Professor Somsak Panyakeow, D.Eng.
	Professor Yoshiaki Nakano, Ph.D.

Accepted by the Faculty of Engineering, Chulalongkorn University in Partial Fulfillment of the Requirements for the Doctoral Degree

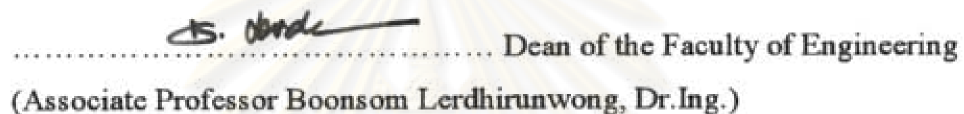
.... Dean of the Faculty of Engineering

(Associate Professor Boonsom Lerdhirunwong, Dr.Ing.)

THESIS COMMITTEE

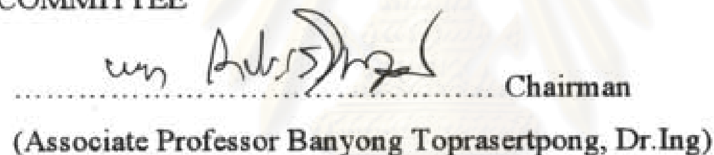
.... Chairman

(Associate Professor Banyong Toprasertpong, Dr.Ing)

.... Thesis Advisor

(Associate Professor Somchai Ratanathammaphan, D.Eng.)

.... Thesis Co-advisor

(Professor Somsak Panyakeow, D.Eng.)

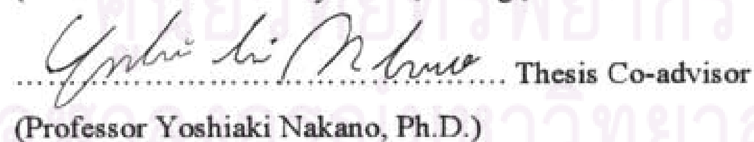
.... Thesis Co-advisor

(Professor Yoshiaki Nakano, Ph.D.)

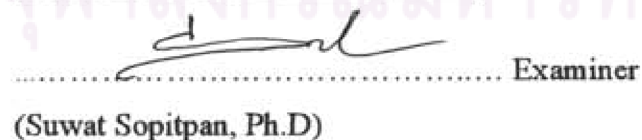
.... Examiner

(Suwat Sopitpan, Ph.D)

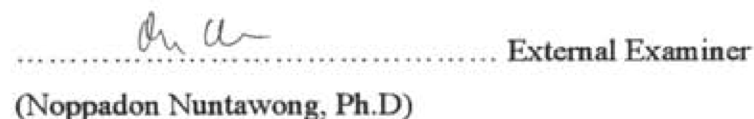
.... External Examiner

(Noppadon Nuntawong, Ph.D)

ศูนย์วิทยทรัพยากร
จุฬาลงกรณ์มหาวิทยาลัย

ไช ไช สาน : อิทธิพลของชั้นแทรกแบบบางที่มีผลต่อโครงสร้างนาโนจาก InP ที่ปลูกด้วย MBE และMOVPE. (THE EFFECT OF THIN INSERTION LAYER ON INP NANOSTRUCTURES BY USING MBE AND MOVPE) อ. ที่ปรึกษาวิทยานิพนธ์หลัก: รศ. ดร.สมชัย รัตนธรรมพันธ์, อ. ที่ปรึกษาวิทยานิพนธ์ร่วม: ศ.ดร.สมศักดิ์ ปัญญาแก้ว, อ.ที่ปรึกษาวิทยานิพนธ์ร่วม: Professor Yoshiki Nankano, 143 หน้า.

วิทยานิพนธ์นี้ได้ทำการศึกษาอิทธิพลของชั้นแทรก GaP และ InGaP ที่มีต่อคุณสมบัติทางโครงสร้างและทางแสงของควอนตัมดอตจาก InP ที่เกิดจากการก่อตัวขึ้น โดยตัวอย่างในการนี้ได้จากวิธีการปลูกผลึกอิพิแทกซีจากลำโมเลกุลและวิธีการปลูกผลึกจากสถานะไอของสารประกอบโลหะอินทรีย์โดยตัวอย่างที่ได้ถูกนำมาวิเคราะห์ลักษณะโครงสร้างด้วยกล้องจุลทรรศน์แรงอะตอมซึ่ง ผลของชั้นแทรกมีผลทำให้ขนาดของควอนตัมดอตมีขนาดเล็กลงและทำให้ค่าความหนาแน่น มีค่าลดลง เนื่องจากชั้นแทรกมีค่าคงตัวผลึกเล็กกว่าค่าคงตัวผลึกของ InP ที่เป็นควอนตัมดอทและ GaAs เป็นแผ่นฐาน โดยความเครียดที่เกิดในชั้นแทรกมีลักษณะเป็นแรงดึง ซึ่งมีลักษณะตรงข้ามกับความเครียดที่เกิดขึ้นในควอนตัมดอต ผลจากลักษณะของความเครียดที่เกิดในชั้นแทรกและ ควอนตัมดอตที่แตกต่างกันอันเป็นผลให้ ขนาดและค่าความหนาแน่นของควอนตัมดอตที่ได้ แตกต่างไปจากตัวอย่างที่มีค่าความหนาชั้นแทรกแตกต่างๆ กัน ซึ่งผลนี้ได้แสดงออกในผลการวัด โฟโตลูมิเนสเซนซ์ที่สอดคล้องกับ การเปลี่ยนแปลงที่เกิดขึ้นและค่าความหนาของชั้นแทรกที่เหมาะสมนั้นขึ้นกับค่าสัดส่วน In ในชั้นแทรก InGaP

ภาควิชา ......วิศวกรรมไฟฟ้า........... ลายมือชื่อนิสิต ....

สาขาวิชา ......วิศวกรรมไฟฟ้า.......... ลายมือชื่อ อ.ที่ปรึกษาวิทยานิพนธ์หลัก..............

ปีการศึกษา ....2553.................. ลายมือชื่อ อ.ที่ปรึกษาวิทยานิพนธ์ร่วม ....

ลายมือชื่อ อ.ที่ปรึกษาวิทยานิพนธ์ร่วม..............

ศูนย์วิทยทรัพยากร จุฬาลงกรณ์มหาวิทยาลัย

5071877121 : MAJOR ELECTRICAL ENGINEERING
KEYWORDS : INP SELF-ASSEMBLED QUANTUM DOTS, INSERTION LAYER, MOLECULAR BEAM EPITAXY, METAL ORGANIC VAPOR PHASE EPITAXY, ATOMIC FORCE MICROSCOPY, PHOTOLUMINESCENCE

SOE SOE HAN : THE EFFECT OF THIN INSERTION LAYER ON INP NANOSTRUCTURES BY USING MBE AND MOVPE. ADVISOR : ASSOC. PROF. SOMCHAI RATANATHAMMAPHAN, D.Eng., CO-ADVISORS : PROF. SOMSAK PANYAKEOW, D.Eng., PROF. YOSHIAKI NAKANO, Ph.D, 143 pp.

The effect of GaP and InGaP insertion layers on self-assembled InP quantum dots are presented and discussed, together with their growth, structural and optical properties. In the growth of InP/InGaP/GaAs self-assembled quantum dots (SAQDs), eventhough the bimodal size distribution for the coherent islands can be overcome by using GaP and InGaP insertion layers, the island size is still large and the areal density of dots is low. Since large dots may introduce dislocations and low density leads to poor optical efficiency, growth of small size, high density and uniformity of InP dots becomes imperative. Under the proper growth conditions, formation of InP QDs via the Stranski-Krastanow mechanism is observed. The critical InP coverage for insertion of GaP layer is found to be 3 ML for the InP/ $In_{0.48}Ga_{0.52}P$/GaAs system in MBE growth system and 4 ML for the InP/ $In_{0.49}Ga_{0.51}P$/GaAs system in MOVPE system. The structural characterization from atomic force microscopy (AFM) measurements indicates that the MBE growth of InP/ $In_{0.48}Ga_{0.52}P$ QDs are larger and, consequently, more dense compared to the MOVPE growth of InP/ $In_{0.49}Ga_{0.51}P$ QDs. By observing photoluminescence (PL) from InP quantum, the PL peak wavelength is continuously reduced between 770 and 810 nm with increase of the GaP and InGaP insertion layers thickness. This red spectral range is also preferable to generate highest photon detection efficiency for single-photon detectors. Additionally, the InP QDs with GaP and InGaP ILs must influence the optical properties of possible quantum optic devices which have to be carried out in future work.

Department:.......Electrical Engineering............ Student's Signaure ....
Field of Study:...Electrical Engineeing ....Advisor's Signature ....
Academic Year:.......2010.............................Co-Advisor's Signature ....
Co-Advisor's Signature ....

ศูนย์วิทยทรัพยากร
จุฬาลงกรณ์มหาวิทยาลัย

Acknowledgements

Firstly and most importantly, I would like to express my deepest thanks to my advisor, Assoc. Prof. Dr. Somchai Ratanathammaphan and co-advisor, Prof. Somsak Panyakeow for encouragement, guidance and support throughout the duration of my Ph.D program. I specially appreciate the help from Ms. Wipakorn Jewasuwan, Mr. Poonyasiri Boonpeng, Ms. Naraporn Pankaow and Ongarj Tangmattajittakul, who gave me the trainings, intrigued the discussion, and showed me support at the hard times.

I would like to pass my deeply appreciation straightforward to Prof. Dr. Yoshiaki Nakano for his acceptance for being my co-advisor and for his plenty of generous supports to do research in Tokyo University. Many people from this lab provided critical support, including Assoc. Prof. Masakazu Sugiyama, Assist. Prof. Akio Higo, Ms. Momoko Deura. I would really like to acknowledge valuable discussions, advice and help from Dr. Wang Yunpeng. His knowledge and insights have propelled my learning.

I would like to say thanks to all my teachers and technical assistants from SDRL for their teaching, discussions and valuable advices. I would also thank my committee members, Assoc. Prof. Dr. Banyong Toprasertpong, Dr. Suwat Sopitaphan and Dr. Noppadon Nantawong for reading and commenting on my dissertation. I would like to acknowledge financial support from Japan Cooperation Agency Office for South East Asia Engineering Education Development Network of Asean University Network (AUN/SEED-NET), Asian Office for Aerospace Research and development (AOARD), Thailand Research Fund (TRF), Nanotech center (NANOTEC), Chulalongkorn University, University of Tokyo and Higher Education Research Promotion and National Research University Project of Thailand, Office of the Higher Education Commission (EN264A).

Finally, I owe a debt of gratitude to all the current and former teachers, students and staffs that I have interacted with, but I mention by name only those who contributed most directly to the work reported in this thesis. This dissertation is dedicated to my family for all their support and encouragement, motivating me to become Ph.D that I am. I thank you all.

CONTENTS

Page

Abstract (Thai) iv

Abstract (English) v

Acknowledgements vi

Contents vii

List of Tables xi

List of Figures xii

List of Symbols xviii

Chapter I : Introduction. 1

1.1 Background 1

1.2 Objectives 4

1.3 Research Methodology 5

1.4 Overview 6

Chapter II : Theoretical Overview of Self-Assembled Nanostructures 8

2.1 The Mechanism of Quantum Confinement in Semiconductors 8

2.1.1 Bulk Material 8

2.1.2 Quantum Wells 9

2.1.3 Quantum Wires 9

2.1.4 Quantum Dots 10

2.1.5 Summary of Quantum Confinement Effects 12

2.2 Applications of Quantum Dots 15

2.3 Synthesis Methods of Quantum Dots 18

2.3.1 Epitaxial Growth Techniques 18

2.3.2 Colloidal Synthesis of Quantum Dots 20

2.4 Nanostructures by Self-Assembling 20

2.4.1 Self-Assembled Growth 20

2.4.1.1 Stranski-Krastanow Mode 22

2.4.1.2 Materials Consideration in S-K Mode 25

2.4.1.3 Size and Morphology of S-K Islands 26

2.4.2 Theory of Self-Assembled QDs Formation 27

Page

2.4.2.1 Thermodynamic Analysis 28

2.4.2.2 Kinetic Analysis 32

2.5 Defects and Dislocations 33

2.5.1 Strain 33

2.5.2 Defects and Stress 37

2.5.2.1 Defect Classification 37

2.5.2.2 Point Defects 40

2.5.2.3 Line Defects 40

2.5.2.4 Planar and Volume Defects 42

2.5.2.5 Stress by Misfit Dislocations 43

2.5.2.6 Stress by thermal expansion mismatch 44

2.5.3 Dislocations 45

2.5.3.1 Critical Thickness for $In_xGa_{1-x}P$ Growth on GaAs 46

2.5.3.2 Types of Misfit Dislocations 47

2.5.3.3 Surface Steps via Threading Dislocation 48

2.5.3.4 Lomer Type Misfit Dislocation 50

2.6 Growth Techniques 51

2.6.1 Multi Steps Technique 51

2.6.2 In-Interruption Growth Technique 52

2.6.3 Thin-Cap and Regrowth Technique 53

2.6.4 Atomic Force Tip-Induced Nano-Oxidation, Atomic - Hydrogen Etching/Cleaning and Regrowth Technique 54

Chapter III : Self-Assembled Quantum Dots Growth and Characterization Techniques 56

3.1 Self-Assembly by Molecular-Beam Epitaxy 56

3.1.1 Basics of Molecular-Beam Epitaxy 56

3.1.2 Molecular Beam Epitaxy (MBE) System Overview 58

3.1.3 In-Situ Characterization Tools 61

3.1.3.1 Mass Spectroscopy (An introduction to Mass Spectroscopy, Ashcroft) 61

ศูนย์วิทยทรัพยากร
จุฬาลงกรณ์มหาวิทยาลัย

Page

3.1.3.2 Reflection High-Energy Electron Diffraction (RHEED) ... 63
3.2 Metal-Organic Vapor Phase Epitaxy ... 65
3.2.1 MOVPE System Overview ... 65
3.2.2 MOVPE Growth Mechanism ... 69
3.2.2.1 Metal-organic precursors ... 73
3.2.2.2 Growth Calibration ... 76
3.2.2.3 Effect of Growth Temperature ... 78
3.2.3 Comparison of MBE and MOVPE ... 79
3.3 Atomic Force Microscopy (AFM) ... 82
3.4 Photoluminescence (PL) ... 84

Chapter IV : Synthesis and Characterization of InP Nanostructures ... 89
4.1 Properties of InP semiconductor compounds ... 89
4.2 Structural and Optical Properties of Quantum Dots ... 90
4.2.1 Size, Shape, Homogeneity and Density ... 91
4.2.2 Optical Properties ... 92
4.3 Effect of Insertion Layers on InP Nanostructures ... 93
4.3.1 GaP Insertion Layer ... 93
4.3.2 InGaP Insertion Layer ... 94
4.4 Effect of GaP Insertion Layer on Structural Characterization of $InP/In_{0.48}Ga_{0.52}P/GaAs$ System by MBE ... 95
4.5 $InP/In_{0.49}Ga_{0.51}P/GaAs$ System by MOVPE ... 99
4.5.1 Effect of GaP Insertion Layer ... 100
4.5.1.1 Structural Characterization ... 100
4.5.1.2 Optical Characterization ... 104
4.5.2 Influence of Growth Parameters on InP QDs by MOVPE ... 109
4.5.2.1 Evolution of InP QDs formation by changing QDs Growth Temperature ... 109
4.5.2.2 Evolution of InP QDs formation by changing III-V Ratio and Growth Rate ... 112
4.5.3 Effect of InGaP Insertion Layer ... 114

Page

4.5.3.1 Structural Characterization 114

4.5.3.2 Optical Characterization 121

Chapter V : Conclusions 130

References 134

Vitae 143

LIST OF TABLES

Page

Table 2.1 Parameters for common semiconductor materials at or near room temperature 47

Table 3.1 Basic Parameters of MOVPE Sources 67

Table 3.2 Comparison between MBE and MOVPE 81

Table 4.1 Some Parameters of P and As based semiconductors compound.............. 90

Table 4.2 The parameters of the samples grown with different temperatures 110

Table 4.3 The parameters of the samples grown with different growth rate and V/III ratio 114

ศูนย์วิทยทรัพยากร
จุฬาลงกรณ์มหาวิทยาลัย

LIST OF FIGURES

		Page
Figure 2.1	Illustration of type I and II quantum well	9
Figure 2.2	Schematic views and graphs of (a) bulk, (b) quantum wells, (c) quantum wires and (d) quantum dots and their density of states (D.O.S)	13
Figure 2.3	Schematic representation of the three crystal growth modes of a film for a different coverage (θ) (a) layer-by-layer or Fran-van der Merwe (b) layerplus-island or Stranski-Krastanow mode island and (c) Volmer-Weber (Herman and Sitter, 1989)	21
Figure 2.4	Schematic representation of total energy change for a strained system in 2D and 3D growth modes. t_{cw} and t_{cd} are critical thicknesses for formation of islands and dislocations, respectively (Seifert et al., 1996)	23
Figure 2.5	Schematic of the total energy vs. time for the self-assembling process. Tc^{e}, and t^{c} are the thermodynamically and kinetically defined critical wetting layer thickness, E_E is the excess energy due to strain, and E_A the 2D-3D activation barrier. X is the point where a pure strain-induced transition becomes possible (no thermal activation)	24
Figure 2.6	Bandgap energy versus lattice constant of various III-V compound semiconductors at room temperature	25
Figure 2.7	Energy of an array of 3D coherently strained islands per one atom versus size of the atom. The control parameter α is the ratio of the surface energy and edge energy (Bimberg et al., 1999)	28
Figure 2.8	Equilibrium phase diagram of a lattice-mismatched heteroepitaxial system as a function of epilayer thickness H and the lattice mismatch. The small panels on the top and bottom illustrate the morphology of the surface in the six growth modes. The small empty triangles represent the presence of stable islands, while the large shaded area ones refer to ripened islands (Daruka and Barabási, 1997)	30
Figure 2.9	Schematic representation of the local strain energy density in and around the 3D island (Seifert et al., 1996)	33
Figure 2.10	Schematic representations of (a) unstrained layer, (b) compressive strained layer and (c) tensile strained layer. The opened squares represent atoms of the substrate materials and closed squares are atoms of the epitaxial materials. In (b) and (c) the lattice constants of epitaxial	

Page

	layers are different from the substrate materials. The arrows in (b) and (c) represent forces (stresses) exerted on the epitaxial layer	34
Figure 2.11	Diffraction peaks from (a) the epitaxial layer (at θ_e) and (b) the substrate (at θ_s)	35
Figure 2.12	Illustration of (a) 90 °edge dislocation and (b) 60º mixed dislocations	37
Figure 2.13	High-resolution TEM image of bonded interface of (001) InP and (001) GaAs	39
Figure 2.14	High-resolution TEM image of bonded interface of orientation-mismatched (001) GaP and (110) InP	39
Figure 2.15	Schematic diagram showing point defects in a crystal (Singh, 2003)	40
Figure2.16	Schematic representation of (a) edge dislocation and (b) screw dislocation http://en.wikipedia.org/wiki/Dislocation#Edge_dislocations)	41
Figure2.17	Dislocation geometry in heteroepitaxial mismatched thin films. (a) One of the inclined {111} planes for a (001) oriented fcc film/substrate system with a gliding TD segment and a trailing MD. (b) Dislocation Burgers (Andrew et al., 2002)	42
Figure 2.18	Burgers circuit (a) around a dislocation and (b) in a perfect crystal (Hull, 1965)	42
Figure 2.19	Atomic order of (113) InP and (001) GaAs: (a) top view, both (b) and (c) side view	43
Figure 2.20	Geometric of appearance of surface step via gliding of threading dislocation with Burger vector b (Hongland et al., 2004)	48
Figure 2.21	TEM images showing dislocation observed in GaAs/$In_{0.15}Ga_{0.85}As$/GaAs for various thicknesses (h) of InGaAs layers (a) misfit dislocation segment (h = 6 nm) (b) elongated misfit dislocation segment (15 nm) and (c) misfit dislocation network with threading dislocation (h=25 nm) (Liu et al., 1999)	49
Figure 2.22	(a) AFM and (b) TEM images of cross-hatch pattern for $In_{0.25}Ga_{0.75}As$/GaAs (001) (Yastrubchak et al., 2003)	49
Figure 2.23	TEM image showing V-shape configuration resulted from inclined slip loops originating in misfit dislocation network (Rajan et al., 1987)	49

		Page
Figure 2.24	Schematic drawing of the spatial dislocation configuration for the case of L-MD which is commonly found in pure edge MD (Vdovin, 1997)...	50
Figure 2.25	AFM image (300 nm×300 nm) of InGaAs QDs aligned multiatomic steps on GaAs (001) surface misoriented by 2° toward [101] direction (Kitamura et al., 1995)...	51
Figure 2.26	AFM image (a) of multiatomic steps on GaAs layer grown on a vicinal (111)B GaAs and (b) InGaAs islands by growing 3-nm-thick ...	52
Figure 2.27	(a) Schematic drawing of In-interruption growth technique and (b) AFM image (3000 nm×3000 nm) of InAs QDs with a In-interruption time 9 sec (Hong et al., 2006)...	53
Figure 2.28	AFM images of (a) nanohole (b) 1 cycle (c) 7 cycles of thin-cap and regrowth of QDs on nanoholes (Suwaree et al., 2006)...	54
Figure 2.29	The schematic illustration of the experimental processes for (a) the formation of the nano-oxide dots on GaAs (001) surface by AFM tip induced oxidation, (b) the subsequent removal of a nano-oxide dot and native oxide layer by atomic hydrogen irradiation and (c) the deposition of InAs QDs on nanoholes by droplet epitaxy ...	54
Figure 2.30	AFM images of (a) nano-oxide dots (b) nanoholes and (c) InAs QD arrays grown by droplet epitaxy (Kim et al., 2006)...	55
Figure 3.1	(a) MBE mechanism and (b) Schematic diagram of MBE process...	57
Figure 3.2	(a) Schematic diagram of the growth chamber of MBE system (b) A photograph of RIBER 32P MBE system ...	59
Figure 3.3	Temperature profile of the preheat process ...	60
Figure 3.4	Schematic diagram of the vertical layer structure of InP QDs embedded in InGaP barrier grown on (100) GaAs Substrate ...	61
Figure 3.5	A schematic diagram of mass spectrometer stev. (http//www.stev.gb.com/ science/spectroscopy.html)...	62
Figure 3.6	A schematic of RHEED observation system...	63
Figure 3.7	The RHEED pattern transition of temperature calibration of temperature calibration process of GaAs [110] azimuth (Ttransition (500 °C) = $(T_1+T_2+T_3+T_4) / 4$) ...	64
Figure 3.8	Photo of AIX 200/4 MOVPE system ...	66
Figure 3.9	Schematic configuration of MOVPE system used in this research ...	68
Figure 3.10	Photo of AIXTRON AIX200/4 reactor used in MOVPE system ...	70

Page

Figure 3.11 Schematic diagram of the vertical layer structure of InP QDs embedded in InGaP barrier grown on (001) GaAs Substrate by changing GaP insertion layers thickness 71

Figure 3.12 Schematic diagram of the vertical layer structure of InP QDs embedded in InGaP barrier grown on (001) GaAs Substrate by changing InGaP insertion layers thickness 72

Figure 3.13 Schematic diagram of the vertical layer structure of InP QDs grown on (001) GaAs substrate by insertion of InGaP layer 73

Figure 3.14 M-$(CH_3)_3$ structure (TMIn and TMGa)........ 74

Figure 3.15 MH_2 $C(CH_3)_3$ structure (TBA and TBP)........ 74

Figure 3.16 Top-view SEM images of $In_{0.5}Ga_{0.5}As$ /GaAs QDs grown at various growth temperatures: (a) 500 °C, (b) 520 °C and (c) 590 °C 79

Figure 3.17 A schematic of AFM measurement 82

Figure 3.18 (a) Modes of AFM measurement (b) Photo of AFM tip 83

Figure 3.19 Photo of Nano-R_2TM, Pacific Nanotechnology AFM Machine 83

Figure 3.20 Photo of SEIKO SPA 400-AFM Machine 84

Figure 3.21 Photo of room temperature photoluminescence setup used for the optical characterization of InP QDs 86

Figure 3.22 Optical design of the iHR320 spectrometer. [Adapted from iHR Fully Automated Imaging Spectrometer User Manual] 86

Figure 3.23 Schematic representation of the room temperature photoluminescence setup used for the optical characterization of InP QDs 87

Figure 3.24 Photo of low-temperature photoluminescence setup used for the optical characterization of InP QDs 88

Figure 3.25 Schematic representation of the low-temperature photoluminescence setup used for the optical characterization of InP QDs 88

Figure 4.1 Typical AFM images of InP QDs with diameter distribution histogram graph grown on (a) 0 ML (b) 1 ML (c) 2 ML (d) 3 ML (e) 4 ML GaP layers 97

Figure 4.2 Height distribution histograms of InP QDs grown on (a) 0 ML (b) 1 ML (c) 2 ML (d) 3 ML and (e) 4 ML GaP layers 98

Figure 4.3 InP QDs density plotted as a function of 0-4 ML GaP thickness 99

Figure 4.4 Typical (1μm × 1μm) scan range AFM images of InP QDs embedded in InGaP barrier with (a) 0 ML (b) 1 ML (c) 2 ML (d) 3 ML (e) 4 ML GaP layers 101

Page

Figure 4.5 Height distribution histograms of InP QDs on (a) 0 ML (b) 1 ML (c) 2 ML (d) 3 ML and (e) 4 ML GaP insertion layers 102

Figure 4.6 Effect of GaP insertion layer on QDs average size and density for InP SAQDs embedded in InGaP grown at 610 °C 103

Figure 4.7 The room temperature PL spectra of the InP QDs grown on the InGaP barrier with 0 – 4 ML thick GaP insertion layer between the InP QDs and the InGaP barrier 105

Figure 4.8 The Temperature dependent PL spectra of InP QDs at temperatures range 20-250 K with GaP insertion layers (a) 0 ML (b) 1 ML (c) 2 ML (d) 3 ML (e) 4 ML 106

Figure 4.9 Series of the PL spectra of InP QDs with 0-4 ML GaP insertion layers at temperatures range 150, 180 and 210 K 107

Figure 4.10 The evolution of the temperature dependence of the PL intensity for InP QDs with 0-4 ML GaP insertion layers 108

Figure 4.11 The PL emission wavelength as a function of GaP insertion layers thickness and temperature 108

Figure 4.12 The different growth temperature changes of InP QDs grown at (a) 475 °C (b) 500 °C (c) 550 °C 111

Figure 4.13 The different growth growth rate and V/III ratio changes changes of InP QDs grown at (a) 0.04 ML/s, 16 (b) 0.04 ML/s, 36 (c) 0.04 ML/s, 16.......... 113

Figure 4.14 Typical (1μm × 1μm) scan range AFM images and diameter histogram graph of InP QDs embedded in InGaP barrier with $In_{0.4}Ga_{0.6}P$ insertion layers (0-4) MLs 116

Figure 4.15 Height distribution histogram graph of InP QDs embedded in InGaP barrier with $In_{0.4}Ga_{0.6}P$ insertion layers (0-4) MLs 117

Figure 4.16 Effect of size and density of $In_{0.49}Ga_{0.51}P$ insertion layers on InP SAQDs embedded in InGaP grown at 610 °C 117

Figure 4.17 Typical (1μm × 1μm) scan range AFM images and diameter histogram graph of InP QDs embedded in InGaP barrier with $In_{0.4}Ga_{0.6}P$ insertion layers (0, 2, 4) MLs.......... 119

Figure 4.18 Height distribution histogram graph of InP QDs embedded in InGaP barrier before the growth of InP QDs 120

Figure 4.19 Effect of size and density of $In_{0.4}Ga_{0.6}P$ insertion layers on InP SAQDs embedded in InGaP grown at 610 °C.......... 120

Page

Figure 4.20 The room temperature PL spectra of the InP QDs grown on the $In_{0.49}Ga_{0.51}P$ barrier with 0- 4 ML thick $In_{0.4}Ga_{0.6}P$ insertion layers between GaP and InGaP layers 121
Figure 4.21 The Temperature dependent PL spectra of InP QDs at temperatures range 20-250 K with InGaP insertion layers (a) 0 ML (b) 1 ML (c) 2 ML (d) 3 ML (e) 4 ML 123
Figure 4.22 Series of the PL spectra of InP QDs with 0-4 ML InGaP insertion layers at temperatures range 150, 180 and 210 K 124
Figure 4.23 The evolution of the temperature dependence of the PL intensity for InP QDs with 0-4 ML InGaP insertion layers 124
Figure 4.24 The PL emission wavelengths as a function of InGaP insertion layers thickness and temperature 125
Figure 4.25 The room temperature PL spectra of the InP QDs grown on the $In_{0.49}Ga_{0.51}P$ barrier by insertion of 0, 2, 4 ML thick $In_{0.4}Ga_{0.6}P$ layers before the growth of InP QDs 126
Figure 4.26 The Temperature dependent PL spectra of InP QDs at temperatures range 20-250 K with InGaP insertion layers (a) 0 ML (b) 2 ML (c) 4 ML 127
Figure 4.27 Series of the PL spectra of InP QDs with 0, 2, 4 ML InGaP insertion layers at temperatures range 150, 180 and 210 K 127
Figure 4.28 The evolution of the temperature dependence of the PL intensity for InP QDs with 0, 2, 4 ML InGaP insertion layers. 128
Figure 4.29 The PL emission wavelengths as a function of InGaP insertion layers thickness and temperature 129

ศูนย์วิทยทรัพยากร
จุฬาลงกรณ์มหาวิทยาลัย

LIST OF SYMBOLS

MBE	molecular beam epitaxy
MOVPE	metal-organic vapor phase epitaxy
InP	indium phosphide
SAQD	self-assembled quantum dot
InGaP	indium gallium phosphide
GaP	gallium phosphide
InAs	indium arsenide
GaAs	gallium arsenide
LDs	laser diodes
LEDs	light emitting diodes
PL	photoluminescence
ILs	insertion layers
v	velocity
p	momentum
D	the density of states
k	electron wave number
QW	quantum wel
g(E)	the density of states
D.O.S	density of states
Er	the electric dipole operator
F	the electric field
QWL	quantum well laser
MLLs	mode-locked lasers
HEMTs	high-electron-mobility transistors
HBTs	hetero-bipolar-transistors
AlGaN	aluminium gallium nitride
LAVD	laser-assisted vapor deposition
MLs	monolayers
SK	Stranski-Krastanow
2D	two dimensions
3D	three dimensions

ศูนย์วิทยทรัพยากร
จุฬาลงกรณ์มหาวิทยาลัย

γ_f	the film surface energy
γ_i	the interface energy
$E\ (el)$	the elastic strain energy
λ	the elastic modulus
a	the lattice mismatch
A	the surface area
T	the film thickness
t_{cw}	the critical wetting layer thickness
t_{cd}	the critical thicknesses for formation dislocations
R	deposition rate
t_e^c	the equilibrium wetting layer thickness
t_c	the critical wetting layer thickness
E_E	the excess energy
$E_{elastic}$	elastic energy
E_{surf}	surface energy
E_{edge}	edge energy
L	base length
E_0	the characteristic energy
L_0	the length of the pyramid
α	the control parameter
MDs	misfit dislocations
h_c	a critical thickness
$a_{//}$	the parallel lattice constant
$a_{\perp}$	the perpendicular lattice constant
σ	a Poisson ratio
C_{11} , C_{12}	elastic constants of the epitaxial layer
ε	strain
b	Burgers vector length
ν	Poisson ratio
G	shear modulus
R	a height of the edge dislocation
F_{ED}	an edge dislocation affects,
σ_{ED}	dislocation stress
TDs	threading dislocations

RHEED	reflection high-energy electron diffraction
LPE	liquid-phase epitaxy
ClVPE	chloride vapor phase epitaxy
HVPE	hydride vapor phase epitaxy
TMGa	Trimethylgallium
TMIn	Trimethylindium
TBAs	Tertiarybuthylarsine
TBP	Tertiarybuthylphosphine
DMZn	Dimethylzinc
H_2S	Hydrogen Sulfide
AsH_3	Arsine
PH_3	Phosphine
H_2	hydrogen gas
SiH_4	Silane
DMZn	Di-methyl-zinc
GR	growth rate

CHAPTER I

Introduction

1.1 Background

Nanostructure science and technology is a broad and interdisciplinary area of research and development activity that has been growing explosively worldwide in the past decade years. It has the potential for evolution the ways in which materials and products are created and the range and nature of functionalities that can be accessed. A worldwide study of research and development status and trends in nanoparticles, nanostructure materials, and nano-devices (or more concisely, nanostructure science and technology) have been carried out in the past few years, since the realization that creating new materials and devices from nanoscale building blocks could access new and improved properties and functionalities **[1]**.

The new direction for semiconductor heterojunctions was first envisioned by Gubanov, Schokley and Herbert Kroemer more than fifty years before back in 1950's. However, the practical implementation of heterojunction devices was not reported until the development of new deposition techniques, first liquid phase epitaxy and then followed with molecular beam epitaxy (MBE) and metal-organic chemical vapor deposition (MOCVD). Film deposition by molecular beam technique was initiated by Cho in 1971 (Cho, 1971). In 1974, Raymond Dingle of Bell Laboratories demonstrated quantum confinement of charge carriers for the first time, and in 1979, Won-Tien Tsang, also of the Bell Labs, built the first semiconductor laser based on quantum confinement **[2]**. Since then, quantum well lasers have become the backbone of fiber optic communication systems. Quantum wire lasers were studied in the late eighties. However, the early works of Yasuhito Arakawa at Tokyo University in 1981 **[3]** and later of Mashahiro Asada at Tokyo Institute of Technology in 1986 **[4]** have shifted the interest of the optoelectronic community almost directly from quantum well to quantum dot lasers in search of better characteristics.

Advanced crystal growth, such as molecular beam epitaxy (MBE) or metal-organic vapor phase epitaxy (MOVPE), allows artificial III-V materials to be made using elaborate heterostructures needed for quantum devices. The development of the

physics and technology of semiconductor heterostructures has revolutionized modern day optoelectronics. Some of the devices that have resulted from semiconductor heterostructures include lasers, light emitting diodes, solar cells, and photodetectors **[5]**.

Instead of searching for the new materials for new applications and for new wavelength ranges in this technology, now one tries to use various combinations of materials, control their composition and thickness or synthesize new materials. Both lattice match and lattice mismatch pairs are now routinely grown and thus it is impossible to say which material combination has which specific properties and is useful in which application. After that scale consideration became significant role in fabrication history. Reducing the scale into nanometer scale exhibits the significant progress for device application. So semiconductor nanostructure became crucial in nowadays technology **[6]**.

Many efforts were spent on the realization of formation and physical properties of SAQDs for a variety of device applications like semiconductor lasers, infrared photo-detectors and quantum computation etc**.[7]**. One of the approaches that used to achieve single-photon generation is based on the emission of semiconductor QDs **[8]**. In the future, one can think of a simple QD device for computer or networking applications. For these purposes, optically or electrically addressable single QDs are needed on a mass production scale which favors metal-organic vapor-phase epitaxy (MOVPE) due to several advantages **[9]**. Current silicon based single-photon detectors have their highest photon detection efficiency in the red spectral range, therefore it is preferable to fabricate single QDs emitting at such wavelengths **[10]**. By using InP QDs embedded in $In_{0.49}Ga_{0.51}P$ emission in this spectral range can be achieved **[11]**. However, InP/InGaP SAQDs on GaAs are usually formed with poor size uniformity compared to that of InAs/GaAs QDs **[12]**. Especially, inhomogeneous broadening in optical spectra due to the randomness in the dot size has been a difficult issue of limiting potential benefits. While in the case MOVPE of InP/ InGaP SAQDs, a bimodal size distribution for the coherent islands has often been observed at low coverages of InP **[13]**. This bimodal size distribution can be overcome by the insertion of GaP and InGaP insertion layers **[14]**. Nevertheless, the island size still remain large and hence the areal density is low **[15]**. Since large dots may introduce misfit

dislocations and low areal density of dots gives poor optoelectronic efficiency, growth of small size, high density, and highly uniform InP/InGaP SAQDs becomes imperative **[16]**.

The size homogeneity and surface density of nanostructure dot ensemble should be high. The variation in size, shape and composition of self-assembled dots is dictated largely by random fluctuations during growth and typically gives rise to a Gaussian variation in the energy position of the electron and hole levels between dots. Finally, we require that the materials used are defect free, such as dislocations. Fortunately, self-assembled growth appears to provide the high material quality needed **[17]**.

Using the Stranski-Krastanow growth mode, the high quality QD ensembles may be grown from a large variety of material systems, for example, InP/GaInP, InAs/GaAs and Ge/Si **[18]**. This epitaxial method takes an advantage of the fact that an initially thin, strained 2-dimensional layer will, on reaching a critical thickness (typically 2 to 3 atomic layers), undergo a phase transition forming a dense collection of energetically favourable 3-dimensional islands (QDs) **[19]**. The driving force behind this transition is the resulting reduction in the total strain energy of the system. When compared with other fabrication methods, dots grown in this way exhibit the largest quantization effects, localization energies, and inter-sublevel energy spacing. Furthermore, such dots may be grown with surface densities greater than 10^{10} cm^{-2} and may be reliably produced **[20]**.

In this work, an interesting case of the growth of InP self-assembled quantum dots (QDs) on InGaP matrices by molecular beam epitaxy (MBE) and metal organic vapor phase epitaxy (MOVPE) on GaAs (100) substrates is observed the effect of insertion of a thin (a few ML thick) GaP and InGaP insertion layers on InP QDs. Research on InP and related compounds has been increasing exponentially in recent years. This is due to fact that InP is a key semiconductor for production of optoelectronic and photonic devices. In particular, InP and related compounds such as InGaAsP are key semiconductor materials for communications in the 1.3 and 1.55 μm special regions as well as for many other optoelectronic applications. The applications of InP and related materials have been extended to other areas that include laser diodes (LDs), light emitting diodes (LEDs), photodetectors, waveguides, photocathodes, and solar

cells **[21]**. In reality, high-speed Internet communication systems are now established wholeover the world based on these devices.

The aim of the research on InP quantum dots was to establish a technology to fabricate a three dimensional quantum dot composite material, a building block for future electronic and optoelectronic devices. The InP dots (islands) self-organize due to lattice mismatch of 3.8% between InP and InGaP. The shape and composition of InP SAQDs were visualized using a technique called Atomic Force Microscopy producing photographic images. Meanwhile, photoluminescence (PL) measurement was used to give valuable information about the optical properties of the InP/InGaP/GaAs structure.

In this contribution, the effects of the thin GaP and InGaP insertion layers on size, the areal density and the optical properties of the grown InP QDs were systematically studied. In the theoretical model of the S-K growth mode, QD growth depends both on the strain and the surface condition of the layer upon which the dots are grown **[22]**. Therefore, the insertion of GaP interface layers between $In_{0.49}Ga_{0.51}P$ matrix and InP QDs layer were also expected to change the morphology, growth characteristics and optical properties of the InP SAQDs. Otherwise, GaP tensile strained material on GaAs, had been reported to improve the structural and optical properties of InP QDs. The GaP and InGaP insertion layers also introduce strain relaxation effect important for growth monitoring, and simultaneously create opportunities in device processing based on InP/InGaP/GaAs system.

ศูนย์วิทยทรัพยากร
จุฬาลงกรณ์มหาวิทยาลัย

1.2 Objectives

The main objective of this work is to observe the effect of GaP and InGaP insertion layers on InP nanostructures grown by solid-source molecular beam epitaxy and metal organic vapor phase epitaxy.

The initial objective of this work is to fabricate self-organized InP quantum dots nanostructures on InGaP insertion layers via stranski-krastanow growth technique under different growth conditions especially by changing GaP and InGaP insertion layer thickness.

After the fabrication of InP nanostructures, the next objective is to investigate the effect of GaP and InGaP insertion layers on structural and optical properties of InP nanostructures by atomic force microscopy (AFM) and photoluminescence (PL).

1.3 Research Methodology

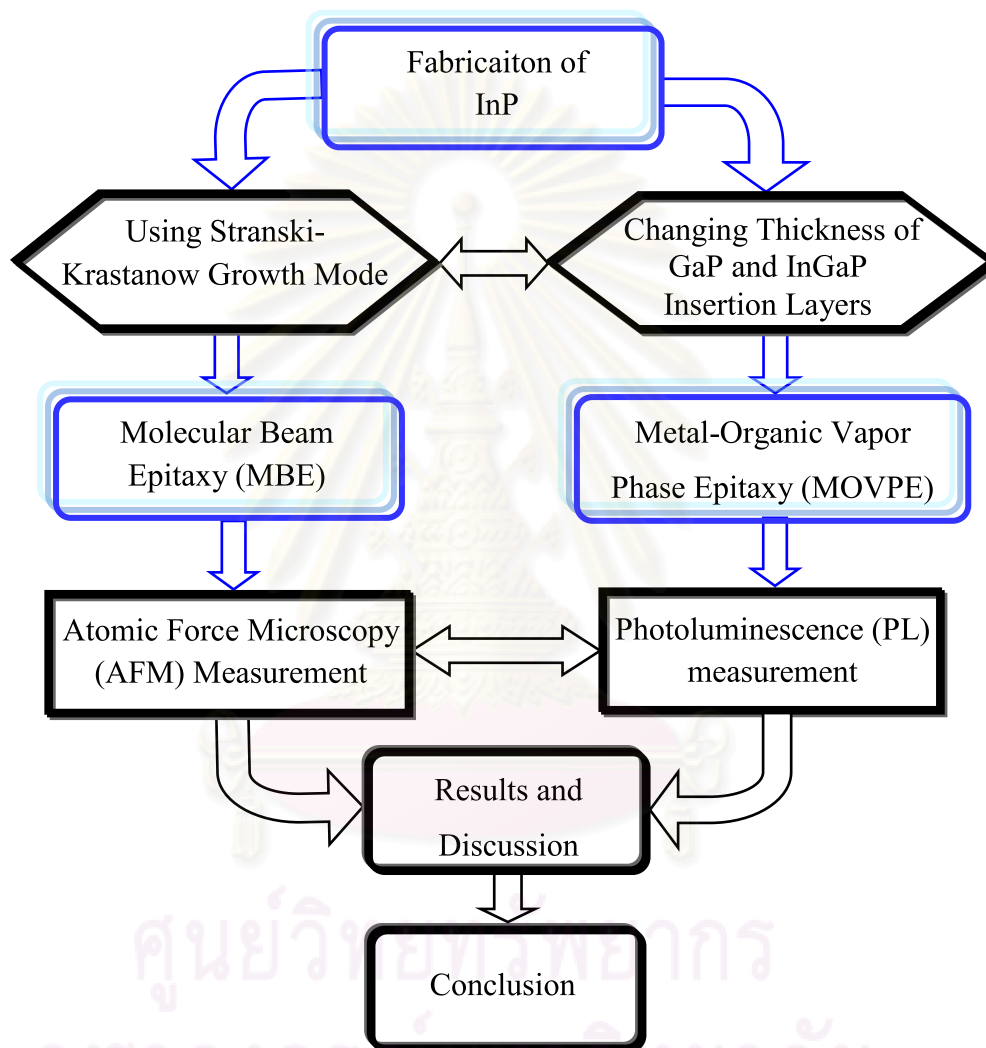

1.4 Overview

This dissertation is to present some approaches of improving the structural and optical properties of InP nanostructures by insertion of GaP and InGaP layers. The InP QDs are grown on GaAs (001) substrate by using RIBER 32P Molecular Beam Epitaxy (MBE) system and AIXTRON AIX200/4 Metal Organic Vapor Phase Epitaxy (MOVPE) system. After the fabrication of InP QDs, the structural and optical

properties of InP nanostructures aere characterized by using SEIKO SPA 400-AFM and Nano-R2^{TM}, Pacific Nanotechnology atomic force microscopy (AFM) machine and photoluminescence (PL) measurements by using the 532 nm line of solid state laser. The characterization of GaP and InGaP insertion layers on InP QDs was carried out from these results. The main goal of this research is to improve structural and optical properties of InP nanostructures by analyzing the effect of GaP and InGaP insertion layers.

The first chapter is meant to make the reader aware of the fact that it is necessary to introduce semiconductor nanostructures and background of nanotechnology. Apart from introduction, some other objective and research methodology were briefly mentioned. An overview of this thesis work is given.

In the second chapter, the reader will get acquainted with theoretical overview of the self-assembled nanostructure. It illustrates the quantum confinement effect, application of QDs, strain, defects, growth mechanism, growth mode and the capabilities of other important background for QDs formation in more details.

The third chapter will review the working principles of the MBE and MOVPE systems which is used to fabricate all the samples needed for this work in terms of the principle and the function of constituent components. The latter is a very important component organo-metallic sources and characterization techniques used for the growth of InP QDs. The working principle and measurement procedure for the instruments used in this work will also be described.

Then, the results concerning InP QDs by insertion of GaP and InGaP layers effects will be presented in chapter four. The effect of GaP and InGaP insertion layers on structural and optical properties of InP QDs will be discussed first. Also, some attention will be given to approach the influence of the other growth parameters such as temperature, growth rate and III/V ratio.

A final chapter will review the results obtained in the thesis and draw some conclusions. Furthermore, possible future improvements on our own work as well as an outlook into where InP nanostructures are headed will be given.

NO THIS PAGE IN ORIGINAL

ศูนย์วิทยทรัพยากร
จุฬาลงกรณ์มหาวิทยาลัย

CHAPTER II

Theoretical Overview of Self-Assembled Nanostructures

2.1 Quantum Confinement in Semiconductors

Quantum dots (QDs) are nanometer-scale semiconductor crystallites. Since the size of the dots is much less than the exciton Bohr radius, the electron-hole pair in a quantum dot is tightly confined in all three dimensions, known as quantum confinement, which produces a number of pronounced modifications in the optical properties of the semiconductor. To have a better understanding of quantum confinement, we will start with a discussion of the properties of the bulk materials. In bulk semiconductor materials, the energy levels of both conduction band and valence band are continuous, with electrons and holes moving freely in all directions. As the dimensions of the material shrink, effect of quantum confinement will easily be seen. Three different types of confinement that have been realized among inorganic semiconductors are described below.

2.1.1 Bulk materials

In bulk, the conduction electrons are delocalized in the plane or plate and their wavefunctions spread in three dimensions. By considering the electrons in bulk as free electron gas, the electrons are free to wander around the crystal without being influenced by the potential of the atomic nuclei. A free electron has a velocity (v) and a momentum (p = m v). Its energy consists entirely of kinetic energy; the potential energy tends to be zero (V=0). Therefore the total energy (E) of the bulk material can be considered as

$$E_{bulk} = E(k) = \frac{\hbar^2 k^2}{2m^*} \tag{2.1}$$

$$D_{bulk} = \frac{1}{2\pi^2}\left(\frac{2m^*}{\hbar^2}\right)^{\frac{3}{2}} E^{\frac{1}{2}} \tag{2.2}$$

where D is the density of states and ***k*** is electron wave number, $\boldsymbol{k} = (k_x, k_y, k_z)$.

2.1.2 Quantum Well

A quantum well (QW) is a sandwich structure with a thin layer of narrower band gap semiconductor in the middle of two layers of wider band gap semiconductor. There are two types of quantum wells. In a type I QW, a potential well, which confines the electrons and the holes in the narrower band gap material region, is formed between the narrower and wider band gap materials; while in a type II QW, the electrons and the holes are confined in different layers (see **Figure 2.1**).

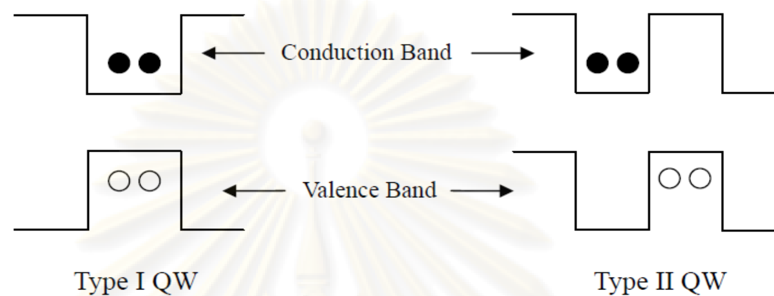

Figure 2.1 Illustration of type I and II quantum well

In a QW, the electrons and holes can only move freely in two dimensions. The model of "*a particle in a one-dimensional-box*" can be used to provide a first description of the movement of the carriers. In the semiconductor, unlike the model, the potential barriers are finite and are determined by the difference in the band gaps of the two semiconductors and whether the alignment forms a type I or type II QW. Because of the finite value of the potential barrier, the wave functions of electrons and holes do not have to be zero at the boundaries. The wave functions extend into the wider band gap material, where they decay exponentially into this region. Also, the lowest energy band-to-band optical transition is not equal to the band gap of smaller band gap semiconductor. It is at a higher energy level determined by the difference between the lowest state of the electrons in the conduction band and the corresponding state of the holes in valence band.

2.1.3 Quantum Wire

A quantum wire is a structure in which the electrons and holes are confined in two dimensions. Such confinement allows free electrons and holes behavior in only one direction, along the length of the wire.

2.1.4 Quantum Dot

Quantum dot is a brand new development from the nano particle science and the most useful quantum dot is semiconductor QDs leading to interesting electronic property for semiconductor devices. Remarkably, dots with well-defined size and spatial distribution can be formed by simply growing at the proper conditions, without the need for patterning or targeted deposition. Understanding the mechanism of dot formation is vital for the production of quantum dots with desired electronic characteristics. The concept of the QD was originally proposed by Arakawa and Sakaki in 1982.

The structure was initially known as a three-dimensional QW but later became known as a quantum box, however, in the nineties, the name quantum dot became the standard, as a result of the wide variety of possible dot shapes in practice. For quantum dots to provide properties useful in devices operating at room temperature, such as lasers, a number of conditions must be fulfilled. First and foremost, the dot size should be small enough to observe zero-dimensional quantum confinement effects and the potential offset between the dot and barrier must be sufficiently deep to observe such effects.

The requirement that at least one electron or hole energy level be confined sets a lower limit on QD size and is of course dependent on the band offset between the dot and barrier materials. On the other hand, an upper limit on dot size may be thought of in terms of thermal evaporation of carriers from the dots through higher energy levels. Ideally, the energy separation between levels should be greater than k_BT, for devices operating at room temperature **[23]**.

The second condition is that the size homogeneity and surface density of the dot ensemble should be high. The variation in size, shape and composition of self-assembled dots is dictated largely by random fluctuations during growth and typically gives rise to a Gaussian variation in the energy position of the electron and hole levels between dots. Finally, we require that the materials used are free from defects, such as dislocations. Fortunately, self-assembled growth appears to provide the high material quality needed. Self-assembled growth has proven to be an extremely fruitful technique which is now widely used.

In the self-assembled growth the quantum dots are created from ultrathin layers (typically about 2 monolayers thick) which spontaneously break up due to strain between the substrate and the grown film, and minimize their energy by forming small scale islands. Size quantization in such islands has been demonstrated. In the last few years, nanostructures have been successfully realized using self-organization effects, which occur during growth of lattice mismatched heterostructures. These effects are also called self-ordering or self-assembly. Self-assembled QDs should fulfill the following requirements in order to make them useful for devices at room temperature **[24]**:

- Sufficiently deep localizing potential and small QD size is a prerequisite for observation and utilization of zero-dimensional confinement effects.
- QD ensembles should show high uniformity and a high volume filling factor.
- The material should be coherent without defects like dislocations.

The interest in quantum dots was initially driven by a desire to create a material with electronic density of states strongly modified by quantum confinement effects (a reduction in size to less than tens of nanometers) and approaching a delta-like density of states for a truly zero-dimensional system. Such a medium was perceived to offer significant advantages for example in ultra-low threshold semiconductor diode lasers, and also presented interesting opportunities for fundamental research in the area of light-matter interaction.

Studies of quantum dots attract significant interest worldwide, because of their fascinating new physics and unique potential for innovative electronic and optoelectronic devices. Actually, these innovative applications are just beginning to emerge. One of them involves using quantum dots for the detection of infrared light in devices similar to the previously explored quantum well intersubband detectors. Other interesting applications include use in quantum gates at the centre of a quantum computer.

As can be deduced from the above section, the detail and simple explanation of bulk, quantum well, quantum wire and quantum dots were preferred to understand background of quantum confinement effect. The following section will be described briefly about quantum confinement effects.

2.1.5 Summary of Quantum Confinement Effects

Quantum confinement introduces a number of important modifications in the physical properties of semiconductors. A brief summary of the quantum confinement effects is presented below.

First of all, quantum confinement introduces a pronounced change in the density of states of semiconductor. The density of states *g(E)* is defined by the number of energy states between energy *E* and *E+dE*, which is derived by *dn(E)/dE*. For electrons in a bulk semiconductor, *g(E)* is zero at the bottom of the conduction band and increases as the energy of the electrons in the conduction band increases, given by $E^{1/2}$. Their confinement result in quantization of carrier energy levels, so-called, discrete energy level which exhibit delta-like density of state as shown in **figure 2.2**, which compares the density of states for electron in a quantum well (and also in quantum wire and dot), where the density of states is a step function because of the discreteness of the energy levels along the confinement direction.

The density of states for a quantum wire has an inverse energy dependence $E^{-1/2}$. For each sub-band, the density of states has a large value near $k_z=0$ and decays as $E^{-1/2}$ as k_z has nonzero values for that sub-band. The energy levels for an electron in a quantum dot have only discrete values, which makes the density of states a series of delta functions at each of the allowed energy value, i.e. $g(E) = \delta(E-E_n)$ $(n=1, 2, ...)$. Theoretically, this feature gives sharp absorption and emission spectra for quantum dots even in room temperature. Quantum confinement also induces a blue shift in the band gap and appearance of discrete sub-bands corresponding to energy quantization along the direction of confinement. The quantum mechanics description of this phenomenon will be presented later in this chapter. As the dimensions of the material increase, the energy of the confined states decreases so the inter-band transitions shift to longer wavelengths. When the dimensions of the material are greater than de Broglie wavelength, the inter-band transition energy finally approaches the bulk value.

As mentioned above, the density of states for both a balance band and a conduction band are significantly modified by the quantum confinement. Instead of a smooth and

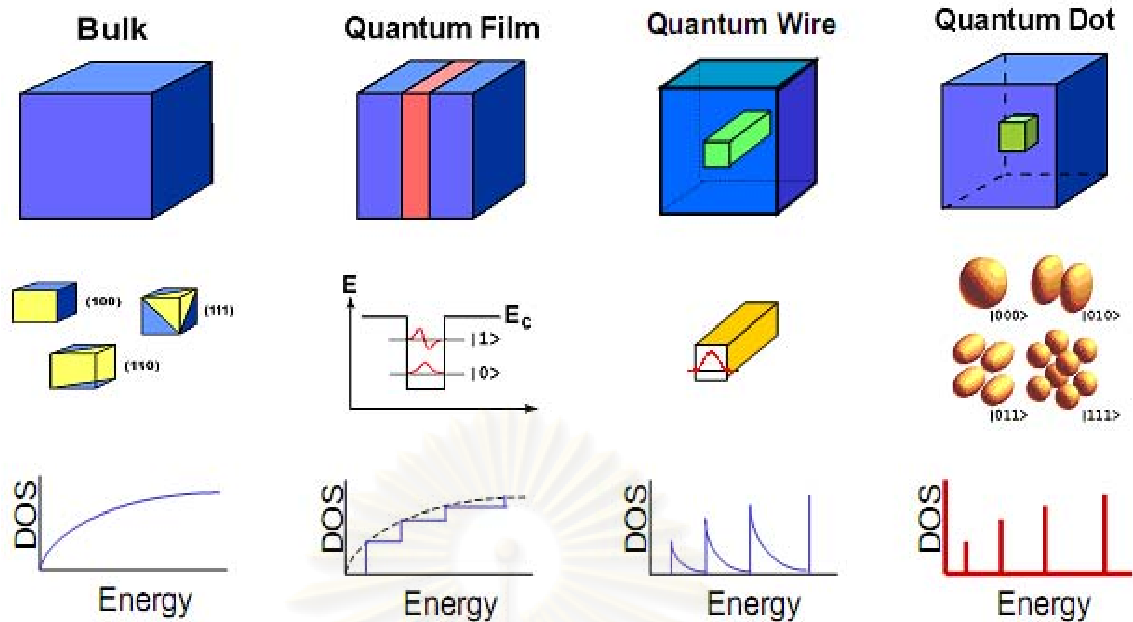

Figure 2.2 Schematic views and graphs of (a) bulk, (b) quantum wells, (c) quantum wires and (d) quantum dots and their density of states (D.O.S) **[25]**.

continuous distribution of the density of states, the energy states are packed in a narrow energy range as the dimension of the material shrink. Discrete energy levels concentrate oscillator strength to the lowest level transitions. The oscillator strength of an inter-band optical transition depends on magnitude of the density of states in both the valence bands and the conduction bands. It also depends on the overlap of the wave functions of electrons and holes. Both factors produce a larger enhancement of oscillator strength with increasing quantum confinement in Type I semiconductors, and the oscillator strength is maximized for quantum dots, which are the most confined structures.

Intra-band transitions, also known as free carrier absorption in the bulk semiconductor, are electrons movements from one allow energy to another within the conduction band or holes from one allow energy to another in the valence band. These transitions often depend on the presence of free carriers introduced by impurity doping or charge injection by a bias field. In the bulk, because intra-band transitions from one *k* value to a different *k* value of conduction band require a change of quasi-momentum *k*, which could occur with lattice phonons coupling, these processes are usually much weaker than band-to-band transitions, which do not require a change of *k*. However, in quantum confined structures such as a quantum well, sub-bands exist

that correspond to energy quantization along the direction of confinement. For the conduction band in a quantum well, an electron can shift from one sub-band to another without changing its two-dimensional quasi momentum k. These new transitions have been utilized to produce sub-band detectors and lasers, such as QWIPs (Levine 1993) and quantum cascade lasers (Faist, Capasso et al. 1996; Capasso, Faist et al. 1997).

Similar to the intra-band transition, an inter-band transition for indirect band-gap material, such as silicon, also requires a change of quasi-momentum k and, thus, involves the phonon coupling. As a result, the emission of a photon produced by the transition of an electron from the conduction band to the valence band, known as recombination of electron and hole, is either extremely weak or nonexistent in the bulk form of an indirect gap semiconductor.

Trap-assisted recombination could occur when an electron falls into a "trap", an energy level within the band gap introduced by the presence of a foreign atom or a structural defect. In a second step, the “trapped” electron moves into an empty valence band state to complete the recombination process. However, the traps are generally undesirable because they shorten the lifetime of carriers and produce multiple energy pathways which contribute to non-radiative recombination. While in the quantum confinement structures, quasi momentum uncertainty Δk is increased because position uncertainty of electrons Δx is reduced by the confinements, according to the “uncertainty principle”. The relaxed quasi momentum Δk selection rule, then, allows enhanced emission to be observed in some indirect band gap material, such as porous silicon (Canham 1997) and silicon nanoparticles (Belomoin, Therrien et al. 2002).

Band gaps of bulk semiconductors can be altered by many factors, such as temperature and stress by applied mechanical force. The most noticeable among these is the Stark effect, which is the change of the electrical properties and the optical spectra due to the modified energy band structure by an applied electric field. In quantum confinement structures, such as a quantum well, if an electric field is applied along the confinement direction, the binding energy of the exciton decreases as the electric field pushes the electron and hole wave functions to opposite sides of the confined region. The electric field can also mix different quantized states and,

therefore, the oscillator strength redistributes between optically allowed (such as $1S_{3/2}1S_e$) and optically forbidden (such as $1P_{3/2}1S_e$) excited states through matrix element

$$W_{sp} = \langle 1S_{3/2}1S_e \,|erF|\, 1P_{3/2}1S_e \rangle \quad (2.3)$$

where *er* is the electric dipole operator and *F* is the electric field. The combination of all these effect is called quantum confinement Stark effect.

2.2 Applications of Quantum Dots

Quantum dots are potentially useful for a number of different technologies. While there is at present no established application of quantum dots, there are a number of very promising areas. Due to their strong size dependent optical properties, quantum dots have been explored extensively in many aspects of applications, which are covered by a number of reviews (AJ 2002; WCW, DJ et al. 2002; A, X et al. 2003; WJ, D et al. 2003; X and S 2003; P 2004; Parak, Pellegrino et al. 2005).

The advantages of quantum well lasers on traditional lasers first predicted in 1970s (Dingle and Henry 1976), and first quantum well lasers which were very inefficient were demonstrated at those dates (van der Ziel et al. 1975). Since the quantum confinement in a QD is in all three dimensions, tunability of a quantum dot laser (QDL) is higher than a quantum well laser (QWL). The concept of semiconductor QDs was proposed for semiconductor laser applications by Arakawa and Sakaki in 1982, predicting suppression of temperature dependence of the threshold current. Henceforth, reduction in threshold current density, reduction in total threshold current, enhanced differential gain and high spectral purity/no-chirping were theoretically discussed in 1980’s (Asada et al. 1986). **[26,27]**. QD lasers acquired more importance after significant progress in nanostructure growth in the 1990’s such as the self-assembling growth technique for InAs QDs.

The first demonstration of a quantum dot laser with high threshold density was reported by Ledentsov and colleagues in 1994. Bimberg et al. (1996) achieved improved operation by increasing the density of the QD structures, stacking successive, strain-aligned rows of QDs and therefore achieving vertical as well as

lateral coupling of the QDs. In addition to utilizing their quantum size effects in edge emitting lasers, self-assembled QDs have also been incorporated within vertical cavity surface emitting lasers **[28]**.

QD lasers are not as temperature dependent as traditional semiconductor lasers. This theory was utilized by applications and in 2004; temperature-independent QD lasers were invented in Fujitsu Laboratories. Other monolithic semiconductor mode-locked lasers (MLLs) are of great interest for optical communications due to their compact nature, mechanical stability and robustness, high repetition rates and low timing jitter.

Recently, quantum dot (QD) MLLs have received attention **[29]**, their inherent properties, such as very broad spectral gain bandwidths **[30,31]**, better temperature stability **[32]**, ultra-low threshold current density **[33]**, and much faster carrier dynamics **[34]** are expected to lead to improved performance. The first demonstration of a QD MLL was by Huang et al **[35]** in 2001 using a two-section InAs/GaAs-based QD gain material. More recently, QD MLLs have been reported using InAs/InP-based QDs operating at the important telecom wavelengths around 1.5 μm **[36–38]**.

In the past decade, quantum dots have been highlighted as bio-labels since they offer many advantage over the traditional fluorophores. First of all, these inorganic materials are more robust against photobleaching than organic molecules (Parak, Pellegrino et al. 2005). This is particularly important for experiments that require observations with extended period of time. In fact, this benefit has already been successfully demonstrated in many practical labeling processes (Parak, Boudreau et al. 2002; Pellegrino, Parak et al. 2003).

Secondly, since the photoluminescence wavelength of quantum dots are determined by their size, multicolor imaging can be conducted with same material of different sizes (Rosenthal, Tomlinson et al. 2002). Also, complexity of sample preparation is limited because their surface properties are defined by the coating material. In addition, quantum dots have broad absorption spectra and narrow emission bands so it is possible to excite different dots with single light source and the emissions from one sized quantum dot can be easily distinguished from that of another sized quantum dot.

Another advantage of quantum dots is their long fluorescence lifetime, which is on the order of a few tens of nanoseconds. In contrast, the fluorescence lifetime of organic fluorophores is about a few nanoseconds, the same as many biological samples' auto-fluorescence. Thus, by using time delayed detection system, fluorescence signal from quantum dots can be recorded virtually free of background noise (Dahan, Laurence et al. 2001).

In current work, we fabricated InP QDs grown on InGaP barrier using GaAs substrate. Research on InP and related compounds has been increasing exponentially in recent years. This is due to fact that InP is a key semiconductor for production of optoelectronic and photonic devices. In particular, InP and related compounds such as InGaAsP are key semiconductor materials for communications in the 1.3 and 1.55 μm special regions as well as for many other optoelectronic applications. The applications of InP and related materials have been extended to other areas that include laser diodes (LDs), light emitting diodes (LEDs), photodetectors, waveguides, photocathodes and solar cells **[41]**. In reality, high-speed Internet communication systems are now established wholeover the world based on these devices.

Red light emitting QD lasers have also been successfully fabricated with InP/GaInP QDs and AlInAs/AlGaAs QDs. It is possible to access new energies by combining materials with different lattice constants and energy gaps. The perfect analog on would be InP dots in a GaP matrix. However, due to the indirect character of GaP, this material is less attractive for optoelectronic applications. Therefore, most of the research concentrated first on InP dots in a InGaP matrix, a ternary compound which is lattice matched to GaAs for nearly equal parts of Ga and In. The larger band-gap of phosphides open another interesting part of the spectrum for quantum dots laser diodes:

InGaP is the material of choice for high brightness red and yellow light emitting LEDs as well as for red light emitting laser diodes with emission wavelengths around 650 nm. InP is also very promising as high frequency devices in the frequency range exceeding several tens GHz such as high-electron-mobility transistors (HEMTs) and hetero-bipolar-transistors (HBTs) **[42,43]**. These InP based devices may find new

application fields in millimeter wave communications, anticollision systems and imaging sensors **[44]**.

Some of compound semiconductors are promising for solar cells because they have bands gap of around 1.4 eV which assures high energy conversion efficiencies. The band gap of InP is 1.35 eV, which is also a convenient value for high conversion efficiency for solar cells. InP is promising as solar cells for space cells satellites, because of its high resistivity against radiation **[45]**. In fact, InP based solar cells with p-n junctions based on thermal diffusion have been fabricated for a space satellite **[46]**. These saturations make InP an interesting material for the future new applications in addition to the presently established applications.

2.3 Synthesis Methods of Quantum Dots

Depending on their applications, high quality quantum dots of various semiconductor materials have been synthesized either on a substrate or dispersed in (organic/inorganic) solution. Some of the major methods used to fabricate quantum dots are described in this section.

2.3.1 Epitaxial Growth Techniques

Molecular Beam Epitaxy (MBE) is a widely used technique for epitaxial growth of quantum-confined structures of both II-VI and III-V compound semiconductors as well as silicon and germanium. The growth is carried out in an ultrahigh vacuum chamber, where the atoms that are the constituents of the semiconductors to be grown are evaporated by heating the effusion cells or ovens. The vapor passes through a small orifice, accelerated by the pressure differential on two sides of the orifice, and, thus, forms a molecular beam. Because of the low density of this molecular beam, the particles neither react nor collide with each other before they impinge on the substrate mounted on the opposite side of the chamber.

By monitoring and controlling the fluxes from different cells together with the substrate temperature, the composition and the epitaxial growth rate on the substrate can be precisely controlled. The ultra high vacuum chamber in MBE allows the use of many in situ analytical techniques to characterize the condition of the substrate

surface prior to growth and the crystallinity, composition, and thickness of the epitaxial material. The MBE technique is well suited for fabrication of quantum wells, quantum wires and quantum dots. The quantum well growth can be precisely controlled layer by layer. The fabrication of quantum wires and quantum dots can be realized by using substrates with a patterned surface.

Another form of quantum dot array, three-dimensional islands on a substrate, can be synthesized when there is a large strain between a thin epitaxial layer and the substrate due to a significant lattice mismatch between the two materials. The surface reconstruction, facilitated by the substrate temperature, results in the formation of three-dimensional structures, composed of the epitaxial material at regular spacing across the surface of the substrate. MBE technique has revolutionized the semiconductor technologies and widely used in manufacturing semiconductor laser diodes and quantum dot laser diodes, which involve MBE-growth quantum well and quantum dot structures.

Metal-organic chemical vapor deposition (MOCVD) is another commonly used epitaxial growth method in which the semiconductor structure are grown from the precursors of metal organics and hydrides. In a MOCVD process, the suitable precursors of semiconductor in gas form are transported to the reaction chamber, and then deposition and growth of the semiconductor take place on a substrate. Finally, the remaining decomposition products are removed from the chamber.

Self-assembled GaN quantum dots were grown on the $Al_xGa_{1-x}N$ surfaces using a surfactant has been reported (Tanaka, Iwai et al. 1996). Generally, MOCVD offers the advantage of being a simple and faster growth technique, with a growth rate typically 10 times that of MBE. However, the precursors are highly toxic and, thus, require extreme safeguard and care during handling. In addition, the hydrodynamic condition of gas flow does not permit the extensive in situ characterization. Another technique to grow quantum dots on a substrate that have evolved in recent years is laser-assisted vapor deposition (LAVD), in which the deposition materials ablated by lasers are directly deposited onto the substrate or mixed with a reactive gas to produce the appropriate material (Ventra, Evoy et al. 2004).

2.3.2 Colloidal Synthesis of Quantum Dots

An alternative approach is to produce quantum dot in solutions, called colloidal synthesis, which deals with chemical reactions in solution on a nanometer scale. Colloidal synthesis has been conducted to make semiconductor nanostructures of different composition, size and shapes. This method involves growing nanoparticles of inorganic materials through chemical reaction of their precursors and, sometimes, controlled precipitation of the reaction product in certain solvents.

Generally, the growth process starts with the fast formation of a huge number of nuclei. Then more and more of the solid product deposits onto the nuclei, so the sizes of the crystallites grow slowly till the desired size is reached, at which time the reaction must be quenched. Otherwise, the dots could keep growing under a process, known as Ostwald ripening, which is the growth of larger dots through the transfer of material from smaller ones, which have a higher solubility. High quality quantum dots used in biological applications have been exclusively prepared by advanced colloidal chemistry over the past decades. Different approaches to stabilize QDs in aqueous solution have been proposed and realized **[47]**.

2.4 Nanostructures by Self-Assembling

Reducing the dimensionality of semiconductor structures benefits basic semiconductor physics and device technology (Reed et al, 1988). Therefore, the understanding of growth mechanisms of self-assembled nanostructures is needed. This section reviews the fundamental mechanisms and theories of the growth of self-assembled islands.

2.4.1 Self-Assembled Growth

When a lattice mismatched structure is grown on a substrate, the lattice constant of the first few monolayers (MLs) of the deposited material is forced to match that of the substrate. The change from the desired lattice constant creates strain in the deposited layer. After a few MLs, the strain in the epilayer builds up and the strain energy is released, in some circumstances, by forming small islands. These islands are zero-dimensional, and are usually referred to as self-assembled quantum dots (SAQDs).

Three possible growth modes can occur when a strained epilayer is grown on a substrate under near equilibrium conditions and these are shown in **figure 2.3**.

For a small lattice-mismatched system, when the mismatch is less than or equal to 2%, the epilayer grows in a 2D layer-by-layer, or Frank-van der Merwe, growth mode as shown in **figure 2.3(a)**. If the lattice mismatch is increased, the growth occurs in a 3D mode known as Stranski-Krastanow (SK) where the growth initially starts out layer by layer, but later develops into islands with a wetting layer (WL) formed from the first phase of growth as shown in **figure 2.3(b)**. Finally, at higher lattice mismatch, islands are instantly formed and this is called Volmer-Weber growth mode as shown in **figure 2.3(c)**. The nature of the change from 2D to 3D growth mode can be explained by the surface/interface free energy model (Gilmer and Grabow, 1987). If we consider the growth mode in terms of surface energies during the film deposition, we can define the change of total energy of a surface before and after deposition $\Delta\gamma$:

$$\Delta\gamma = \gamma_f + \gamma_i - \gamma_s \quad (2.4)$$

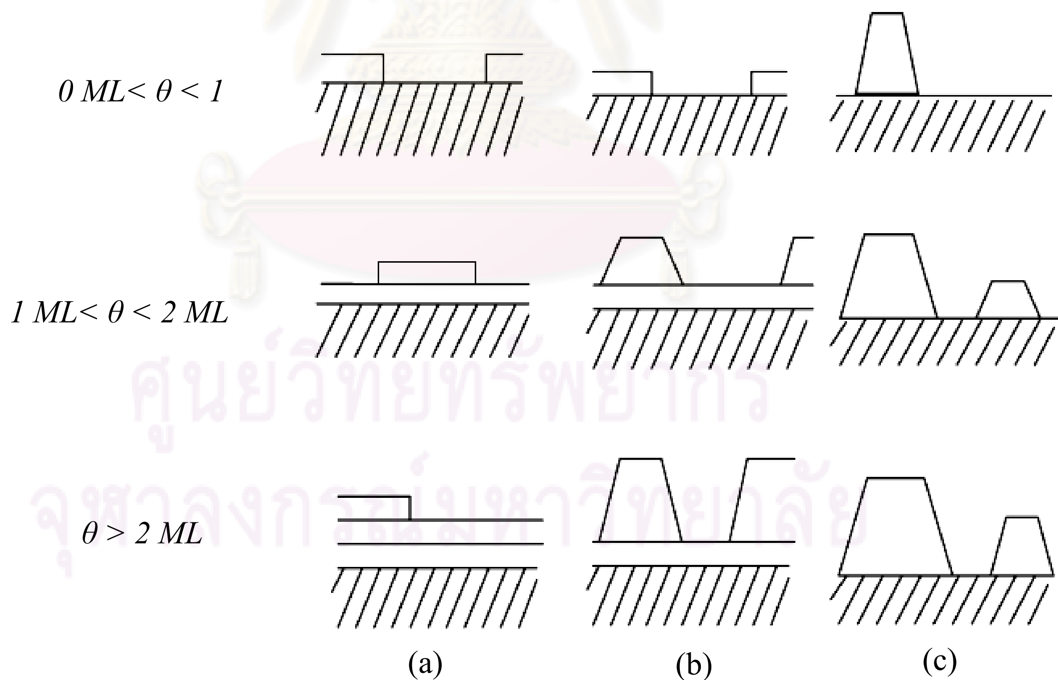

Figure 2.3 Schematic representation of the three crystal growth modes of a film for a different coverage (θ) (a) layer-by-layer or Fran-van der Merwe (b) layerplus-island or Stranski-Krastanow mode island and (c) Volmer-Weber (Herman and Sitter, 1989).

where γ_s is the substrate surface energy, γ_f is the film surface energy, and γ_i is the interface energy between the film and the substrate which includes additional energy arising from the strain between the film and the substrate.

If $\Delta\gamma < 0$, layer-by-layer growth mode arises because the atoms of the deposit material are strongly attracted to the substrate than they are to themselves. On the contrary, if $\Delta\gamma > 0$, the deposit atoms are more strongly bound to each other than those to the substrate and the growth mode known as island or Volmer-Weber mode results. Between these two modes is the SK growth mode which arises when the interface energy increases as the layer thickness increases and $\Delta\gamma$ reaches zero. In the SK growth mode, islands are formed on top of the WL and the SK growth is sometimes called layer-plus-island growth. Because the QDs grown in this work is SK QDs, the details of SK mode are thus given more importance and explored further here.

2.4.1.1 Stranski-Krastanow Mode

The first observation of self-assembled island formation, which is a special case of the Stranski-Krastanow growth, was made in 1985 **[48]**.When epitaxially growing one material on another (heteroexpitaxy), there are three possible modes. The first, Frank-van der Merwe, is simply the successive addition of 2-D layers to the substrate crystal. The second mode, Volmer-Weber, will occur if the added material can minimize its free energy by trading increased surface area for decreased interface area, forming an island structure like water droplets on glass. A third possibility can arise if the lattice spacing of the added material mismatches the substrate **[49]**. Here, growth starts with a strained 2-D wetting layer, but islands form after the first few monolayers. The driving force is the incorporation of dislocations within the islands to relieve strain. This third mode is called Stranski-Krastanow **[50]**.

Stranski-Krastanow growth is also an intermediary process characterized by both 2D layer and 3D island growth. Transition from the layer-by-layer to island-based growth occurs at a critical layer thickness which is highly dependent on the chemical and physical properties, such as surface energies and lattice parameters, of the substrate and film **[51]**. Island formation in the SK growth mode is related to the accommodation of elastic strain associated with lattice mismatch. Strain relaxation in some growth conditions by the transition from platelets 2D to coherent islands 3D is

explained by the elastic strain energy, *E (el),* during the growth of lattice mismatched system:
(Seifert et al., 1996)

$$E\ (el) = \lambda\, \varepsilon^2 A\, t \ldots\ldots\ldots\ldots \quad (2.5)$$

where λ is the elastic modulus, ε is the lattice mismatch, *A* is the surface area, and *t* is the film thickness. The elastic strain energy for layer-by-layer growth will increase linearly as a function of the deposited film volume and the energy will increase either to the point where coherent islands are nucleated, this appears as point t_{cw} in **figure 2.4** or until it reaches the activation energy for dislocation formation, t_{cd} in the same figure. The SK growth process can be explained by **figure 2.5** where the three distinct energy periods are plotted. The first period A has two regions: the stable 2D area and the metastable 2D area, or pseudomorphic 2D layer area. At the beginning of film deposition, the stable 2D layer-by-layer growth leads to a perfect wetting of the substrate. After the film exceeds the critical wetting layer thickness (t_{cw}), 2D growth proceeds into the metastable 2D area where excess energy is stored due to the building up of a supercritical thick wetting layer. During epitaxy, the deposition of the island material starts with a complete wetting of the substrate. As the deposition continues, the accumulated strain energy, E_{el}, increases linearly with the wetting layer

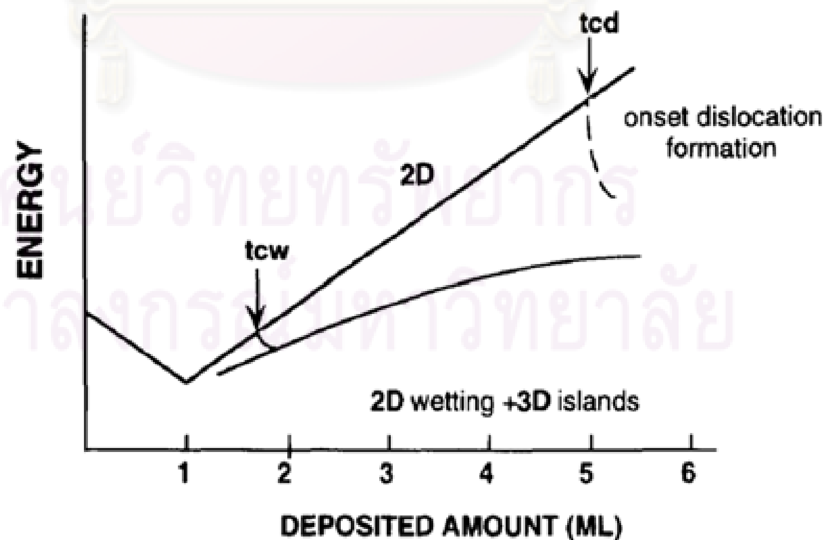

Figure 2.4 Schematic representation of total energy change for a strained system in 2D and 3D growth modes. t_{cw} and t_{cd} are critical thicknesses for formation of islands and dislocations, respectively (Seifert et al., 1996).

thickness, according to $E_{el}=c\varepsilon^2 t$, where c is the elastic modulus, ε is the lattice mismatch, and t is the wetting layer thickness. The deposition rate, R, increases linearly in time, see **figure 2.5**. When the wetting layer thickness exceeds the equilibrium wetting layer thickness, t_e^c, the system enters a meta-stable region. There is potential for island formation, but the activation energy for the formation needs to be overcome.

When the critical wetting layer thickness, t_c is reached, the island nucleation starts and the wetting layer starts to decompose. Mobile adatoms from a decomposing wetting layer stick together with the deposited adatoms at the surface, and island nuclei form. When these nuclei become larger than a certain critical size, determined by surface and interface energies and bond strength, they grow steadily. Before the nuclei reach this critical size, they run the risk to dissolve **[52]**. Examples of some suitable materials combinations for island growth are, for instance, InP on $Ga_xIn_{1-x}P$/GaAs, $Ga_xIn_{1-x}As$ on GaAs, $Ga_xIn_{1-x}P$ on GaP, InAs on InP, and Ge_xSi_{1-x} on Si, amongst others.

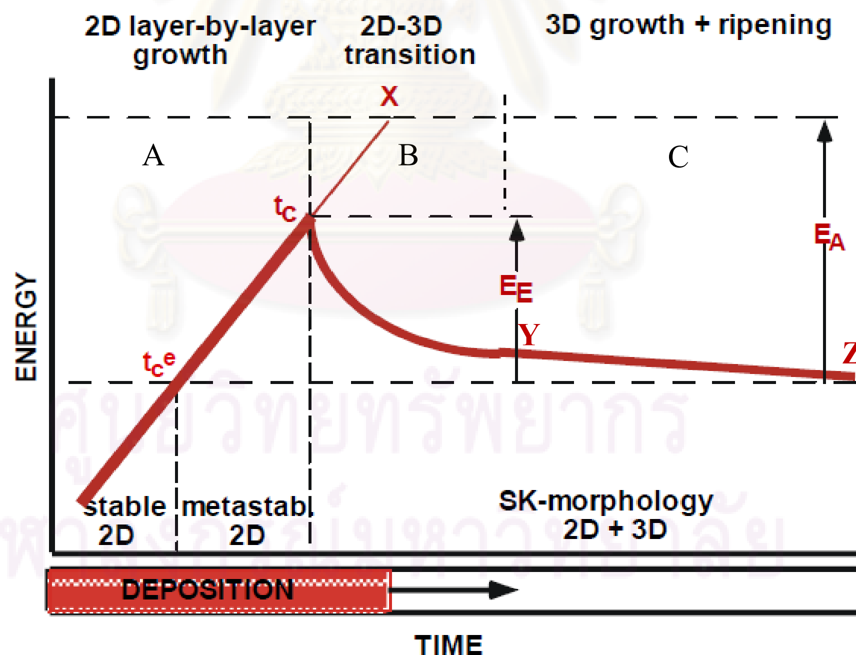

Figure 2.5 Schematic of the total energy vs. time for the self-assembling process. T_c^e, and t_c are the thermodynamically and kinetically defined critical wetting layer thickness, E_E is the excess energy due to strain, and E_A the 2D-3D activation barrier. X is the point where a pure strain-induced transition becomes possible (no thermal activation) **[51]**

This section can be achieved to summarize the principle and give some idea about the underlying mechanism of Stranski-Krastanow growth mode. However, what counts are the facts, and it was possible to present better and deeper understanding of the perspective of Stranski-Krastanow growth mode in the next section.

2.4.1.2 Materials Consideration in S-K Mode

Self-assembled SK QDs have been studied in various semiconductors. They are grown on Si, GaAs or InP substrates. Among these three materials, GaAs and InP are direct bandgap materials and Si is indirect. Therefore, Si is useless as light emitters although it is inexpensive, while InP and GaAs find many optoelectronics applications such as laser diodes. The epilayer of self-assembled SK QDs is required to have a larger lattice constant than those of the substrate. This limits the type of material, and, consequently, the range of energy associated with the epilayer. Therefore, material consideration is an important role for the study of self-assembled growth.

Figure 2.6 shows the relationship between the lattice constant and energy gap of III-V semiconductor material systems. As seen in the figure, InAs on GaAs (or Ge on Si) is

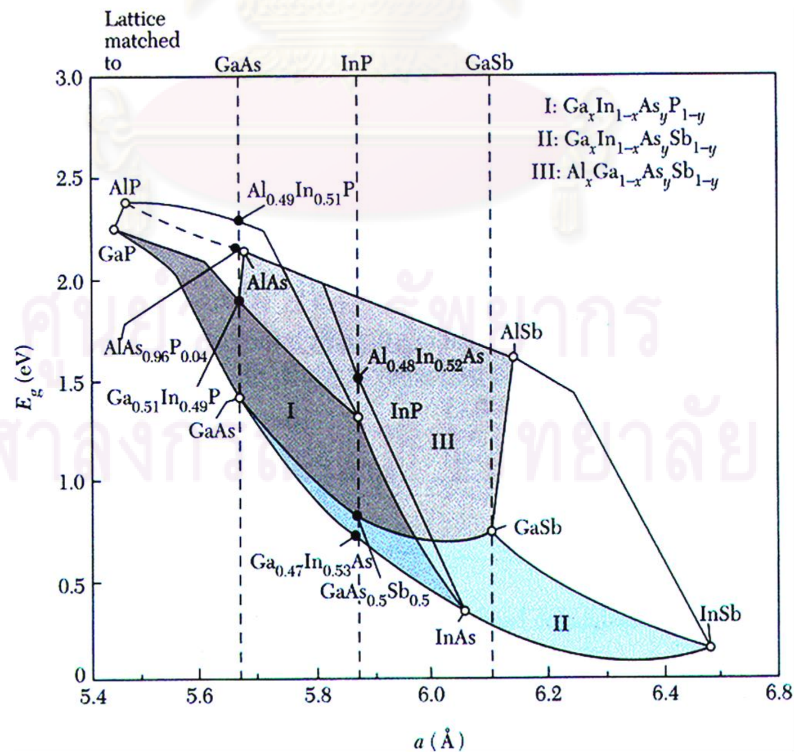

Figure 2.6 Bandgap energy versus lattice constant of various III-V compound semiconductors at room temperature

a good material system for QD studies since a lattice constant of InAs is larger than GaAs and carrier confinement is possible since the energy gap of InAs is smaller than that of GaAs. In this work, another materials combination, widely investigated by MOVPE **[53-55]** but less so by MBE **[56]**, is the system InP/ InGaP /GaAs (001) (misfit ≈ 3.8%), with InP forming the dots and InGaP the barrier, lattice matched to GaAs substrate. Since optimum growth temperatures for InP in MOVPE are higher than those for InAs (best in the range between 550 and 700 °C), MOVPE-grown dots of InP are generally larger. Typical base diameters are in the range of about 40-80 nm, and heights are in the range of about 12-25 nm, depending on deposition conditions. If these dots that embedded into InGaP, are fully developed, luminescence will be at about 1.65 eV. This heterocombination is particularly attractive for optoelectronic applications based on GaAs substrates and for basic studies of self-assembling. The growth parameters can be varied across a wide range: the deposition temperatures in MOVPE, for instance, between 550 and almost 700°C, which significantly affects surface densities, sizes, and shapes of the islands. An extension to even lower temperatures of about 470°C can be made by using MBE as the deposition technique **[57]**. The more detailed discussion about self-assembled in MBE and MOVPE with the materials combinations InP/InGaP/GaAs (001) will be described in chapter 4.

2.4.1.3 Size and Morphology of S-K Islands

In the following discussion we will address the relationship between the density, size and morphology of the islands. The sizes (i.e., average values of the size distribution) of coherent islands in the III-V combinations are range between base areas of 12x12 nm^2 for InAs/GaAs and 45x60 nm^2 for InP/InGaP. The typical maximum densities and morphology shapes of the islands vary simultaneously. Islands of InAs on GaAs reach a maximum density at around $10^{11} cm^{-2}$. At this density the islands have an average spacing of about 30 nm (center to center) and this is obviously the density where the local strain fields around the islands overlap so that no more additional nucleation takes place.

Consequently, for different thicknesses of the initial wetting layer different amounts of deposited material must be accommodated into a fixed number of islands, which affects the 3D shape of the islands. This characterization of this work is InP islands

grown on InGaP layers. For these materials combination InP/GaInP, the objects for investigation are larger and geometrical differences are more easily visible. Most of AFM investigations showed a bimodal size distribution, dependent on the InP deposition in MOVPE at around 650 °C, with flat (= 2 nm high), irregularly shaped islands and larger (= 23.5 nm high), rather uniform islands. This bimodal size distribution is typical for small amounts of InP deposition. In addition to these coherent islands for higher depositions of InP also much larger *noncoherent,* i.e., relaxed islands have been observed.

The smaller islands in this materials combination have not been very well characterized, up to now. The high area densities of these islands in the order of 10^{10} islands/cm^2 for low deposition of InP **[58]** and their disappearance with increasing deposition of InP characterizes them as pre-stages on the way towards the fully developed islands. the diameter of the small islands varies up to a maximum of about 40 nm, which is also the base-diameter of the fully developed islands.

Depending on the deposition conditions (temperature, surface concentration and mobility of excess material) some of these islands size could then reach a critical size by thickening and this could then be the qualitative change towards the formation of stable 3D islands. Regard on some experimental results, the disappearance of the small islands in samples with post-growth annealing and high area densities of fully developed islands shows that these small islands are highly unstable and act as food for the larger islands. Note that the larger, non-coherent islands differ only in their size, but not in their principal shape from the fully developed islands.

2.4.2 Theory of Self-Assembled QD Formation

The theoretical work on self-assembled QD formation can be explained by equilibrium and nonequilibrium aspects. For the equilibrium aspects, QD formation can be explained using energetic principles and thermodynamics (Shuchukin et al., 1995; Daruka and Barabási, 1997). For the nonequilibrium aspects, QD formation can be explained using dynamical models (Dobb et al., 1997; Daruka et al., 1997). In this section, the thermodynamic and dynamical or kinetic analyses are reviewed.

2.4.2.1 Thermodynamic Analysis

The total energy of a coherently strained 3D island can be expressed in terms of elastic energy ($E_{elastic}$), surface energy (E_{surf}) and edge energy (E_{edge}) as:

$$E_{total} = E_{elastic} + E_{surf} + E_{edge} \quad \text{.......................(2.6)}$$

Moreover, the energy per atom per unit volume in a pyramid-shaped island with a base length of L can be obtained by the sum of all the L-dependent terms as follows: (Bimberg et al., 1999)

$$E(L) = E_0 + \left[-2\left(\frac{L_0}{L}\right)^2 \ln\left(\frac{e^{1/2}L}{L_0}\right) + \frac{2\alpha}{e^{1/2}}\left(\frac{L_0}{L}\right) \right] \quad \text{..............(2.7)}$$

where E_0 and L_0 are the characteristic energy and length of the pyramid, respectively. *E(L)* is governed by the control parameter α which is a function of the surface energy and the elastic strain energy of the island. A representative diagram for **equation (2.7)** is shown in **figure 2.7**. The island is in the most stable and optimum size at the minimum energy (min $E(L) \equiv E(Lopt)$) < 0) if α = 1. However, the island will be ripening at the energy $E(L) \rightarrow 0$ if $\alpha \rightarrow \infty$. If $1 < \alpha < 2e^{-1/2} \approx 1.2$, the island is in a metastable state where $E(L) > 0$. Therefore, the local minimum energy $E(L)$ disappears when $\alpha > 1.2$ and there exists a thermodynamic tendency to ripen and become a single huge cluster where all the deposited materials are collected (Shchukin and Bimberg, 1999). The investigation of the equilibrium properties of strained heteroepitaxial systems is studied by taking in to account WL in order to get

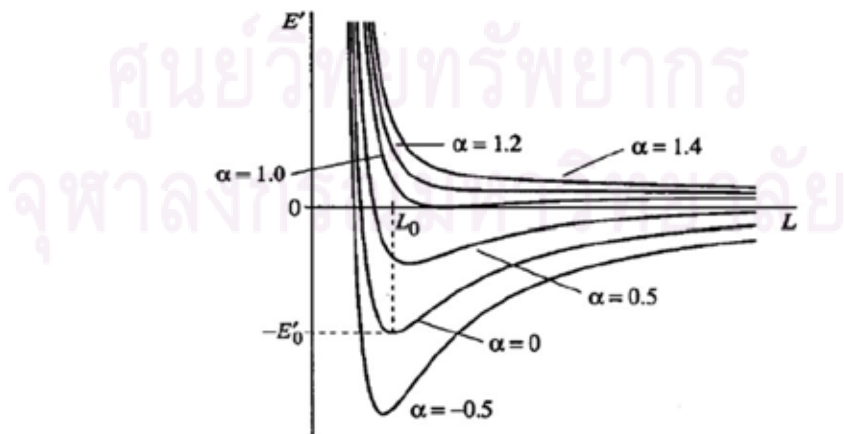

Figure 2.7 Energy of an array of 3D coherently strained islands per one atom versus size of the atom. The control parameter α is the ratio of the surface energy and edge energy (Bimberg et al., 1999).

more understanding of the equilibrium system (Daruka and Brabasi, 1997).

In their work, the desorption and interdiffusion of QD material were neglected in order to conserve the system and stored the energy in the WL with respect to the film coverage in order to minimize the energy of the system. When H ML of epilayer is deposited on a substrate, a fraction of H ML (H_1) is formed as a wetting layer and H_2 ML is distributed in the form of 3D pyramidal shaped islands. The rest of the H ML which is equal to (H-H_1-H_2) ML is assembled in the ripened islands. This implies that the growth of 3D coherent islands is initiated via the formation of 2D platelets which act as precursors. Therefore, the total energy density (total energy per unit cell) of this system is given by

$$E = H_1 E_{WL} + H_2 E_{island} + (H - H_1 - H_2) E_{rip} \qquad (2.8)$$

From the **equation (2.8)**, the nucleation of 3D islands depends on the WL thickness, and the total volumes of all islands are not limited. The Phase diagram of lattice-mismatched system shown in **figure 2.8** is for the understanding of the equilibrium morphology of the heteroepitaxial system **[59]**. In this figure, there are six growth modes (phases) and these phases are separated by the phase boundary lines: H_{c_2}: FM - R_1, FM - SK_1; H_{c_2}: SK_1- R_2; H_{c_3}: SK_2-SK_1; H_{c_4}: VW-SK_2, VW-R_3 (Barabasi, 1999).

The FM phase

In this phase, the deposited material contributes to the pseudomorphic growth of the wetting film, and the islands are absent, reminiscent of the so-called FM growth mode. The WL thickness in this case is the same as the nominal thickness of the material deposited, H. Such growth of the WL will continue until H reaches a critical value H_{c_1}, which defines the phase boundary between the FM and either the R_1 or the SK_1 phases.

The R_1 Phase

Above H_{c_1}, the inequality $0 < \varepsilon < \varepsilon_1$ is satisfied after the formation of a WL of $n_1 = H_{c_1}$ ML, the excess material (H—n_1) contributes to the formation of *ripening* islands.

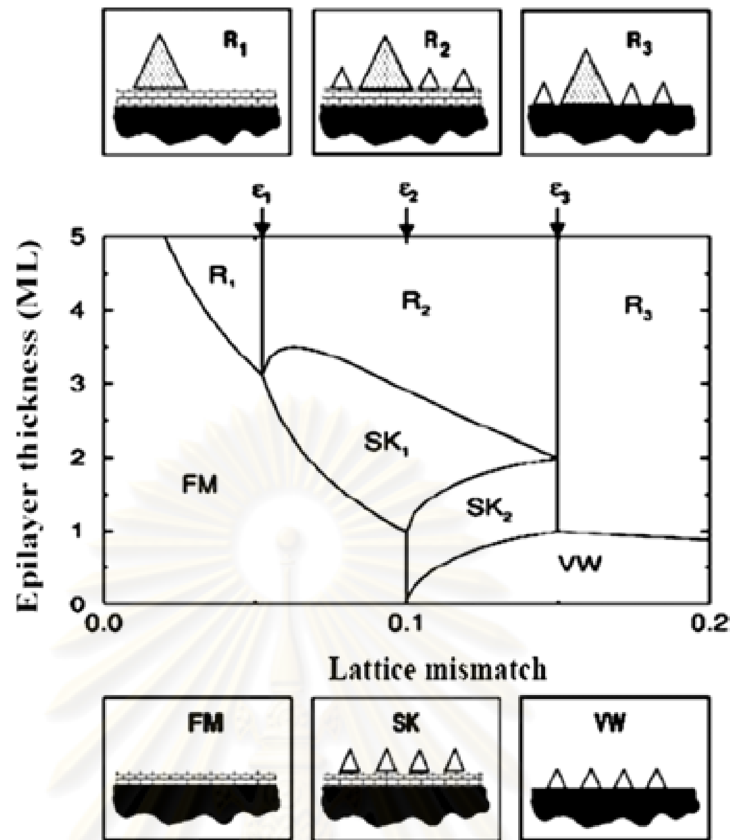

Figure 2.8 Equilibrium phase diagram of a lattice-mismatched heteroepitaxial system as a function of epilayer thickness H and the lattice mismatch. The small panels on the top and bottom illustrate the morphology of the surface in the six growth modes. The small empty triangles represent the presence of stable islands, while the large shaded area ones refer to ripened islands (Daruka and Barabasi, 1997).

The SK_1 phase

Above H_{c_1} and for $\varepsilon_1 < \varepsilon < \varepsilon_2$, the deposited material H is distributed between the wetting film, and finite stable islands, in a process similar to the SK growth mode. At H_{c_1}, the equilibrium island size jumps from zero (in the FM phase) to some finite $x_0(H, \varepsilon)$ value. Naturally, within the SK_1 phase the island size, their mass, the WL thickness, and the island density p are continuous functions of H and ε. With increasing H, the density p increases from 0 at H_c to a finite value. Interestingly, as a consequence of island-island interactions in the SK_1 phase the WL also continues to grow, but at a sub-linear rate.

ศูนย์วิทยทรัพยากร
จุฬาลงกรณ์มหาวิทยาลัย

The R_2 phase

In this phase the deposited material A is distributed between a wetting film, finite islands, and ripening islands. The finite islands formed in the SK_1 phase are preserved, being stable with respect to ripening. Thus in the R_2 phase both finite stable islands and ripening islands coexist.

The VW phase

For large lattice misfits ($\varepsilon > \varepsilon_2$) and for small coverages *H, all* the deposited material is accumulated in the form of finite islands. Due to the large misfit, in this phase the wetting film is absent and the islands form directly on the substrate, similar to the so-called VW growth mode. In the absence of the wetting film, both the island size x_0 and the island density *p* simply increase with *H.*

The SK_2 phase

By increasing H in the regime $\varepsilon_2 < \varepsilon < \varepsilon_3$ we reach a new phase when *H* exceeds the value H_{c_4} which we label the SK_2 phase. In this phase the behavior of the system is quite different from the SK_1 growth mode, since at the H_{c_4} boundary we already have islands formed in the VW mode. As we enter the SK_2 phase by increasing *H* above H_{c_4}, the island density and the island size remain unchanged, but a wetting film starts to form. This process continues until a full monolayer is completed, at which point we enter the SK_1 phase. Thus, in contrast with the SK_1 phase, in SK_2 phase the formation of new islands is suppressed until the one-monolayer-thick WL is completed.

The R_3 phase

In this last phase, which occurs for $\varepsilon > \varepsilon_3$ and for $H > H_{c_3}$ we expect the formation of ripening islands. The formation of stable islands is suppressed, and all the material deposited after H_{c_4} contributes only to the formation of new *ripening* islands, that *coexist* with the stable islands which had been formed in the VW growth mode. However, in contrast with R_2, in the R_3 phase the wetting film is absent. The summarized solution is that the stability of the islands depends only on coverage (*H*) and sufficiently large coverage can enhance the possibility to ripened islands without dependence of the value of lattice mismatch (ε).

2.4.2.2 Kinetic Analysis

The kinetic model for the time-dependent 3D island density for semiconductor heteroepitaxy is explained by the island using a mean-free theory by Dobbs et al. (1997). This model describes how this density varies with growth conditions. Theoretical analysis of SK growth kinetics for the island density using growth rate equation is based on the physical processes of adatom deposition, surface diffusion, attachment and detachment of adatoms from the islands as follows: the atoms deposit and adsorb to the growing surface.

The deposited atoms on the growing surface known as adatoms diffuse over the surface and collide with one another. After colliding, the adatoms form 2D islands. The small 2D islands with sizes less than critical thickness are thermodynamically unstable and quickly broken up into adatoms again. Further deposition of adatoms results in larger 2D islands. They are stable by capturing the adatoms more and transforming into 3D islands when their sizes exceed the critical sizes.

By applying the above model, the density of 3D islands formed during the deposition of InP QDs on GaP-stabilized GaAs (001) (Dobbs et al., 1997) are studied. The experimental results shows that island density increases with the growth rate and decreases with the growth temperature. It is worthy to note that the island density also increases consistently with increasing the deposition and then saturates. No significant changes in the island density for further deposition but leads to the island size. This limited size of QDs idea can also simply be explained from the self-limiting effect proposed by Seifert et al. (1996). Many authors have already described the limited size of QDs form the kinetic aspects (Seifert et al., 1996; Chen and Washburn, 1996; Jesson et al., 1998).

Figure 2.9 illustrates the strain energy density along the surface of the WL and around an island. The change in this energy density due to the formation of 3D islands affects the chemical potential. The top of the island, where the partial strain relaxation in the island takes place, is located at the minimum in the potential whereas the edge of the island, where high compressive strain exists, is at the maximum in the potential. The propagation of compressive strain at the island edge increases an inherent misfit strain between the substrate and the wetting layer around the island. The increase in

the potential around the coherent island depends on the island size and so its formation has a self-limiting effect on island growth. This outcome will be achieved to understand the coherent view of the kinetic analysis of self-assembled QDs formation. In the next section, defects and dislocations in QDs formation will be briefly discussed.

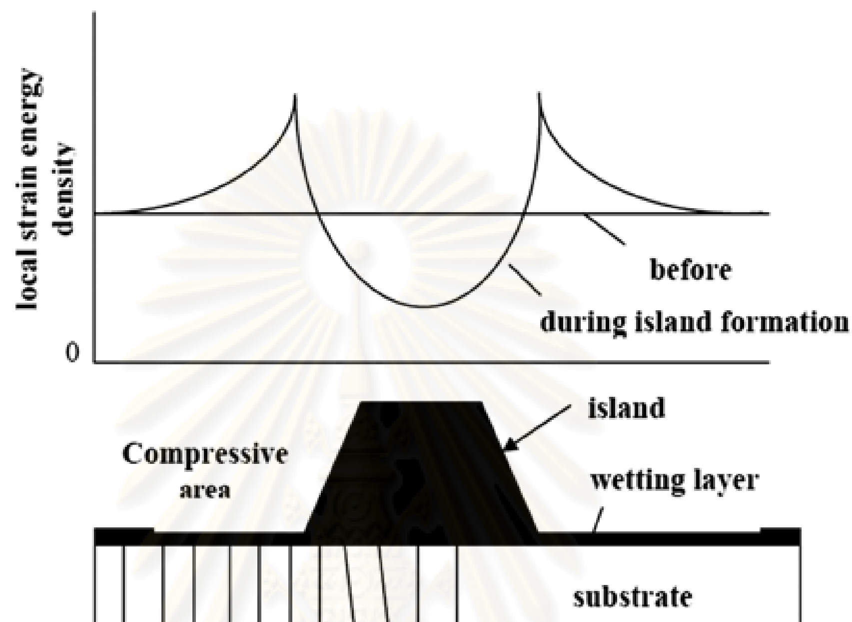

Figure 2.9 Schematic representation of the local strain energy density in and around the 3D island (Seifert et al., 1996).

2.5 Defects and Dislocations

The characteristics of a semiconductor are influenced by the strain. This section will briefly present strain in the context of semiconductor heterostructures in order to understand the strain epitaxy. The issues associated with strains such as defects and dislocations in strained heterostructures are explained. Especially, the strained behaviour related to the dislocation mechanism which is one of the important matters of this work is discussed in this section.

2.5.1 Strain

When an overlayer that has a different lattice constant from a substrate is grown on the substrate, the resulting epitaxy is called a strained epitaxy. The strained behaviour

of heterostructure is related to the dislocation mechanism. The main reasons why the strained heteroepitaxy is interested in are two facts. They are (i) incorporation of the built-in strain and (ii) generation of a new effective substrate. In the strained epitaxy, a thin overlayer has a built-in strain which effects on the electronic and optoelectronic properties of material. In a lattice-mismatched heterostructure, strain energy is relieved by the generation of misfit dislocations (MDs) when the overlayer thickness exceeds a critical thickness (h_c) and eventually the overlayer becomes its own substrate. This process allows the substrate possibility of growing in semiconductor technology.

The strain (ε) between the two different materials due to lattice mismatch is defined by

$$\varepsilon = \frac{a_l - a_s}{a_s} \qquad (2.9)$$

Where a_s and a_l are lattice constants of substrate and overlayer, respectively. The accommodation of lattice of the epitaxial layer with the substrate is shown in **figure 2.10**. In the strained heteroepitaxy, the lattice constant of the epitaxial layer in the

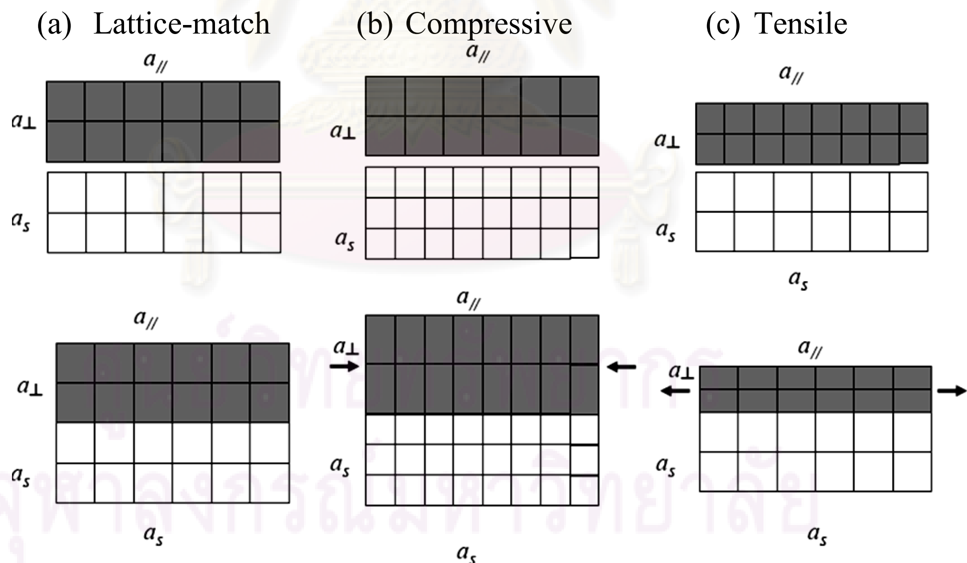

Figure 2.10 Schematic representations of (a) unstrained layer, (b) compressive strained layer and (c) tensile strained layer. The opened squares represent atoms of the substrate materials and closed squares are atoms of the epitaxial materials. In (b) and (c) the lattice constants of the epitaxial layers are different from the substrate materials. The arrows in (b) and (c) represent forces (stresses) exerted on the epitaxial layer.

direction parallel to the interface is forced to be equal to the lattice constant of the substrate while the direction perpendicular to the substrate is changed by Poisson effect. Under the compressive strain, the parallel lattice constant ($a_{//}$) is forced to shrink and the perpendicular lattice constant ($a_{\perp}$) will expand. In this case, the diffraction peaks from a epilayer (at θ_e) and substrate (at θ_s) in XRD spectrum are located as shown in **figure 2.11(a)** for the symmetric reflection from (00*l*) planes. Conversely, under a tensile strain, $a_{//}$ will expand and $a_{\perp}$ will shrink. In this case of smaller cubic lattice constants in a coherent epilayer, the observed diffraction peaks are shown in **figure 2.11(b)**.

In the strained epitaxial growth, the lattice constants of the strained film in the direction parallel and perpendicular to the interface are

$$a_{//} = \frac{a_l d_1 + a_s d_0}{d_1 + d_0} \quad \text{(2.10)}$$

$$a_{\perp} = (1 - \sigma f)\, a_1 \quad \text{(2.11)}$$

where d_1, d_0 are lattice constants of film and substrate and σ is a Poisson ratio which is given by

$$\sigma = \frac{C_{11}}{2C_{12}} \quad \text{(2.12)}$$

where C_{11} and C_{12} are elastic constants of the epitaxial layer. The C_{11} and C_{12} for InAs are 8.329×10^{11} and 4.526×10^{11} dyn/cm^2 and for GaAs are 11.88×10^{11} and 5.38×10^{11} dyn/cm^2 respectively.

ศูนย์วิทยทรัพยากร
จุฬาลงกรณ์มหาวิทยาลัย

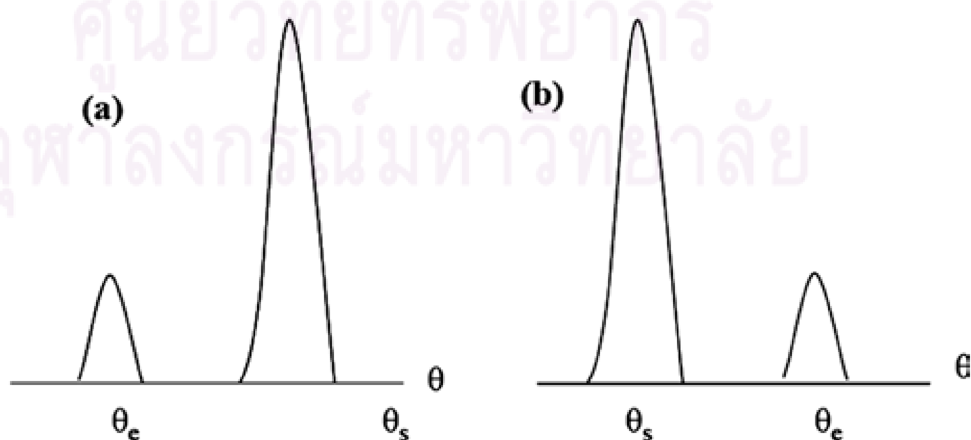

Figure 2.11 Diffraction peaks from (a) the epitaxial layer (at θ_e) and (b) the substrate (at θ_s).

To calculate the alloy composition from the lattice constant, its dependence on the composition must be determined. In the case of fully relaxed layers, $a_{\perp}$ can be measured by using Vegard's law. However, Vegard's law is no longer true for strained layer. In this case, both lattice parameters ($a_{\perp}$ and $a_{//}$) are considered to determine the alloy composition. The In concentration from the $In_xGa_{1-x}P$ alloy layers can easily be determined from the free lattice constant (a_{InGaP}) using Vegard's law which can be expressed by the following formulae:

$$a_{InGaP} = \frac{2C_{12}a_{//} + C_{11}a_{\perp}}{2C_{12} + C_{11}} \quad (2.13)$$

$$a_{InGaP} = xa_{InP} + (1-x)\,a_{GaP} \quad (2.14)$$

$$C_{11} = \frac{xa_{InP}C_{11}^{InP} + (1-x)\,a_{GaP}C_{11}^{GaP}}{a_{InGaP}} \quad (2.15)$$

$$C_{12} = \frac{xa_{InP}C_{12}^{InP} + (1-x)\,a_{GaP}C_{12}^{GaP}}{a_{InGaP}} \quad (2.16)$$

The important concept in strained layer epitaxy is critical thickness. Critical thickness arises because of a competition between strain energy and chemical energy. Below the critical thickness, minimum energy state of the bilayer system is achieved by strain. Above the critical thickness, the minimum energy state is achieved by the formation of dislocations (Bhattacharya, 1994).

If the coherent strain becomes relatively large either due to a large lattice mismatch or a large thickness of the epitaxial layer, the strain energy is reduced by the formation of dislocation at the interface which is given by (Bhattacharya, 1994)

$$E_{st} = f^2 \left(C_{11} + C_{12} - \frac{2C_{12}^2}{C_{12}}\right) d_1 \quad (2.17)$$

The critical thickness as a function of strain is given by (Fritz et al., 1985)

$$\varepsilon = \frac{a_s}{\sqrt{2}\,h_c}\frac{(1-\sigma/4)}{2\pi(1+\sigma)}\left(ln\frac{\sqrt{2}h_c}{a_s} + 1\right) \quad (2.18)$$

where ε is the strain, h_c is the critical layer thickness, a_s is the lattice constant of the substrate and σ is Poisson ratio. This section will be an important knowledge and discussion to understand strain effect in QDs formation. As a consequence, the next

section will be briefly discussed some principles and specifics of defects in QDs formation.

2.5.2 Defects and Stress

In semiconductors, the reasons of introduction to defects and stress are either thermodynamic considerations or the presence of impurities during the crystal growth process. Therefore, the regular pattern of atomic arrangement in crystal is interrupted by defects. Four types of defects in crystalline semiconductors are generally characterized as (i) point defects, (ii) line defects, (iii) planar defects and (iv) volume defects.

2.5.2.1 Defect Classification

Crystal defects include any kind of structural irregularity in crystalline order. We can sort them into point defects, line defects, and plane defects. The line defects are usually mentioned as dislocations, and the plane defects include stacking fault, twin, or anti-phase boundaries. Dislocations can be sorted in three kinds: edge (also known as 90º or Lomer) dislocation, screw dislocation, and mixed dislocation. Basically, they are lines of atoms with broken bonds, and characterized by their Burgers vector which is a shortest path of atomic displacement (and a direction of dislocation slipping). For the edge dislocation, its line is perpendicular to Burgers vector. Screw dislocation has its line and Burgers vector parallel. Mixed dislocation could have line and Burgers vector at any angle between 0 and 90º, and they are characterized by this angle.

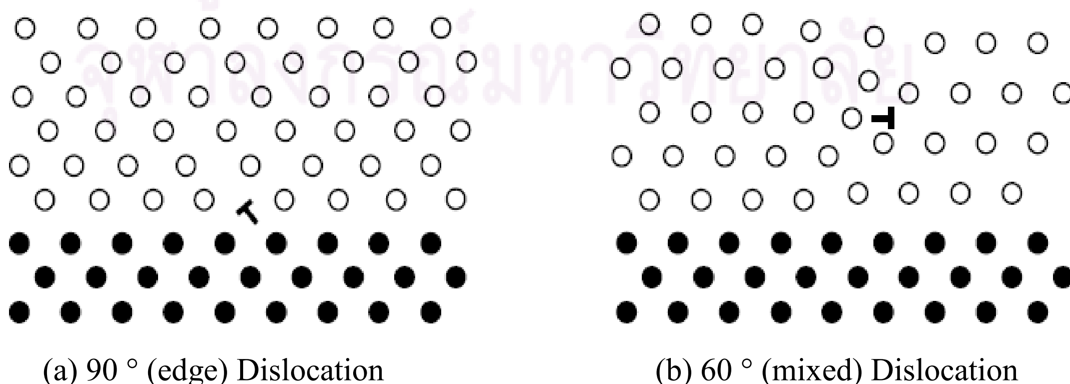

(a) 90 ° (edge) Dislocation (b) 60 ° (mixed) Dislocation

Figure 2.12 Illustration of (a) 90 °edge dislocation and (b) 60º mixed dislocations

For epitaxially grown III-V semiconductors, most commonly seen dislocations are edge and 60º dislocations. They are illustrated in **figure 2.12**. The edge dislocation relieves geometry mismatch more efficiently, however, it is energetically easier to introduce 60º dislocations in III-V materials. Hence, there are mostly 60º dislocations present in a layer grown under a large lattice mismatch, such as a GaAs layer on Si. This 60º dislocation also has low energy to propagate and slip, therefore, once it is generated at a lattice-mismatched interface, it threads microns throughout the epilayer as growth proceeds. This is a reason why heteroepitaxy of III-V on Si has never been successful, since it is difficult to eliminate or terminate 60º dislocations propagation.

In the case of wafer bonding, on the other hand, it brings two perfect materials **[60]** into contact abruptly. Hence, dislocation formation mechanisms are very different (and much simple). In the case of InP vs GaAs, their lattice mismatch at room temperature is 3.7% (It is 3.6% at 600 °C. Since the difference is small, we neglect the effect of thermal expansion for simplicity. We will discuss thermal mismatch in later section). This means that every 26 atoms of InP would match with every 27 atoms of GaAs if they are placed with the same orientation. **Figure 2.13** shows a high-resolution transmission electron microscope (TEM) image of bonded interface **[61]**.

As the two materials are put in contact and brought to an elevated temperature, high enough that atomic bonding can be cut and reformed, atoms on their surfaces would rearrange themselves to form atomic bonds with each other. Among 27 of GaAs atoms, 26 atoms will find their InP mates but the remaining 1 will not. Hence, this leftover 1 atom forms a defect as shown in **figure 2.12 (a)**, i.e., an edge dislocation if defects are formed on a line penetrating the paper plane. The edge dislocation has a slip plane parallel to the interface, so it could move left or right, but it can hardly climb up into InP or GaAs layer as it is energetically difficult.

Hence, the dislocations are confined at the interface and do not affect crystalline quality of layers away from it.What happens if their surface orientations of materials bonded are different? As we saw before, the geometry mismatch at the interface is now largely affected by orientation relation of the two, and the mismatch becomes different depending on which cross-section of the interface you are looking at. **Figure 2.14** is an example of wafer bonding of orientation-mismatched (001) GaP and (110) InP **[62]**.

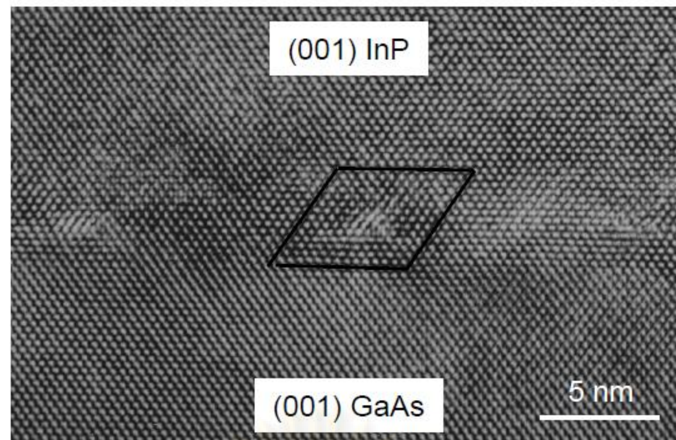

Figure 2.13 High-resolution TEM image of bonded interface of (001) InP and (001) GaAs **[61]**

As they are aligned by their [1−10] direction, the geometry mismatch in this direction is the same as the lattice mismatch of GaP and InP, which is 7.7%, so that there must be 1 defect per every 13 atoms. Whereas on the other cross-section, the mismatch is so large that they are approximately 3 atoms of InP lined up with 4 atoms of GaP. In such a case the lattice alignment is called "misfit vernier" and there is little lattice deformation. In this way, the linear dislocation density is very different depending on which crosssection to observe.

In real samples, there is another source of dislocation: tilt between InP and GaAs. The tilt exists both in vertical and horizontal orientations. The vertical tilt is from surface misorientation of commercial substrates, and horizontal tilt is from misalignment of two wafers when we place them together. This issue of tilt is already discussed elsewhere **[63]**, and since the effect of the tilt is minor compared to latticeand thermal mismatch, we do not need to discuss it here.

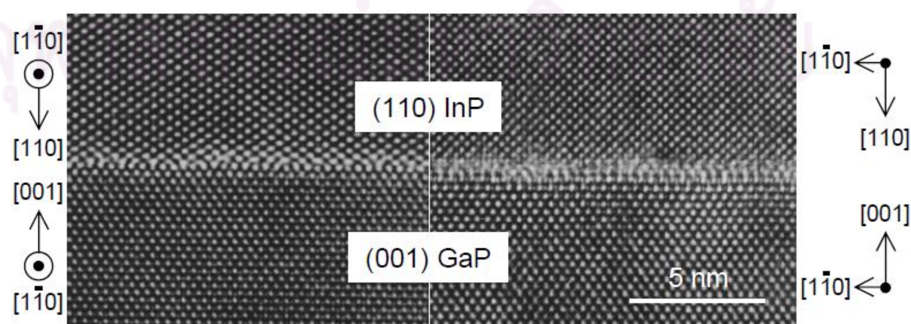

Figure 2.14 High-resolution TEM image of bonded interface of orientation-mismatched (001) GaP and (110) InP **[61]**

2.5.2.2 Point Defects

A point defect is a highly localized defect that affects the periodicity of the crystal only in one or few unit cells (Singh, 2003). The common defects which usually occur in binary GaAs compound is anti-site defect in which one of the atoms from Ga atom sits on the As sublattice instead of the Ga sublattice. Other point defect is interstitial defect where an atom sits in a site that is in between the lattice points. A schematic showing some important point defects in a crystal is shown in **figure 2.15**.

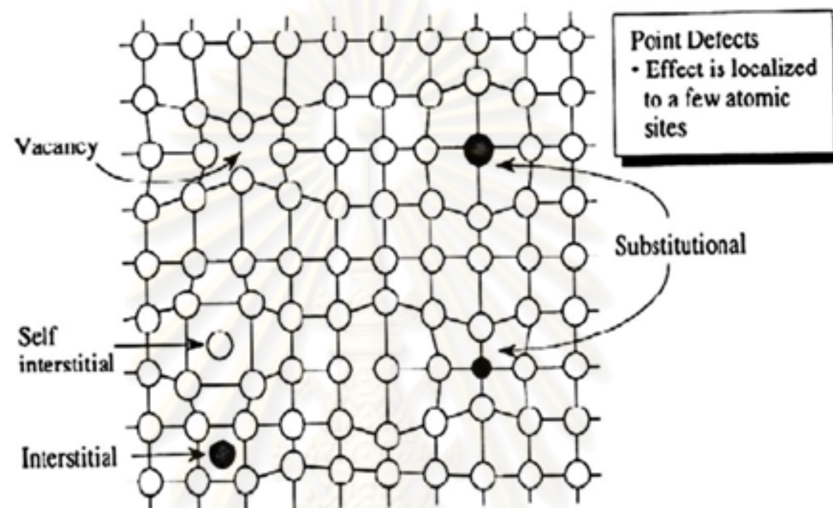

Figure 2.15 Schematic diagram showing point defects in a crystal (Singh, 2003).

2.5.2.3 Line Defects

When the large number of atomic sites is misaligned, the resulting defect is called a line defect or dislocation. There are two major types of dislocations, namely, *edge dislocation and screw dislocation*. When an extra half plane of atoms is inserted to a perfect crystal, a defect known as an edge dislocation is created in regular atomic structure along line where the extra half-plane terminates as shown in **figure 2.16(a)**.

A screw dislocation shown in **figure 2.16(b)** can be visualized as being formed by cutting the crystal pathway through with a knife and shearing it parallel to the edge of the cut by one atom spacing. The screw dislocation transforms successive atom planes into a helix around the dislocation line. The characteristic of both edge and screw dislocations is termed as mixed dislocation as shown in Fig. 3.15 (Andrew et al., 2002). The dislocations present in real crystalline solid are commonly of mixed dislocation.

Dislocations are generally described by the Burgers vectors and the dislocation line. From **figure 2.17(a)**, relaxation occurs via threading dislocation (TD) motion and MD formation on the inclined glide planes. The most common slip system is a/2(110) {111}. The Burgers vectors for this system are along the face diagonals of the cubic cell and are the shortest possible primitive lattice translation vectors. The set of possible Burgers vectors can be constructed by considering the edges of a half octahedron, as shown in **figure 2.17(b)**.

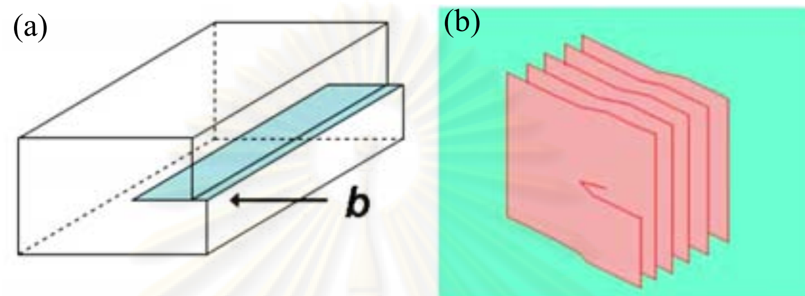

Figure 2.16 Schematic representation of (a) edge dislocation and (b) screw dislocation (http://en.wikipedia.org/wiki/Dislocation#Edge_dislocations).

The dislocation Burgers vector can be decomposed into edge b_{edge} and screw b_{screw} components. Consequently, the edge component can be decomposed into parts parallel $b_{//}$ and perpendicular $b_{\perp}$ to the film/substrate interface: $b_{edge} = b_{//} + b_{\perp}$.

In order to get a better understanding of dislocation with Burgers vector, the basic information about Burgers vector is explained. A dislocation is given in terms of the Burgers circuit. A Burgers circuit is any atom to atom path taken in a crystal containing the dislocations which forms a closed loop. The vector required to complete the circuit is called the Burgers vector. Therefore, the orientation and magnitude of a dislocation can be characterized in terms of its Burgers vector. The Burgers vector of edge dislocation is perpendicular and screw dislocation is parallel to the line of the dislocation. The schematic diagram for Burgers circuit and Burgers vector is illustrated in **figure 2.18**. In general case, the dislocation line lies at an arbitrary angle to its Burgers vector. However, the Burgers vector of the dislocation is always the same and independent of the position of the dislocation. There are two basic types of dislocation movement. They are (i) glide or conservative motion and (ii) climb or non-conservative motion. In a glide motion, the dislocation *moves in* the

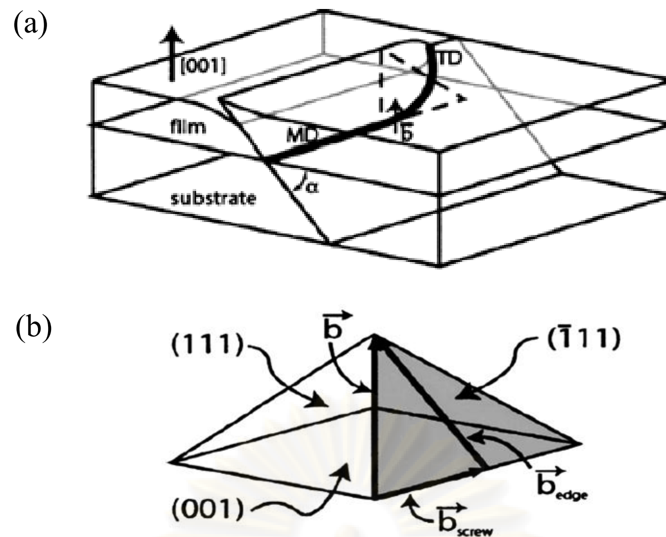

Figure 2.17 Dislocation geometry in heteroepitaxial mismatched thin films. (a) One of the inclined {111} planes for a (001) oriented fcc film/substrate system with a gliding TD segment and a trailing MD. (b) Dislocation Burgers (Andrew et al., 2002).

surface defined by its line and Burgers vector. In climb motion, the dislocation moves out of the glide surface.

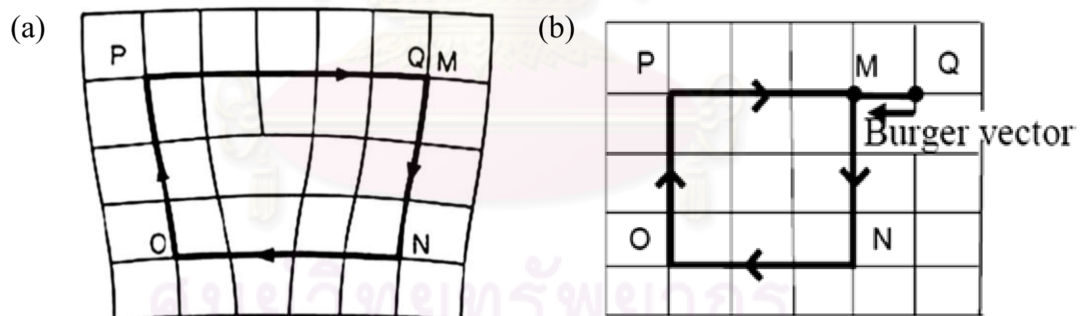

Figure 2.18 Burgers circuit (a) around a dislocation and (b) in a perfect crystal (Hull, 1965).

ศูนย์วิทยทรัพยากร
จุฬาลงกรณ์มหาวิทยาลัย

2.5.2.4 Planar and Volume Defects

Planar and volume defects are not important in single crystalline materials, but can be importance in polycrystalline materials. If the Si is grown on glass substrate, small regions of Si are perfectly crystalline but are next to microcrystallities with different orientations. The interface between these microcrystallities is called grain boundries. Grain boundaries may be viewed as array of dislocations.

Volume defects are introduced if the crystal growth process is poor. The crystal may contain regions that are amorphous or may contain voids. In most epitaxial growth techniques used in modern optoelectronics, these defects are not a problem. However, the development of new material systems such as diamond (C) or SiC are hampered by such defects.

2.5.2.5 Stress by Misfit Dislocations

A bonded interface of (113)B InP and (001) GaAs will be reported. In **figure 2.19** we show free-standing atomic order of each material at the bonded interface: (a) top view, (b) side view at (−110) cross section, (c) side view at cross section orthogonal to (b). It is a complex interface, and there may not be dislocation lines since atom positions are 50% off between neighboring atomic planes. To obtain an order of stress

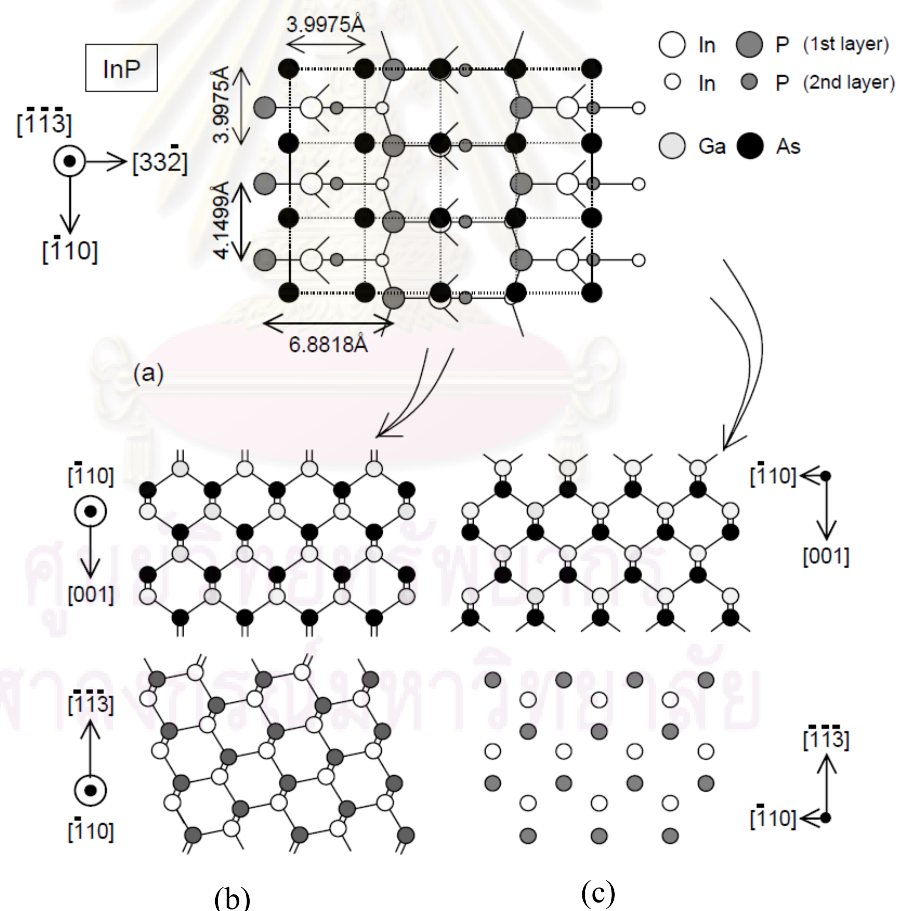

Figure 2.19 Atomic order of (113) InP and (001) GaAs: (a) top view, (b)(c) side view

magnitude by interface defects, so the very simple model and calculate stress from 1-dimentional misfit dislocation array. From the theory of J. W. Matthews, force by an edge dislocation F_{ED} is expressed as **[64]**

ศูนย์วิทยทรัพยากร
จุฬาลงกรณ์มหาวิทยาลัย

$$F_{ED} = \frac{Gb^2}{4\pi(1-\nu)}\left(\ln\frac{\mathrm{R}}{\mathrm{b}} + 1\right) \quad (2.19)$$

where b is Burgers vector length, ν is Poisson ratio, G is shear modulus, and R is a height of the edge dislocation. By dividing F_{ED} by an area that an edge dislocation affects, we can obtain dislocation stress σ_{ED} as

$$\sigma_{ED} = F_{ED}\frac{1}{R \circ S} = F_{ED}\frac{1}{R(b/\varepsilon)} \quad (2.20)$$

$$= \frac{1}{4\pi(1-\nu)}\left(\ln\frac{\mathrm{R}}{\mathrm{b}} + 1\right)\frac{\mathrm{Gb\varepsilon}}{\mathrm{R}}$$

Where

$$\varepsilon = \frac{l_{InP} - l_{GaAs}}{l_{GaAs}} \quad (2.21)$$

where S is spacing between dislocations, which can be expressed by b and a geometry mismatch ε. The parameters G and ν are orientation-dependent, but (001) values is used here since an order of magnitude need to get. As for R, in **figure 2.18**, the number of monolayers deformed at the interface is about 5-6, so there can be assume R = 10Å. Also, b = 3.9975Å. The only orientation-dependent term is ε, which is

$$\varepsilon = \frac{6.8818 - 3.9975}{6.8818} = 0.4191 \quad \text{for } [33\bar{2}] \text{ direction} \quad (2.22)$$

$$\varepsilon = \frac{4.1499 - 3.9975}{6.4.149} = 0.0367 \quad \text{for } [\bar{1}10] \text{ direction} \quad (2.23)$$

To get an idea of how much large or small these stress values are comparison of these values with the stress in strained material such as strained MQW.

2.5.2.6 Stress by thermal expansion mismatch

Another source of stress in bonded structure would be thermal expansion mismatch between the two bonded materials. That is, during cooling down the sample from bonding temperature, the two materials would shrink at different rates, so that mismatch would be generated. And at low temperatures, such mismatch cannot be relieved by creating any dislocation. The thermal expansion constants at the room temperature are listed in Appendix A. Their temperature dependence is negligible here since we want to find the order of magnitude of the strain. The thermal expansion/deflation should occur in a symmetric way no matter what orientation the materials are, so it should generate symmetric mismatch strain. If we set the bonding

temperature to be 575°C, the amount of strain generated in InP/GaAs bonded structure during cooling down to room temperature (25°C) is

$$(575 - 25) \times (6.4 - 4.56) \times 10^{-6} \approx 10^{-3} = 0.1\% \quad \text{……………..(2.24)}$$

Since GaAs shrinks more than InP, it generates about 0.1% compressive strain in InP side or 0.1% tensile strain in GaAs side. Right after the bonding, both InP and GaAs sides are equally thick (3~400 μm), so the strain is almost evenly split between them. As we etch off the InP substrate, the strain will be concentrated onto InP side, i.e., the InP active region will be under biaxial 0.1% compressive strain.

As a conclusion on thermal mismatch stress, it would be insignificant if the gain medium is a strained MQW, to which strain of about 1% is intentionally added. However, if the strain in the gain medium is small, this thermal mismatch strain could become significant and the main source of asymmetric stress, thus affecting the polarization. Aside from affecting the properties of gain medium, the thermal stress would cause wafer bowing which would be an obstacle for a large-scale wafer bonding. This problem can be estimated by thinning the substrates or employing thin film transfer technology.

2.5.3 Dislocations

There are many models for the generations of MDs. MDs are associated with TDs and extend into a film growing epitaxially on the substrate. The formation of MDs for the strained layer heterostructures for various lattice-mismatched systems are shown by both qualitatively (Shiryaev, et al., 1997; Liu et al., 1999; Samonji, et al., 1999; Takano et al., 2005) and quantitatively (Andrew, et al., 2002; Hoagland, et al., 2004).

2.5.3.1 Critical Thickness for $In_xGa_{1-x}P$ Growth on GaAs

A particular technological interest regards on the InP/InGaP/GaAs structure, in which an InGaP layer is deposited on a GaAs substrate. InGaP can be matched to GaAs, when the Indium molar fraction is 48.84% and Gallium, consequentially, is the 51,2%, yielding an Energy gap of 1.88 eV (at room temperature). $In_{0.48}Ga_{0.52}P$, has interesting properties like a low electron effective mass, 0.111 m_0, high mobility (1850 cm^2/Vs at room temperature) and a direct band gap **[65]**. It can be mainly used

in HEMTs, HCTs, pumping lasers for optical fibre amplifiers, doped with Erbium **[66]**, but also for tandem cells in space applications and in combination with Al (AlGaInP) for high efficiency LEDs (emitting in green, yellow, orange and orange-red colours light).

The case of InGaP/GaAs is particularly complex, from the literature review, the mismatch versus the Indium fraction in the alloy and the critical thickness (thickness above which the growing layer relaxes producing structural defects) as a function of the Indium fraction are observed. The InGaP/GaAs heterostructure is indeed very sensitive to the stoichiometric composition: a slight variation of the composition from the lattice match causes a consistent deformation of the layer lattice (high mismatch), therefore a high parallel strain. This mismatch produces an elastic energy accumulation at the interface, which enhances as the layer thickness increases.

The lattice bears the consequent accumulation of elastic energy up to a certain value, corresponding to a critical thickness, above which all the stored energy forces the layer to a plastic relaxation, accompanied by the formation of a large amount of dislocations. The Mattews and Blakeslee model **[67]** predicts the critical thickness for InGaP on GaAs and it is connected to the Indium percentage in the alloy by the Vegard's law **[68]**:

$$a_{InGaP} = x a_{InP} + (1-x) a_{GaP} \quad \text{(2.25)}$$

While epitaxy restrictions generally limit materials growth to material with the same lattice constant, it is possible to make brief excursions to materials of different lattice constants. When a lattice mismatch film is grown on a substrate epitaxially, the epilayer is generally restricted in thickness by the Matthews-Blakeslee condition **[69-71]**. The Matthews-Blakeslee condition, base on a force balance model, represents the thickness limit for a strained film before dislocations begin to form. These dislocations, interruptions in the periodicity of the perfect lattice, are devastating for semiconductor lasers because they serve as nonradiative recombination centers. The critical thickness of a film (h_c) is defined as:

$$h_c = \frac{1}{2} \frac{a_s\left(1-\frac{1}{4}\nu_l\right)}{\varepsilon_{ll}(1-\nu_l)\pi}\left[1+\ln\left(\frac{h_c\sqrt{2}}{a_s}\right)\right] \quad \text{(2.26)}$$

Where a_s is the unstrained lattice constant of the substrate and a_f is the lattice constant of the epilayer. The strain within the plane ε_{ll} is given by

$$\varepsilon_{ll} = \frac{a_s - a_f}{a_f} \quad \text{.......................................(2.27)}$$

and the Poisson's ratio, ν, is given as:

$$\nu_l = \frac{C_{12}^{film}}{C_{11}^{film} - C_{11}^{sub}} \quad \text{.......................................(2.28)}$$

where C_{11} and C_{12} are materials properties representing the film and substrate's mechanical behavior. The Matthews-Blakeslee analysis is for that of an epitaxial film, growing by the Frank- Vander Merwe mechanism, extending infinitely in either direction within the plane and growth perpendicular to the plane. Table 2.1 contains values for common semiconductor materials at or near room temperature **[72-75]**.

Table 2.1: Parameters for common semiconductor materials at or near room temperature

	GaAs	InP	GaP
a (A°)	5.65325	5.8687	5.4505
C_{11}(dyn/cm^2)	11.9×10^{11}	10.11×10^{11}	4.05×10^{11}
C_{12}(dyn/cm^2)	5.34×10^{11}	5.61×10^{11}	6.20×10^{11}
ν_L[100]	0.31	0.36	0.31

2.5.3.2 Types of Misfit Dislocations

There are two types of MDs in (001) epitaxial zinc-blende crystals or diamond cubic systems for low lattice mismatched (001) interfaces. They are α type and β type dislocations that are classified according to the termination of dislocation core. The dislocation line along the [1-10] direction with P atoms at the core is defined as α type dislocation. On the other hand, the dislocation lines along [110] direction with Ga atoms at the core are known as β type dislocation (Wu et al., 1999). Many research groups have investigated asymmetries of dislocation lines. Abrahams et al. (1969) suggested that the occurrence of such an asymmetries effects are due to differences in the nucleation or mobility of these two types of dislocations (Abrahams et al, 1969). Kuesters et al. (1986) reported that the velocity of α type dislocation is much greater

than that of β type dislocation under the investigation with TEM results. Kavanagh et al. (1988) investigated the dislocation densities, surface morphology and strain of InGaP/GaAs epitaxial interfaces as a function of indium composition and layer thickness by TEM, medium energy ion blocking and doublecrystal x-ray diffractometry. They claimed that asymmetries in dislocation densities are due to unequal distribution of Burgers vector of 60º type or edge type dislocation densities in the strained layer which in turn responsible for the strain asymmetry in strained layer (Kavanagh et al., 1988). Many experimental results additionally confirm that the argument of asymmetry in MDs along <110> direction.

2.5.3.3 Surface Steps via Threading Dislocation

Hongland et al. (2004) reported influence of surface steps on glide of TDs during layer growth. They demonstrated the surface step via the glide of TD, which is energetically favorable when the thickness of the layer exceeds a critical value, is shown in **figure 2.20**. This group quantitatively proved that critical values for MDs are larger than predicted by traditional stepless solution from the energy point of view required to form a unit length of dislocation with edge and screw Burgers vector components, b_e and b_s respectively on the interface. The TDs elongate to form MD segments during the growth of $GaAs/In_xGa_{1-x}As/GaAs$ under the investigation by TEM measurement are shown in **figure 2.21** (Liu et al., 1999). The surface steps are seen as 2D arrays so-called cross hatch when we look at from the top as seen in plain view of AFM and TEM images in **figure 2.22 (a)** and **(b)** (Yastrubchak et al., 2003).

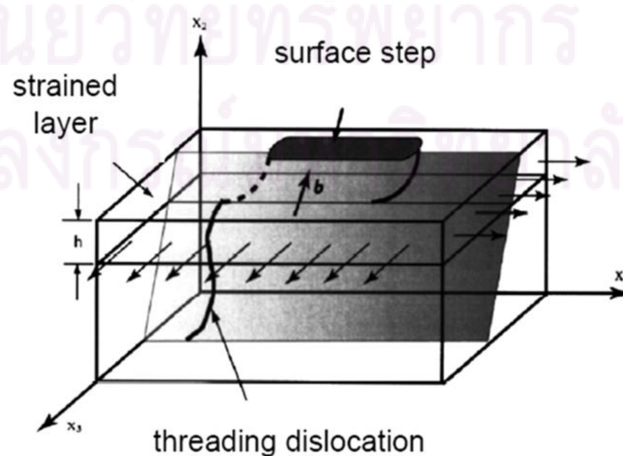

Figure 2.20 Geometric of appearance of surface step via gliding of threading dislocation with Burger vector *b* (Hongland et al., 2004).

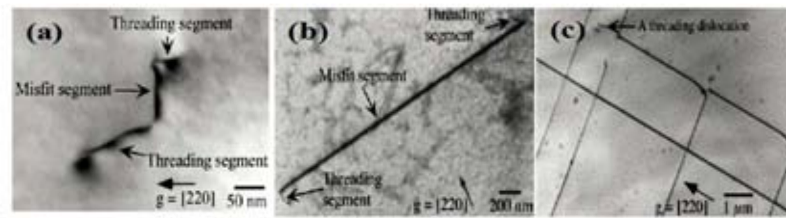

Figure 2.21 TEM images showing dislocation observed in GaAs/$In_{0.15}Ga_{0.85}As$/GaAs for various thicknesses (h) of InGaAs layers (a) misfit dislocation segment (h=6 nm) (b) elongated misfit dislocation segment (15 nm) and (c) misfit dislocation network with threading dislocation (h=25 nm) (Liu et al., 1999).

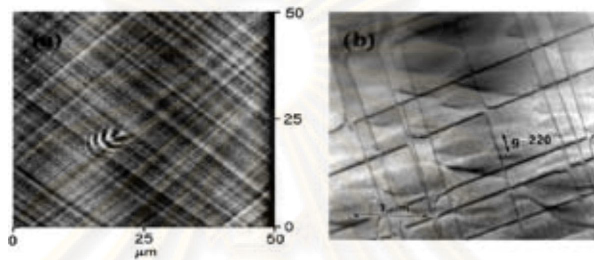

Figure 2.22 (a) AFM and (b) TEM images of cross-hatch pattern for $In_{0.25}Ga_{0.75}As$/GaAs (001) (Yastrubchak et al., 2003).

Since the Burgers vector makes an angle of 60º to the line direction, this type of MD is commonly called a 60° dislocation. One of primary features of the dislocation structure is V-type configuration emerging from interface between substrate and strained layer into surface buffer layer in InGaAs/GaAs strained layer superlattices structure (Rajan et al., 1987). The apex angle of the V-shape is ~70°. They claimed that the formation of V-shape is due to annihilation of inclined MDs segments of expanding slip loops originating in the MD network. TEM image of V-shape configuration is shown in **figure 2.23**.

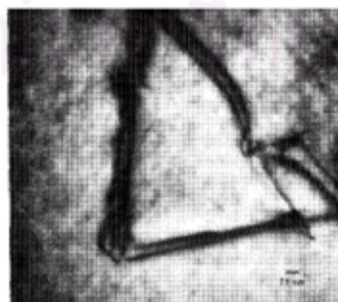

Figure 2.23 TEM image showing V-shape configuration resulted from inclined slip loops originating in misfit dislocation network (Rajan et al., 1987).

2.5.3.4 Lomer Type Misfit Dislocation

In heteroepitaxial growth, pure edge (Lomer type) misfit dislocations (L-MDs) are the most efficient at misfit strain. Pure edge MDs have been obtained on many heteroepitaxial systems such as SiGe/Si, Ge/GaAs, GaAlAsP/GaAs, GaAlAsSb/GaSb and InGaAsP/InP with (001)-oriented substrates (Vdovin et al., 1996); {111} (Ernst et al., 1993); {112} (Mitchell at al., 1991) substrate orientations.

The number of L-MD fraction in the MD network depends on the lattice mismatch, growth thickness, epitaxial layer composition and temperature or annealing (Hull and Bean 1989; Hull et al., 1989). In the paper of Vdovin et al. (1997), two typical types so-called A type and B type in L-MDs of pure edge MDs characterized by different geometrical properties have been observed for different epitaxial systems **[76]**.

A type L-MDs are in a form of curved lines leaving the interface and greatly deforming the MD network. After that, they are generated via interaction of the parallel 60°-MDs pre-existing at the interface. B type L-MDs are long and difficult to identify generation mechanism which are frequently observed in the MD networks with low MD linear density. The schematic configuration for the generation L-MD of pure edge MD is shown in **figure 2.24** (Vdovin, 1997). Both types are determined by the growth conditions and the mobility of individual dislocations in the film. The common dislocation node for initial 60° MDs, arising as a result of the dislocation reactions in crossing points of the MDs, is a starting point for the generation of pure edge MDs **[77]**. The MD propagation is accompanied by a shift of dislocations from interface upwards onto the epilayer or downwards onto the substrate.

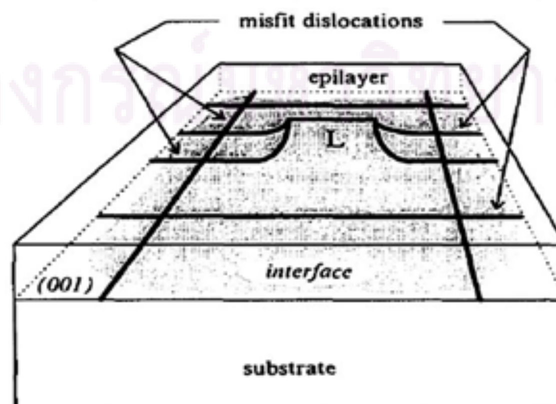

Figure 2.24 Schematic drawing of the spatial dislocation configuration for the case of L-MD which is commonly found in pure edge MD (Vdovin, 1997).

2.6 Growth Techniques

Many order QDs growth techniques are reviewed in this part such as multi step (Kitamura et al., 1995; Akiyama et al., 2006) In-interruption growth (Hong et al., 2006), thin-cap and regrowth (Suwaree et al., 2006) and atomic force tip-induced nano-oxidation, atomic-hydrogen etching/cleaning and regrowth techniques (Kim et al., 2006).

2.6.1 Multi Steps Technique

Kitamura et al. (1995) demonstrated that the alignment of QDs along surface steps for (001) GaAs substrates misoriented by 2° toward [010], [110], and [1-10] using multiatomic step structures in MOCVD growth. In this technique, first, GaAs epilayer with multi atomic steps structure is grown on a vicinal GaAs substrate under appropriate growth conditions. Then, InGaAs quantum dots are grown on a vicinal substrate. **Figure 2.25** visualizes the alignment of InGaAs QDs with a diameter below 20 nm along multiatomic surface steps for the [010] misoriented surface.

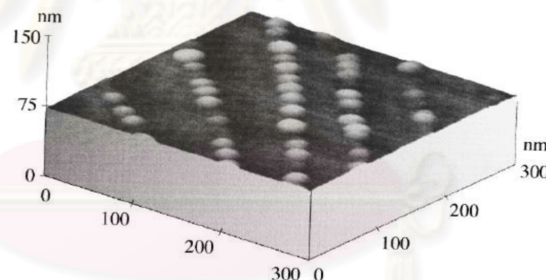

Figure 2.25 AFM image (300 nm×300 nm) of InGaAs QDs aligned multiatomic steps on GaAs (001) surface misoriented by 2° toward [101] direction (Kitamura et al., 1995).

InGaAs QDs arrays aligned on vicinal (111)B GaAs substrate tilted 8.5° towards the [-10-1] direction have been reported by Akiyama et al. (2006). First, SL buffer layer consisting of ten periods of 3 nm GaAs/ 10 nm AlGaAs are grown on the (111)B GaAs substrate. Then, 50-nm-thick GaAs layer are deposited at a substrate temperature 600°C onto the SL buffer layer, a bunching of atomic steps called quasiperiodic corrugation of about 20 nm in period and about 2 nm in height are induced as shown in **figure 2.26(a)**. It is worthy to note that they used low growth rate

of GaAs, 0.05 nm/s and high As_4/Ga flux ratio is 500-700 in order to be effective in making the multiatomic steps quite straight and almost periodic.

The AFM image of InGaAs QDs grown by depositing 3-nm-thick $In_{0.3}Ga_{0.7}As$ layer at Ts 520°C is shown in **figure 2.26(b)**. Each train of island is aligned along the [-101] direction, parallel to the underlying GaAs multiatomic steps. The array of island trains has the average period of about 50 nm, which is nearly twice as large as that of underlying GaAs multiatomic steps. The height of islands are 3-5 nm and lateral sizes are about 50-60 nm along the island trains. Neighboring islands are separated by small gaps of about 5-10 nm. The average density of islands is 3×10^{10} cm^{-2}. This explanation gives some critical issues concerning the growth techniques. The following section will focus on the presentation of In-interruption growth technique.

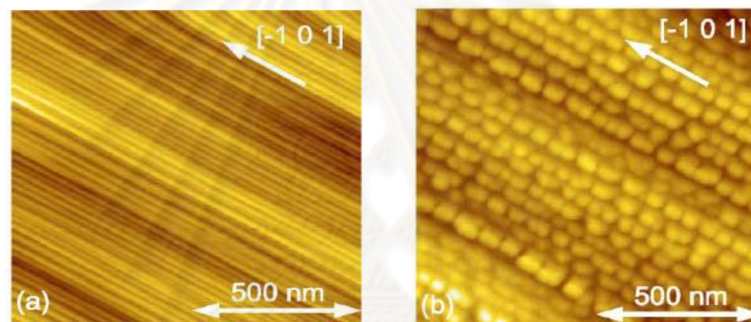

Figure 2.26 AFM image (a) of multiatomic steps on GaAs layer grown on a vicinal (111)B GaAs and (b) InGaAs islands by growing 3-nm-thick

2.6.2 In-Interruption Growth Technique

Ordered quantum dots (QDs) on a more conventional GaAs (100) substrate using In-interruption growth technique shown in **figure 2.27 (a)** are obtained without doing any complicated steps which was proposed by Hong et al. (2006).

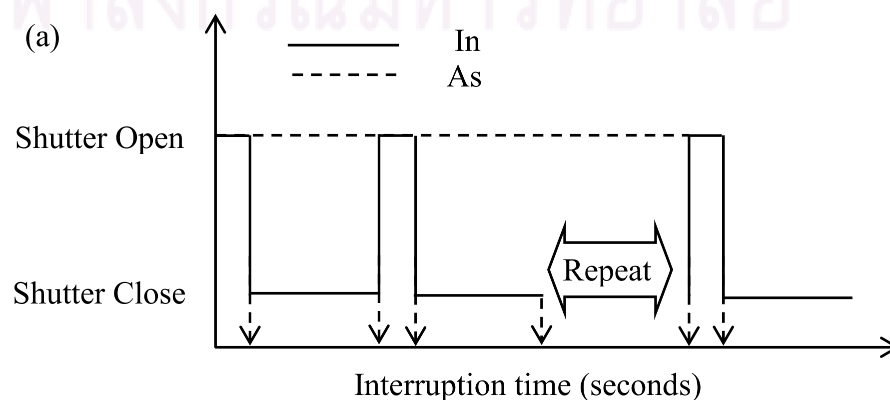

(b)

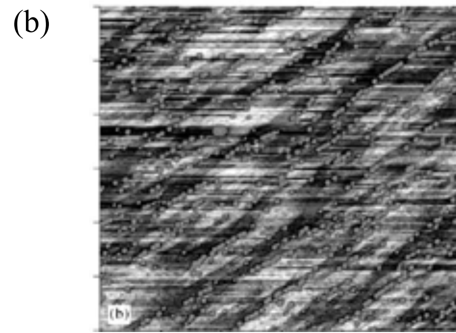

Figure 2.27 (a) Schematic drawing of In-interruption growth technique and (b) AFM image (3000 nm×3000 nm) of InAs QDs with a In-interruption time 9 sec (Hong et al., 2006).

Indium atoms are interrupted while arsenic atoms supplying all the time during the growth of QDs. Therefore, In sources arriving at the substrate have a migration time to reach a more suitable site and this effect results in aligned QDs. AFM image of InAs QDs with 9 sec In-interruption time is shown in **figure 2.27 (b).**

2.6.3 Thin-Capping and Regrowth Technique

In this section, a review of thin-capping and regrowth technique, base on some experimental work will be presented. The initial part is devoted to the InAs QDs growth by thin-capping and regrowth technique base on the experimental work of Suwaree. A thin-capping and regrowth molecular beam epitaxial technique is proposed and demonstrated to be a suitable approach for the growth of lateral quantum-dot molecules (QDMs). Recently, ordered InAs QDs grown on GaAs (001) substrate using a thin-capping and regrowth of QDs technique is demonstrated by Suwaree et al. (2006). By using a conventional QDs growth technique, as-grown randomly distributed QDs are formed on flat surface firstly. Then, on top of these QDs layers, thin GaAs layer (6ML) is capped. Because of the lattice mismatch between the QDs and capping layer, the strain energy around the QDs is increased. Correspondingly, In atoms migrate out from the QDs and leave a nanohole in the middle of the QDs. By regrowing the QDs on top of nanoholes via a thin-capping process, nanopropeller QDs are formed. By repeating the thin-capping-and-regrowth process for 7 cycles at the regrown thickness of 0.6 ML, nanopropeller QDs are aligned along the [1-10] direction. AFM images of evolution of laterally aligned QDs along [110] are shown in **figure 2.28**.

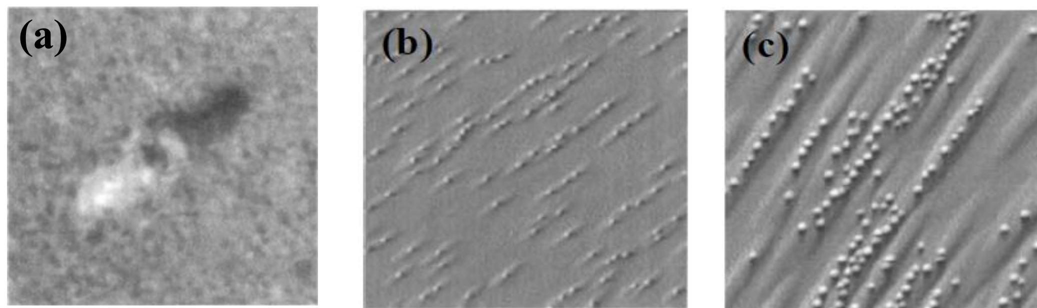

Figure 2.28 AFM images of (a) nanohole (b) 1 cycle (c) 7 cycles of thin-cap and regrowth of QDs on nanoholes (Suwaree et al., 2006).

2.6.4 Atomic Force Tip-Induced Nano-Oxidation, Atomic-Hydrogen Etching/ Cleaning and Regrowth Technique

Even more recently, the combination of atomic force microscope tip-induced nano-oxidation, atomic-hydrogen etching/cleaning and regrowth of InAs QDs by using droplet epitaxy technique is performed by Kim et al. (2006). A promising way to obtain site-controlled QDs with high quality based on the patterning and regrowth process, which can reduce the interface defects and contaminants between QDs and nanoholes to a negligible level, is suggested. Nano-oxide dots on GaAs surface are created by AFM tip-induced nano-oxidation in a contact mode. Then, these nano-oxide dots are removed by soft etching in order to form nanoholes. Finally, indium is

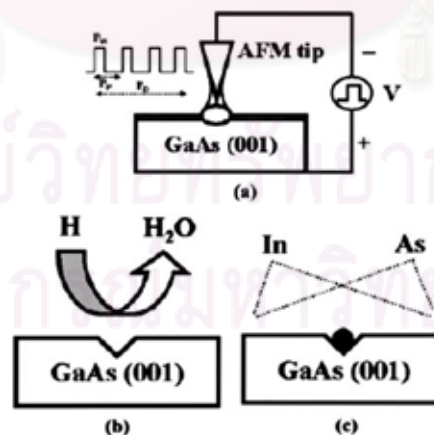

Figure 2.29 The schematic illustration of the experimental processes for (a) the formation of the nano-oxide dots on GaAs (001) surface by AFM tip induced oxidation, (b) the subsequent removal of a nano-oxide dot and native oxide layer by atomic hydrogen irradiation and (c) the deposition of InAs QDs on nanoholes by droplet epitaxy.

ศูนย์วิทยทรัพยากร
จุฬาลงกรณ์มหาวิทยาลัย

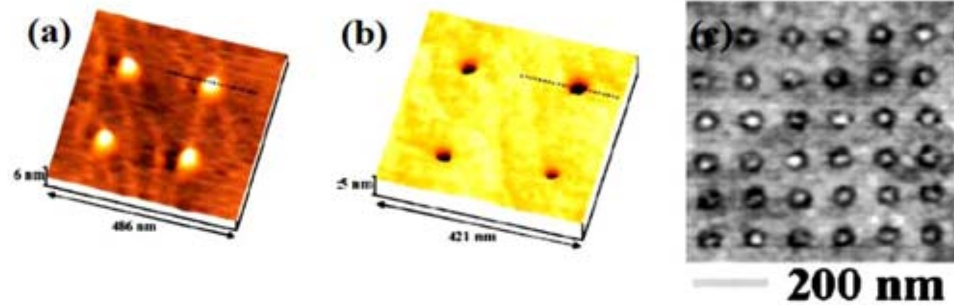

Figure 2.30 AFM images of (a) nano-oxide dots (b) nanoholes and (c) InAs QD arrays grown by droplet epitaxy (Kim et al., 2006).

supplied by droplet epitaxy method. The schematic illustration of the experimental procedures is shown in **figure 2.29** and the AFM images of grown nanostructures by atomic force tip-induced nano-oxidation, atomic-hydrogen etching/cleaning and regrowth technique is shown in **figure 2.30**.

The aim of this chapter has been to make understanding with the self-assembled nanostructures and it will be cover to use in fabricating quantum structured semiconductors. Its mainly focus on self-assembling as one of the most promising method to produce quantum dots. These include especially the phenomena of strain, defect, dislocation and other growth mechanism concern with self-organization. This discussion will open the doors for completely new realization of quantum structured semiconductors.

ศูนย์วิทยทรัพยากร
จุฬาลงกรณ์มหาวิทยาลัย

CHAPTER III

Self-Assembled Quantum Dots Growth and Characterization Techniques

3.1 Self-Assembly by Molecular-Beam Epitaxy

Self-assembled QDs can be obtained by Molecular Beam Epitaxy (MBE). MBE is an epitaxial growth technique which is based on the interaction of beams of atoms and molecules of thermal energy on a heated crystalline surface under ultra-high-vacuum (UHV) conditions **[78]**. In MBE, the constituent elements of a semiconductor in the form of „„molecular beams"" are deposited onto a heated crystalline substrate to form thin epitaxial layers.

One of the most useful tools for in-situ monitoring of the growth is Reflection High Energy Electron Diffraction (RHEED). It can be used to calibrate growth rates, observe the removal of oxide from the surface, calibrate the substrate temperature, monitor the arrangement of surface atoms, determine the proper arsenic overpressure, give feedback on surface morphology, and provide information about growth kinetics **[79]**.

3.1.1 Basics of Molecular-Beam Epitaxy

Fabrication of high-quality quantum dots requires a method for high-precision epitaxial growth of high-purity semiconductor crystals, such as molecular-beam epitaxy. Since its invention in the early 1970"s, MBE has grown from a specialized research tool to a major industrial technique **[80, 81]**. **Figures 3.1(a)** and **(b)** show a schematic of a typical MBE mechanism. Elemental sources are heated in ultra-high vacuum (UHV) to produce molecular beams, which impinge on a heated substrate.

Atomic layer-by-atomic layer deposition is achieved by using low beam fluxes, which are controlled by varying the temperature of the source cells. The atomic mean-free path in the beams is generally larger than the distance between the source and the substrate. Typical growth rates of $0.1 - 1 \mu m/hr$ are obtained. The shutters in front of the sources are used to control growth time. Uniform growth is obtained by rotating the substrate during deposition. In order to obtain low impurity levels, a background

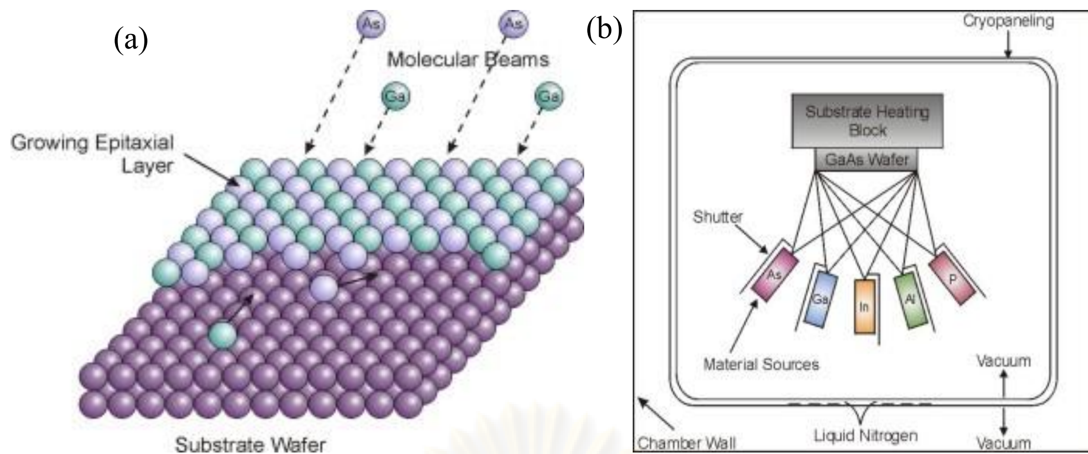

Figure 3.1 (a) MBE mechanism and (b) Schematic diagram of MBE process

pressure of less than 5×10^{-11}Torr is maintained. The UHV environment allows for in-situ monitoring of growth conditions and growth rate by reflection high-energy electron diffraction (RHEED), laser reflectrometry, or other methods. Layer-by-layer epitaxy of lattice-matched materials is possible within a range of growth rates and substrate temperatures.

The mechanisms of this growth mode are described by the Burton-Cabrera-Frank theory. According to this model, growth proceeds according to the following steps: (1) Atoms impinge on the sample surface, where they are adsorbed; (2) The atoms migrate along the surface towards atomic steps, where they are stabilized by the increased number of atomic bonds; (3) The atoms migrate along the step edges to a kink site, where they are incorporated into the lattice.

Deposition involves the lateral motion of step edges or the growth of two-dimensional islands until an atomic layer is completed. The materials most commonly grown by MBE are known as III-V compounds, because they are composed of one element from Group III of the periodic table, and one element from Group V. In particular, we grow InP, GaAs, AlAs, InAs, and alloys of these materials. Deposition is typically done on the (100) surface of a GaAs substrate.

A special advantage of MBE, compared to other growth techniques, is that a computer-controlled shutter in front of each cell allows precise control over layer thickness and composition. The mechanical shutters in front of the sources can be closed and opened in less than 1 second. The temperatures of the sources can be

accurately controlled. The composition of the epilayer and its doping level depend on the relative arrival rates of the constituent elements and dopants, which in turn depend on the evaporation rates of the appropriate sources. This makes it possible for MBE to grow sub-atomic layers.

3.1.2 Molecular Beam Epitaxy (MBE) System Overview

A typical MBE machine consists of four chambers: load chamber, introduction chamber, transfer chamber, and growth chamber. These chambers are separated by isolated gate valves and the samples are transferred from one chamber to another by a magnetic arm. The introduction and the growth chambers have heaters for a heat treatment process (preheat) of the substrate. Ultra-high vacuum condition is obtained via a pumping system which consists of sorption pump, ion pump, and titanium sublimation pump.

The schematic drawing of a typical MBE growth chamber is shown in **figure 3.2(a)**. Inside the growth chamber are material source cells, substrate heater, monitoring equipment, and a pumping system. The solid-source materials are separately contained in different effusion cells. During growth, the chamber wall and the effusion cells are cooled with liquid nitrogen from heated parts. Two types of monitoring equipment are used: mass spectroscopy and reflection high-energy electron diffraction (RHEED).

The mass spectroscopy is used for particle analysis while RHEED is used as a tool to observe surface crystalinity. There are two ionization gauges which measure the beam flux and background pressure (BP). One of the ionization gauges measuring for BEP is located at the same level of manipulator behind the substrate heater and the other gate is situated in front of the ion pump for measuring the background pressure. The temperature is measured by W-Re thermocouples and controlled by computer via a controller card (EUROTHERM). In order to get a uniform flux profile on the substrate"s surface, the substrate is continuously rotated by a motor during epitaxy. In this work, quantum dots composed of InP within an InGaP matrix were elaborated by molecular beam epitaxy on semi-insulating (100) oriented GaAs substrates using a Riber 32P system shown in **figure 3.2 (b)**. The substrate is attached to a molybdenum block (MO). Prior to the crystal growth, contaminations are removed from the

substrate surface by a 3-hour pre-heat process in the introduction chamber before being transferred to the growth chamber. The preheat process is done when the pressure in the introduction chamber is 1×10^{-8} Torr or lower. The temperature profile of the pre-heat process is shown in **figure 3.3**.

In the pre-heat process, the sample is heated by increasing the substrate temperature (T_{sub}) from 30°C to 450°C at a rate of 7°C/min. This ramp up is taken 1hour. During the ramp up, the contaminations from the substrate surface are removed and purged; the pressure inside the introduction chamber thus increases. When the T_{sub} reaches 450°C, it is held for 1 hour. Then, T_{sub} is ramped down from 450°C to 30°C. The pre-heat process thus takes 3 hours in total and all samples are subject to this process without exception. After the pre-heat process, the samples is transferred to the growth chamber and de-gas process is carried out. In de-gas process, the temperature of each cell is increased from the standby temperature (T_{std}) to the required temperature in order to remove the contamination from each cell.

After de-gas processes which prepare the cells for growth, the substrate has to go to the de-ox process in order to prepare the surface for subsequent epilayer growth. All samples in this work are composed of InP grown on $In_xGa_{1-x}P$ matrix. The lattice mismatch of 3.8% between InP and $In_{0.48}Ga_{0.52}P$ (lattice matched to GaAs) drives the

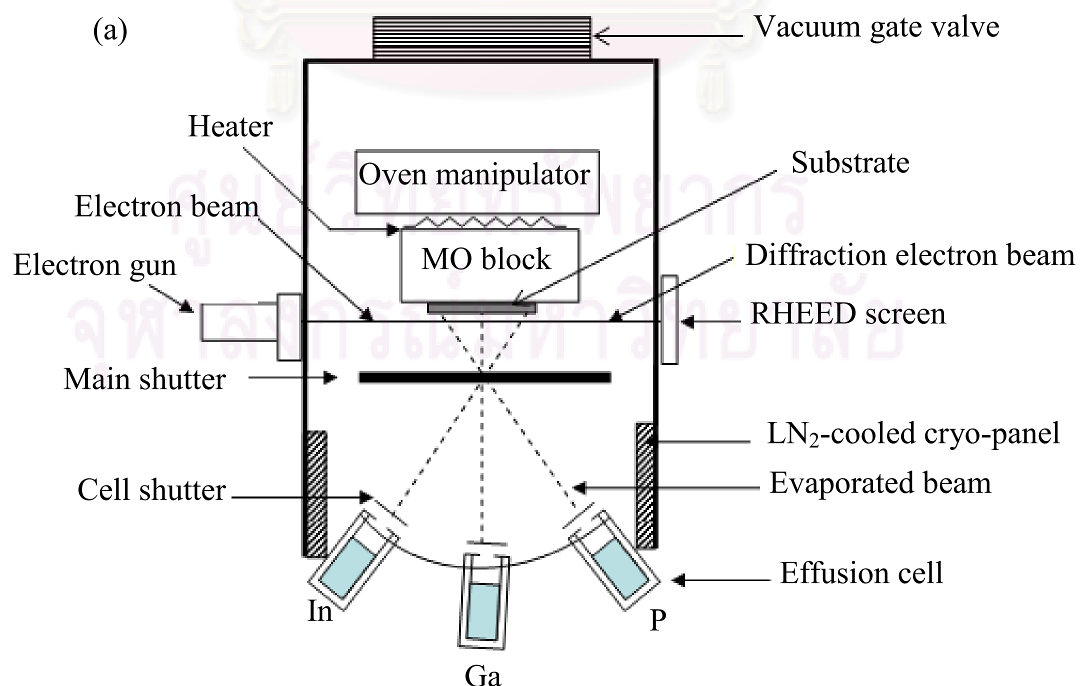

Figure 3.2 (a) Schematic diagram of the growth chamber of MBE system

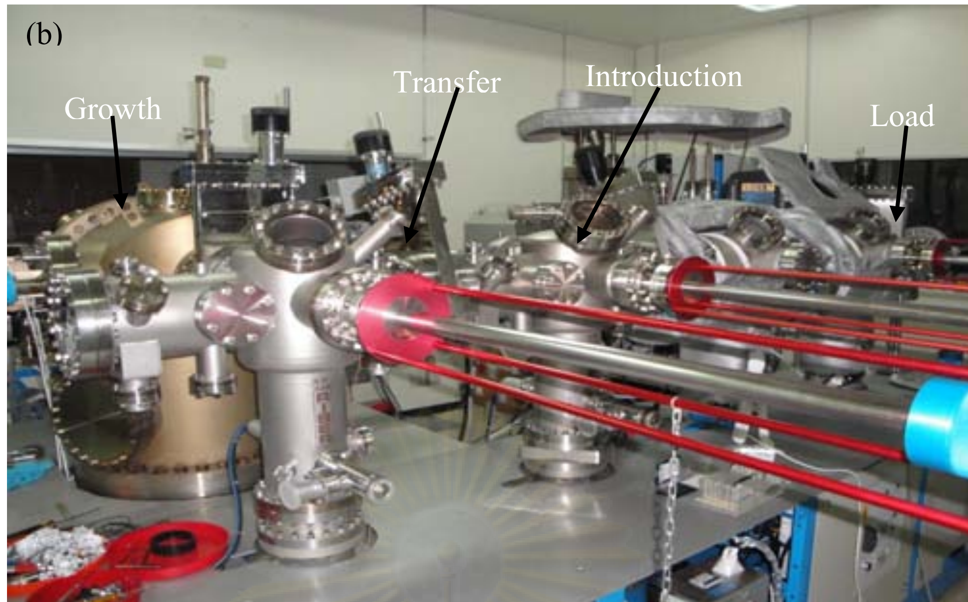

Figure 3.2 (b) A photograph of RIBER 32P MBE system

strain- induced the formation of QDs via the Stranski-Krastanow growth mechanism. The growth process was monitored by using 15kV reflection high-energy electron diffraction (RHEED) system. When T_{sub} is around 580°C, a spotty pattern starts to occur because the native outside come out of GaAs surface. To ensure complete oxide removal and thus a clean GaAs surface, the temperature is kept at slightly above the de-ox temperature. Usually, if $T_{deoxide}$ = 580 °C, the temperature would be kept at 590°C until the CO peak is flat. The removal of native oxide was performed by heating the substrate under As_4 beam at 600°C until the streaky pattern appeared.

After oxide desorption, a 300 nm thick GaAs buffer layer was grown at 580°C and followed by a 200 nm $In_{0.48}Ga_{0.52}P$ grown at 480°C. After the deposition of 300 nm

Figure 3.3 Temperature profile of the preheat process

GaAs, the growth was interrupted to change from As to P rich ambient. Then, GaP insertion layers with 0-4 monolayers were grown prior the growth of InP QDs. Finally, the QDs were fabricated by deposited 3ML InP with temperature of 450°C at growth rate 0.5 ML/s. The schematic representation of the vertical layer structure of InP QDs embedded in InGaP barrier grown on (100) GaAs substrate by changing the thickness of GaP insertion layers is shown in **figure 3.4**. The relatively low temperature was chosen in order to inhibit In incorporation from the barrier into the QDs during their self-assembly **[82]**. All other growth parameters are kept at the same conditions and only change thickness of GaP insertion layers thickness in this samples growth process. All the structural characterization of these samples will be discussed in the next chapter 4.

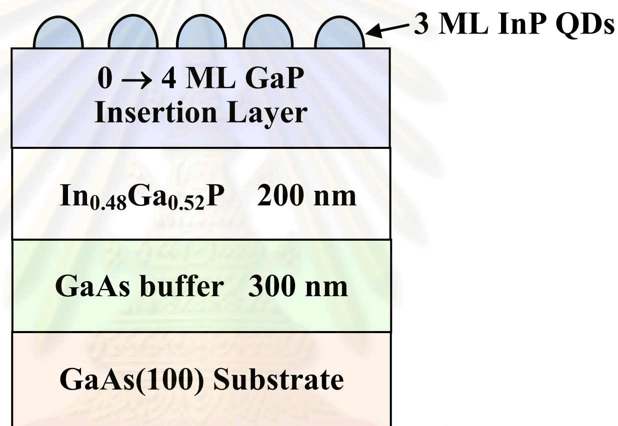

Figure 3.4 Schematic diagram of the vertical layer structure of InP QDs embedded in InGaP barrier grown on (100) GaAs Substrate.

3.1.3 In-Situ Characterization Tools

Two important in-situ characterisation tools are mass spectroscopy and RHEED. Mass spectroscopy is used to investigate the chemical constitutes inside the growth chamber. RHEED is used to calibrate the growth rates and to indicate the 2D to 3D growth mode transition point.

3.1.3.1 Mass Spectroscopy (An introduction to Mass Spectroscopy, Ashcroft)

Mass spectrometry is an analytical technique used to measure the mass-to-charge (m/z) ratio of ions. The composition of a sample can be determined from the mass spectrum representing the masses of sample components. A typical mass spectrometer

comprises three parts: an ion source, a mass analyzer, and a detector system. A schematic diagram of mass spectrometer is shown in **figure 3.5**. The sample has to be introduced into the ionization source of the instrument.

Once inside the ionization source, the sample molecules are ionized, because ions are easier to manipulate than neutral molecules. These ions are extracted into the analyzer region of the mass spectrometer where they are separated according to their mass-to-charge ratios. The separated ions are detected and this signal sent to a data system where the m/z ratios are stored together with their relative abundance for presentation in the format of a m/z spectrum.

The analyzer and detector of the mass spectrometer, and often the ionization source too, are maintained under high vacuum to give the ions a reasonable chance of travelling from one end of the instrument to the other without any hindrance from air molecules. The entire operation of the mass spectrometer, and often the sample introduction process also, is under complete data system control on modern mass spectrometers. In all experiments, masses of the particles such as hydrogen, helium, argon, water, oxygen, carbon dioxide and carbon monoxide are checked by mass spectrometer. Specifically, the complete removal of native oxide from the substrate surface is investigated by mass spectrometer. In the de-ox process, when the signal of 28 peak (carbon monoxide) is almost flat, further growth process is continued.

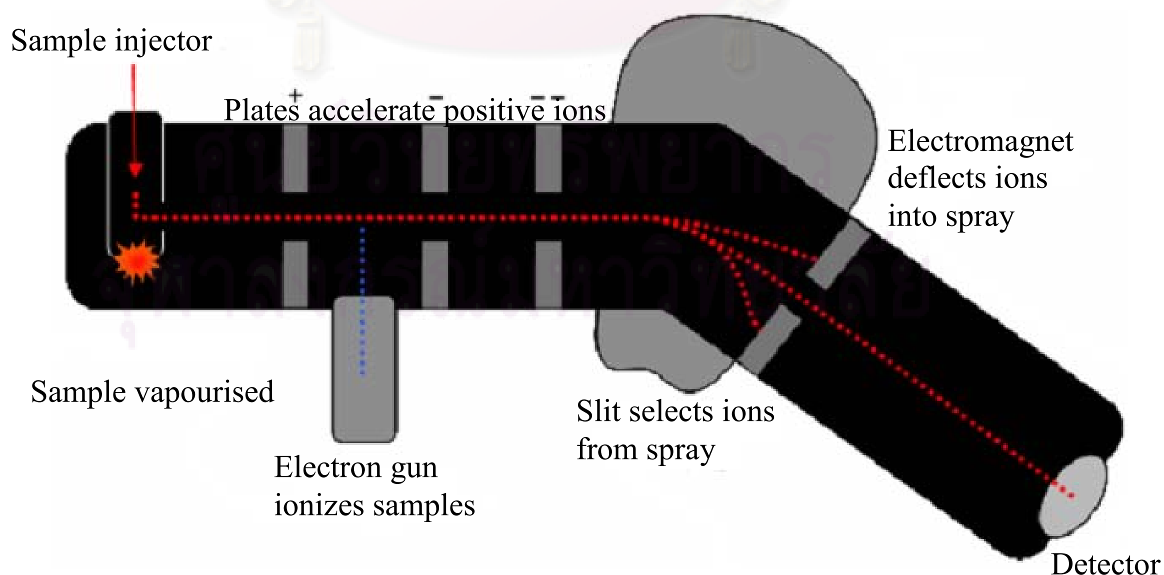

Figure 3.5 A schematic diagram of mass spectrometer stev. (http//www.stev.gb.com/science/spectroscopy.html)

3.1.3.2 Reflection High-Energy Electron Diffraction (RHEED)

The reflection high-energy electron diffraction (RHEED) intensity oscillation technique has been extensively used to study interface formation and interrupted growth effects in the preparation of heterojunctions, quantum wells and superlattices. Reflection high-energy electron diffraction (RHEED) is also the analytical tool of choice for characterizing thin films during growth by molecular beam epitaxy, since it is very sensitive to surface structure and morphology. In particular, RHEED is well suited for use with molecular beam epitaxy, a process used to form high quality, ultrapure thin films under ultrahigh vacuum growth conditions. It is remarkably simply to implement, requiring at the minimum only an electron gun (10 to 20 keV), a phosphor screen, and a clean surface. In addition to semiconductor growth processes RHEED has also been used to obtain real-time information on the top monolayers of a surface during surface phase transitions. **Figure 3.6** shows a schematic of RHEED observation system.

A RHEED system in MBE requires an electron source (gun), photoluminescent detector screen and a sample with a clean surface although modern RHEED systems have additional parts to optimize the technique. The electron gun generates a beam of electrons which strike the sample at very small angle relative to the sample surface. A high energy beam (3-100 keV) is directed at the sample surface at a grazing angle, has a very strong effect on both diffraction and its interpretation. The electrons are diffracted by the crystal structure of the sample and then impinge on a phosphor screen mounted opposite to the electron gun. Because of its small penetration depth,

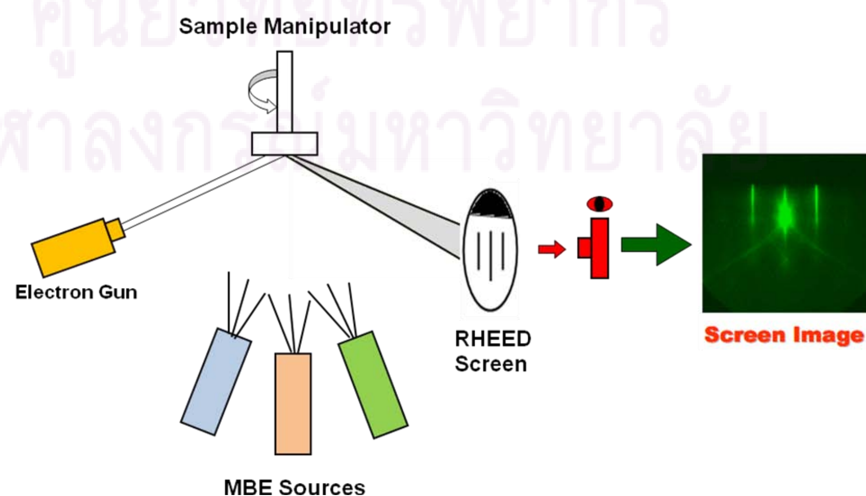

Figure 3.6 A schematic of RHEED observation system

owing to the interaction between incident electrons and atoms, RHEED is primarily sensitive to the atomic structure of first few planes of a crystal lattice. The resulting pattern is a series of streaks. The distance between the streaks is being an indication of the surface lattice unit cell size. **Figure 3.7** shows an example of RHEED patterns of temperature calibration process of GaAs.

The grazing incidence angle ensures surface specificity despite the high energy of the incident electrons. If a surface is atomically flat, then sharp RHEED patterns are seen. If the surface has a rougher surface, the RHEED pattern is more diffuse. This behaviour can lead to 'RHEED oscillations' as a material is evaporated onto a surface. RHEED is therefore of particular use with MBE. RHEED is an in-situ characterization and surface diffraction analysis technique due to the glancing incident angle of the high energy electron beam. As a result, the resulting diffraction pattern is characteristic of only the top few monolayers of the structure. Diffraction patterns are a result of the constructive interference of the diffracted electrons that obey Bragg"s law and do not undergo any scattering losses.

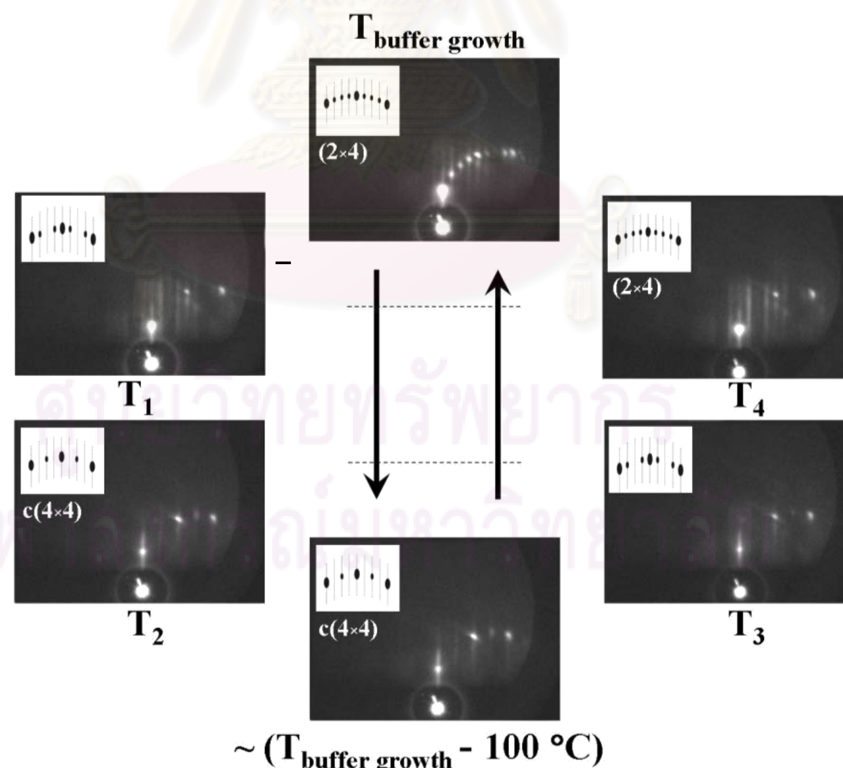

Figure 3.7 The RHEED pattern transition of temperature calibration of temperature calibration process of GaAs [110] azimuth ($T_{transition}$ (500 °C) = $(T_1+T_2+T_3+T_4) / 4$)

3.2 Metal-Organic Vapor Phase Epitaxy

Metalorganic chemical vapor deposition (MOCVD), also often called metalorganic vapor phase epitaxy (MOVPE), was invented in the end of 1960s and since then became the most important growth method for optoelectronic devices. Many epitaxial techniques are currently available for the growth of compound semiconductor materials, including liquid-phase epitaxy (LPE), chloride vapor phase epitaxy (ClVPE), hydride vapor phase epitaxy (HVPE), as well as chemical beam epitaxy (CBE), MBE and MOCVD. Recently, MBE and MOCVD have become the most popular techniques for the development of semiconductor nanophotonics, especially in QDs, due to their abrupt interfaces and atomic layer control.

Unlike the aforementioned techniques, MBE is conceptually simple. Elemental sources are evaporated at a controlled rate onto a heated substrate under ultrahigh-vacuum conditions. In the ultrahigh-vacuum environment, the growth of an atomic layer can be well controlled and monitored by reflection high energy electron diffraction (RHEED). Molecular beam epitaxy is the ultimate research tool for the production of complex and varied structures. However, it has some limitations for commercial applications. The maintenance and operations of UHV systems are expensive. Their throughput is limited by the relatively low growth rate.

In general, devices that are produced by MBE and MOCVD have very similar performance characteristics. The major advantages of MOCVD over MBE are their versatility and the suitability for large-scale production. Metal organic chemical vapor deposition is also the most economic technique, particularly for the mass production of devices. Therefore, efforts in the research, development and production of MOCVD have increased rapidly over the last two decades. Many types of commercial MOCVD equipment for different purposes have been developed to grow high-quality materials and further fabricate optoelectronic devices, such as lasers, light emitting diodes, transistors and so on.

3.2.1 MOVPE System Overview

Metal-Organic Vapor Phase Epitaxy (MOVPE) is now the most industrially important technique for III-V semiconductor epitaxy, as well as molecular beam epitaxy (MBE).

Figure 3.8 Photo of AIX 200/4 MOVPE system

As the name implies, the sources of group III (Al, Ga, In) are organic molecules in this technique. In this subsection, the MOVPE would be introduced with illustrating the machine used in this research. In this work, MOVPE growth process is carried out using model number AIX 200/4 system from AIXTRON. Photograph of this MOVPE system is shown in **figure 3.8**. The sources for group III are Trimethylgallium (TMGa) ,Trimethylindium (TMIn), and that for group V are Tertiarybuthylarsine (TBAs) and the Tertiarybuthylphosphine (TBP). The source for n-doping is Dimethylzinc (DMZn), and that for p-doping Hydrogen Sulfide (H_2S). The basic properties of these sources were listed in **table 3.1**. In these sources, except for the TMIn is solid and H_2S is vapor, others are liquid at the thermostat bath temperature. In other MOVPE systems, AsH_3 and PH_3 are often used as the sources for the V group, however, partially for safety concerns, almost all of the sources are organic solutions in our system. Purified H_2 gas is guided to each source tank through mass flow controllers (MFC), and saturated vapor is carried out to “Run” line or “Vent” line through other MFC‟s. Depicted in **figure 3.9** is the schematic configuration of the MOVPE machine.

The pressures in all of the gas lines are auto-controlled with pressure controllers. “Run MO” line is used to mix all of the saturated H_2 gas containing group III as well as zinc sources, and guide into the reactor chamber with a stable flow rate. “Vent MO” line is used to collect the unused saturated gas and guide it into the phosphor-trap filter and then scrubber. “Run Hydride” and “Vent Hydride” lines play the same

roles for group V and sulfur sources. Differential pressure meters are placed between "Run MO" line and "Vend MO" line, as well as between "Run Hydride" line and "Vend Hydride" line, to monitor the pressure difference and thus prevent reverse flows at the point of link up before phosphor-trap filter. An important technique to be noted for sharp epitaxial interface in MOVPE is the use of dummy line.

In the process of epitaxy, the MFC regulation steps are kept to a minimum number of times, since the the regulation requires a certain length of time, which results in a broad interface between different epitaxy layers. For this purpose, the injection of the source-containing gas into the "Run" line is not a simple open/close valve, but a switch valve between "Run" line and "Vent" line. Basically, when the source-containing gas is switched from "Vent" line to "Run" line, the same quantity pure H_2 dummy gas would be switched from "Run" line to "Vent" line through dummy lines, to maintain a stable flow in the "Run" and "Vent" lines. Since the speed of this switching is much faster than the MFC regulating, the epitaxy with sharp interfaces between different epitaxy layers is possible. The high quality layer interface is vital for thin film epitaxy, like multi-quantum wells (MQW).

Table 3.1: Basic Parameters of MOVPE Sources **[83]**

Elements	Sources	Molecular Weight	Fusing Point	Boiling Point	Vapor Pressure $log_{10}P$ [Torr] T: Temperature [K]	Thermostat Temperature [Degree]
In	Trimethyl-indium(TMIn)	159.9	88.4	133.8	10.52-3014/T	17
Ga	Trimethyl-gallium(TMGa)	114.8	-15.8	55.7	8.07-1703/T	0
As	Tertiarybuthyl-arsine(TBAs)	134.1	-1	68	7.243-1509/T	17
P	Tertiarybuthyl-phosphine(TBP)	90.1	4	54	7.5857-1539/T	17
Zn (p-dopant)	Dimethyl-zinc(DMZn)	95.4	-42	46	7.802-1560/T	-10
S (n-dopant)	Hydrogen Sulfide (H_2S)	34.1	-82.9	-60.19	----	----

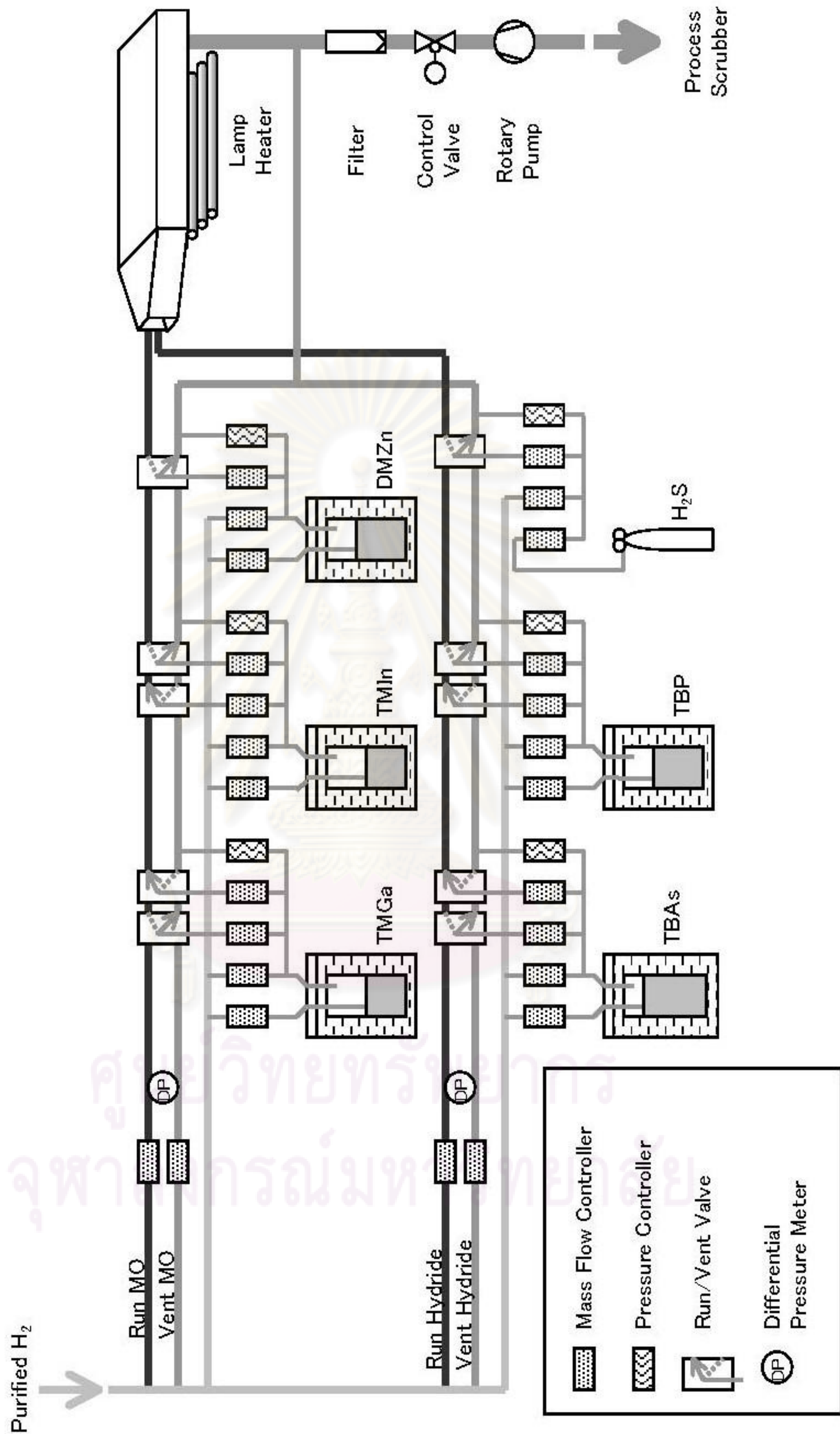

ศูนย์วิทยทรัพยากร
จุฬาลงกรณ์มหาวิทยาลัย

Figure 3.9 Schematic configuration of MOVPE system used in this research.

3.2.2 MOVPE Growth Mechanism

Metal Organic Vapor Phase Epitaxy (MOVPE) has become the most popular epitaxial growth technology for industrial production of III-V semiconductor devices. In the MOVPE of III-V semiconductors like InP, a carrier gas (usually H_2) brings a controlled amount of source materials into a high temperature reactor. The reactor is so designed that gas flow is not turbulent over the susceptor, on which the substrate with mirror-polished surface is placed. Usually the group III source gases are metal-organics, like Trimethyl-gallium (TMGa), Trimethyl-indium (TMIn) or Trimethyl-aluminum (TMAl). The group V sources can be Arsine (AsH_3) and Phosphine (PH_3), but due to their poisonous nature our reactor (AIXTRON 200/4), uses Tertial-butyl-arsine (TBAs) and Tertial-butyl-phosphine (TBP) under constant monitoring for H_2 leak and reduced ambient pressure. n-type dopant is introduced by Silane(SiH_4), H_2S or H_2Se, while the p-type dopant can be introduced by Di-methyl-zinc (DMZn).

At normal temperature and pressure, the metal-organic sources are liquid, and the temperature and pressure of their cylinders are well controlled. The carrier gas that is bubbled into the cylinder bring saturated vapor of chemical with it into the reactor. Due to high temperature in the reactor, the source molecules crack into smaller molecules and become highly activated. Reaction between group III and group V sources produce the solid shoot, with is deposited on top of the substrate. In reality, there are complicated processes like gas diffusion, adsorption, and evaporation. Since the group V atoms tend to easily evaporate from the surface, partial pressure of group V sources are kept much higher than the group III sources to prevent bad surface.

The growth rate (GR) depends on temperature in the low temperature region, but at higher temperature growth rate is relatively temperature independent, depending more on the supply of group III sources. At even higher temperatures, GR tends to fall due to increase rate of evaporation. Usually the growth is done in the temperature independent region where GR can be well controlled by control and switching of the source gas flow by mass flow controllers. **Figure 3.10** shows a schematic of the reactor used in this research (AIXTRON AIX200/4). The reactor is a lateral chamber with a graphite susceptor. The gas flow can be switched instantaneously by a run and vent method, enabling relatively sharp interface for quantum dots and wells.

In all MOVPE samples growth processes, quantum dots composed of InP embedded in $In_{0.49}Ga_{0.51}P$ matrix were carried out in a horizontal MOVPE reactor _AIXTRON, AIX200/4 (shown in **figure 3.10**) with a rotating substrate holder on nominally (001) oriented GaAs substrate. The inlet of the reactor is divided into two parts: Group-III precursors were introduced from the upper inlet and group-V precursors were introduced from the lower inlet. Hydrogen gas was used as the carrier gas for precursors and as coolant between the inner reactor and the outer tube. The reactions occur in a rectangular inner liner tube, which has a graphite rotator as a sample susceptor. During MOVPE growth processes, GaAs substrates were placed at the center of the susceptor. For InP and GaAs growth, trimethylgallium (TMGa) and trimethylindium (TMIn) were used as the group-III precursor with a hydrogen carrier and tertiarybutylarsine (TBAs) and tertiarybutyl- phosphine (TBP) were used as the group-V precursor.

Epitaxial growth conditions were a total pressure of 100 mbar, H_2 total flow rate of 13,000 sccm_sccm denotes cubic centimeter per minute at STP_, temperature of 610 °C, and V/III ratio of source precursors of 18 for InP. Lattice-matched $In_{0.49}Ga_{0.51}P$/GaAs structures are becoming major III-V semiconductor systems because, compared to AlGaAs/GaAs systems, they have lower reactivity with oxygen, and more reduced DX centers and lower interfacial recombination rates. Fabrication of InP SAQDs in InGaP/GaAs systems is difficult by metal organic vapor phase epitaxy (MOVPE), mainly due to the exchange between As and P. The other causes that contribute to the difficulty include the ordering effect of InGaP and the segregation of In in the InGaP layer.

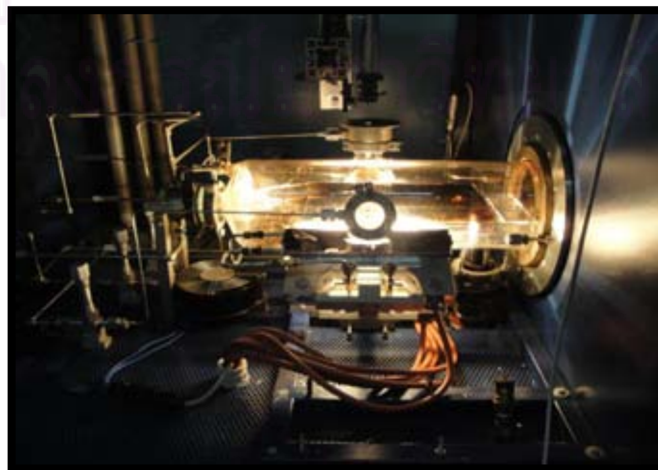

Figure 3.10 Photo of AIXTRON AIX200/4 reactor used in MOVPE system

The lattice mismatch of 3.8% between InP and $In_{0.49}Ga_{0.51}P$ (lattice match to GaAs) drives the strain-induced formation of QDs via Stranski-Krastanow growth mechanism. Schematic representation of the InP QDs structure embedded in InGaP barrier grown on (001) GaAs substrate was depicted in **figure 3.11**. Firstly, 120 nm GaAs buffer layer was grown on semi-insulating GaAs (001) substrate at 610°C. After the growth of GaAs buffer, growth of 150 nm lattice-matched $In_{0.49}Ga_{0.51}P$ layers was followed at the same temperature.

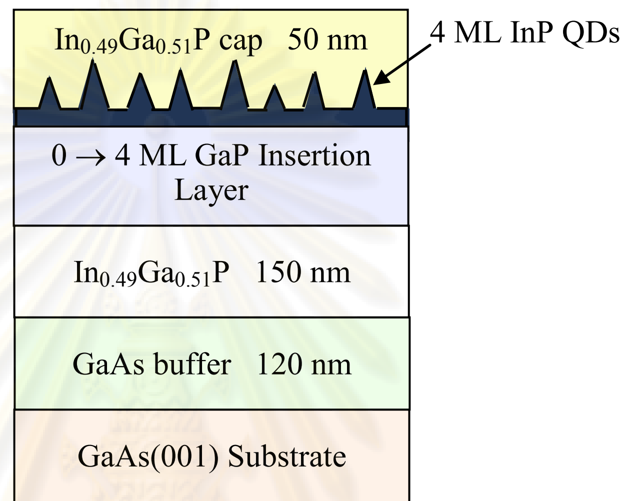

Figure 3.11 Schematic diagram of the vertical layer structure of InP QDs embedded in InGaP barrier grown on (001) GaAs Substrate by changing GaP insertion layers thickness.

In all growth process, the growth temperature was fixed at 610°C. Then 0 - 4 MLs GaP insertion layer was deposited to improve QDs size uniformity. Finally, the single-layer of self-assembled InP QDs was grown at a growth rate of 0.5 ML/s by depositing 4 ML of InP. After the growth of InP QDs, 50 nm cap of InGaP followed in the case of samples planned for PL measurements.

Insertion of GaP layer in the materials system InP/InGaP/GaAs by the Stranski-Krastanow technique in MOVPE technique is less well studied than other material systems. We here review the structural, morphological and optical properties of InP QDs due to insertion of 0 – 4 MLs GaP insertion layer by using atomic force microscopy (AFM) and photoluminescence (PL) measurements. The structural and

optical results of these GaP insertion layers growth samples will be explained in the next chapter.

Regards on the results of InP QDs by changing the thickness of GaP insertion layers, the dots size of InP QDs is quite large at these growth conditions. The InP QDs grown by changing the other growth parameters like temperature, growth rate and III/V ratio at the same growth structure were fabricated and observed to improve the size and density of QDs. Unfortunately, the QDs growth process with these parameter changes could not give good results and quality InP QDs. In the next growth structure, another approach to improve InP QDs properties by insertion of $In_{0.4}Ga_{0.6}P$ layer will be proposed.

For the reason of the comparison of the above GaP insertion layer thickness changes growth structures, the insertion of $In_{0.4}Ga_{0.6}P$ insertion layer at 2 and 4 ML thickness samples were grown at the same growth parameters and conditions. The schematic representation diagram of the vertical layer structure of InP QDs embedded in InGaP barrier grown on (001) GaAs substrate by changing InGaP insertion layers thickness is shown in **figure 3.12**. Comparison of the effect of GaP and InGaP insertion layer by analyzing the structural properties like InP QDs size, shape and density from AFM measurement and also by analyzing the optical properties from PL measurements was observed. The improvement of these results will be discussed in chapter 4.

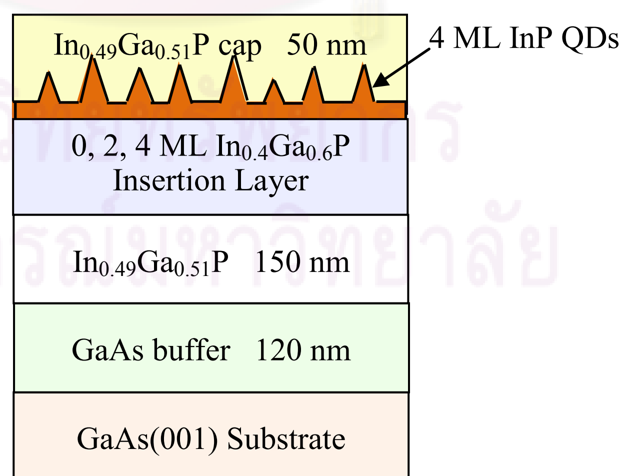

Figure 3.12 Schematic diagram of the vertical layer structure of InP QDs embedded in InGaP barrier grown on (001) GaAs Substrate by changing InGaP insertion layers thickness.

In the next growth structure, 120 nm GaAs buffer layers were grown on semi-insulating GaAs (001) substrates at 610 °C. After the growth of GaAs buffer, growth of 150 nm lattice-matched $In_{0.49}Ga_{0.51}P$ layers was followed at the same temperature. In all growth process, the growth temperature was fixed at 610 °C. Then 0 - 4 MLs $In_{0.4}Ga_{0.6}P$ insertion layer was deposited to improve QDs size uniformity. Then, 2 ML GaP layer was grown to get better QDs quality. Finally, the single-layer of 4 ML self-assembled InP QDs was grown at a growth rate of 0.5 ML/s. After the growth of InP QDs, 50 nm cap of InGaP followed in the case of samples planned for PL measurements. The structural, morphological and optical properties of InP QDs due to insertion of 0 – 4 MLs $In_{0.4}Ga_{0.6}P$ insertion layers by using atomic force microscopy (AFM) and photoluminescence (PL) were characterized. The analysis of these AFM and PL results of InP QDs samples with $In_{0.4}Ga_{0.6}P$ insertion layers will be reported in chapter 4. The schematic representation diagram of vertical layer structure of InP QDs grown on (001) GaAs substrate by insertion of InGaP layer is shown in **figure 3.13**.

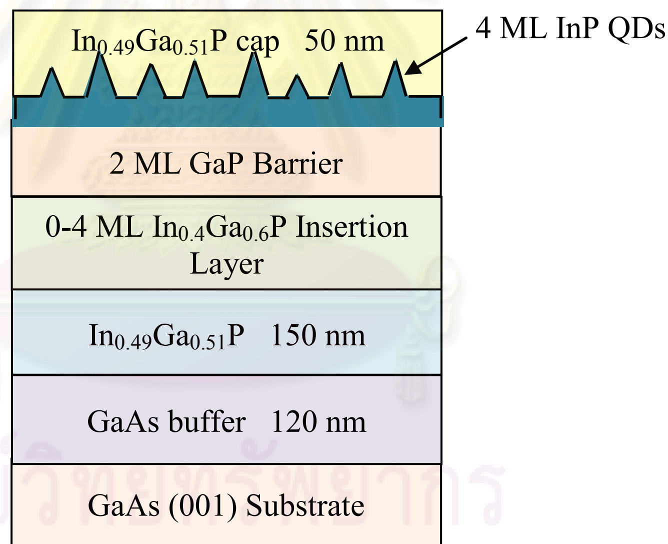

Figure 3.13 Schematic diagram of the vertical layer structure of InP QDs grown on (001) GaAs substrate by insertion of InGaP layer

3.2.2.1 Metal-organic precursors

The metalorganics contain metal-alchilic group bonds and are featured by relatively high vapour pressures, around 100 torr at the working temperatures. The metal-organic sources are highly reactive with Oxygen and water, the more utilized are the thrimethyls, because of their high stability **[84]**.

Depending on the group of the metallic element, different chemical properties are present. The group II precursors are MR_2 kind molecules, as Dimethylzinc or Dimethylcadmium. The group II element has 2 electrons in the s type orbital, in the external shell: to provide two covalent bonds, an sp hybridization occurs, that forms two sp linear orbitals. The so built molecules are electron acceptors, or Lewis acids, thanks to the not completed p orbitals. In the case of the group III precursors, a sp^2 type hybridization takes place (example in **figure 3.14**), with the formation of a trigonal planar molecule, characterized by 3 ligands, separated by 120°. Thus after the formation of 3 covalent bonds, the p orbital, perpendicular to the molecule plane, remains unoccupied, making MO thermostated liquid the molecule electrophile, a Lewis acid also in this case. Differently in case of group V metalorganics, where 3 p and 2 s electrons are present, the formation of 3 covalent bonds and a sp^3, hybridization occurs with tetragonal configuration. They form bond angles around 109, 5° with 2 unbound electrons at disposal. The present electron pair makes the molecule a Lewis basis or electron donor.

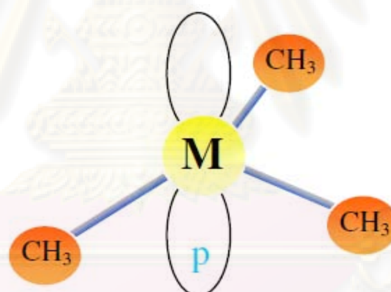

Figure 3.14 $M\text{-}(CH_3)_3$ structure (TMIn and TMGa).

The VI group precursors have 2 s and 4 p electrons. Two covalent bonds occupy two of the tetrahedral sp^3 positions.

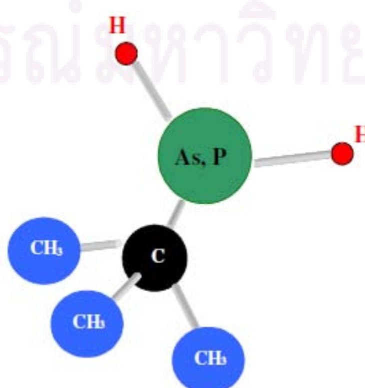

Figure 3.15 MH_2 $C(CH_3)_3$ structure (TBA and TBP)

In general, the metalorganic precursors must have specific properties in the way to be particularly suitable for the growth: a low pyrolysis temperature, the absence of pre-reactions in the gas phase, a high purity (electronic grade) and low toxicity. TBAs (tertiarybutylarsine) and TBP (tertiarybutylphosphine), satisfy quite well these features, mainly the low toxicity and the reduced dissociation temperature **[85]**. Their composition is illustrated in **figure 3.15**. They present very suitable features for the MOVPE process.

First, they are characterized by proper vapour pressures: TBP shows a high vapour pressure, 286 torr at room temperature, while the TBAs is of 96 torr at 10°C. With respect to the more traditional Arsine and Phosphine, one of the Metal-hydrogen bonds is replaced by a metal-carbon bond, sensibly reducing the toxicity. Indeed the limit threshold values (TLV, toxic index defined as the maximum acceptable concentration in a 8 hours/daily use), for AsH_3 and PH_3 are respectively 0.05 and 0.03 ppm, while the LC50 (lethal concentration for 50% of the rats population tested) is between 11 and 50 ppm for AsH_3, 77 for TBAs and 1100 ppm for TBP.

Moreover while AsH_3 undergoes a 50% pyrolysis at a temperature around 600°C, and PH_3 shows pyrolysis temperatures even higher (over 850°C), TBA has a pyrolysis of 50% at 425°C (450°C for TBP). These characteristics grant the lower materials consumption and lower V/III ratios, whose typical values are between 1 and 100, to be compared with the 1000 of the hydrides. The use of these alternative precursors evidenced the experimental reduction of the unintentional Carbon incorporations, and with this, of the background doping **[86]**. This effect, widely documented in the case of TBAs, is naturally consequence of the lower pyrolysis temperatures. This dissociation mechanism causes intra-molecular reactions that end to produce H_2 species in higher quantities than in the case of hydrides. H_2 plays a role in removing radical species from the surfaces.

The hydrogen atmosphere that the ethylic and tetiarybuthilic species tend to form products such as C_2H_4 and C_4H_8, much more stable than CH_2, and much less responsible of Carbon incorporation into the grown layer. Another important vantage is that by lowering the reagents a lower usury of the vacuum system and of the drainage gas synthesis follow. For the growth of doped layers, in the case of III-V InGaAsP-type semiconductors, Zinc for p doping and Silicon for n doping are used.

The most common zinc precursors is Dimethilzinc, DMZn, that undergoes the 50% of the pyrolysis at a temperature of only 250°C. Silicon in general is supplied by a gas source, Disilane.

3.2.2.2 Growth Calibration

Quantum dots formation is heavily affected by growth rate. QDs grown by Stranski-Krastanow islanding mechanism are best understood as a kinetic process of nucleation and growth, unlike the steady-state process that describes growth of thicker layers. QDs kinetics are extremely sensitive to the number of atoms arriving at the surface, the growth rate. The growth rate for bulk materials, and even quantum wells, is most commonly define as the time-averaged process of monolayer-by-monolayer deposition. However, due to their relative thickness, it is commonly ignored that there are in fact two separate domains of materials growth. The first domain is the initial domain where the atomic species first begin to impinge upon the crystalline surface.

Upon close inspection, these surfaces are not simply flat crystal plane like those found within the bulk substrate rather the surfaces are quite different from their buried counterparts. Particularly at higher growth temperatures, a crystalline surface is an evolving and dynamic surface of terraces and steps. Furthermore, the dangling bonds at the surface undergo reorganization to minimize the surface energy. The surface reconstructions have different geometries, as many as seven, each dependent on the particular stoichiometry at the surface **[87, 88]**.

Under normal growth conditions, the GaAs (100) surface atoms stabilize into a so-called 2×4 reconstruction. Upon the initiation of growth, these surface atoms must undergo reorganization to their crystallographically appropriate positions to accommodate the newly arriving atomic species. This reorganization is an evolution through different reconstruction geometries and it takes some time before the first monolayer of new material can organize itself. Essentially, a great deal of surface diffusion is required before the crystal can begin to grow in an ordered fashion. Upon opening of shutter, the effusion begins to cool down slightly as atoms escape from the cell, lowering the temperature and flux rate of the cell. As such, the initial growth rate is slightly higher than that the steady-state growth rate of the uncapped effusion cells.

Careful calibration of each cell in the growth chamber – in both growth regimes – is essential for accurate growth deposition. This calibration process occurs by measuring and averaging the RHEED oscillations in both regimes at a number of different cell temperatures. A curve fitting method is then used to predict growth rates at any temperature within the cell operational range. Whenever a major equipment or process change is made, this process is repeated for each group III effusion cell. Even cooling the materials and reheating them can cause the flux rate to change for a particular effusion cell temperature. Before each growth, the flux rate is measured to renormalize the cell.

At the start of each growth, a buffer layer identical to the substrate is grown to prepare the surface for epitaxial growth and to bury impurities and defects before the important film deposition begins. During this time, RHEED oscillations are taken to confirm that the growth rate curve fitting prediction is accurate. QDs growth is unique in that the entirety of it occurs during the initial growth rate regime. Growing the quantum dots at the slower growth rates leads to the red shift in their emission wavelength. Knowing that larger dots emit at longer wavelength, this phenomena is most likely the result of allowing the dots more time to self-assembled and grow to a larger size.

While the quantum mechanisms of QDs dictate at the dots emit at a single wavelength light that is related to the dots size, a wide distribution of sizes will result in a wide distribution of wavelengths. The size distribution is generally counterproductive for QDs for photonic emission applications where a single emission wavelength is highly desirable but a range of size is an unavoidable result of the kinetic process. The inhomogeneous spectrum broadening can be minimized, but not entirely eliminated.

To grow one wafer for device fabrication, some calibration growths are need to determine the growth rate and the gas flow for each material in the device structure. That is, a device structure typically consists of InGaP layers with 2 or more different compositions, and TMGa and TBAs gas flow rates are needed to grow each InGaP layers. Calibration of dopant flows rate are also need to grow doped materials, however, doping specification is not tight for most devices and the system doping characteristics were stable enough over a long time. Therefore, doping calibration was done in every 2-3 months or before growing device structures with critical doping. On

the other hand, it is very critical to control composition and thickness of InGaP layers since those parameters determine device performances; hence calibrations were needed each time to grow one device structure.

For lattice-matched materials, a bulk layer of the material was grown with gas flows based on previous or similar growth data, and its composition and thickness were obtained by methods described later in material characterization section. For lattice-mismatched materials, we have a thickness limit to grow without relaxation by dislocations. We can grow such material thicker than its critical thickness and have it intentionally relaxed, but if the mismatch is around 1%, the grown layer is likely to be partially relaxed even if it is grown over 1μm **[89]**. It will be difficult to find out how much it is relaxed by using simple X-ray diffraction method. Therefore, a MQW structure which consists of the InGaP material to calibrate and InP barrier was grown. The X-ray tells net strain and total thickness of 1 pair InGaP/GaAS, hence, if we know the growth rate of InP, we can obtain growth rate of the InGaP, and by the thickness ratio we can calculate strain in the InGaP layer.

Dr. G. Fish and Dr. P. Abraham wrote a very useful program for calibration. It calculates material composition from measured strain and photoluminescence (PL) data, and vice versa. It also calculates PL wavelength from MQW by specifying material composition and thickness, hence, we can find out composition of the InGaP in above-mentioned calibration MQW. Once the composition of the grown material is found, the program calculates segregation coefficients for Ga/In and As/P.

The meaning of the segregation coefficient is well explained elsewhere **[90]**: it is basically a parameter which correlates solid-phase composition ratio (Ga/In or As/P of grown layer) to gas-phase composition ratio (TMGa/TMIn or TBAs/TBP) determined by gas flow rate and Epison reading. Hence, with the segregation coefficients we can estimate gas flow rate needed to obtain particular solid-phase composition. The calibration is mostly about refining the segregation coefficients.

3.2.2.3 Effect of Growth Temperature

Growth temperature influences the migration and desorption of adatoms. The density and size of QDs strongly depend on these two factors. The growth temperature of

QDs is typically set around 500°C. At higher temperatures, a lower density of larger QDs is obtained because the diffusion length is larger. **Figure 3.16** shows the surface micrograph of typical samples with self-assembled QDs grown at 500, 520 and 590°C. As the temperature is increased from 500 to 520°C, the QD density declines from 2.2×10^{10} to 1.6×10^{10} cm^{-2} and the QD size is slightly increased.

As the temperature increases to 590°C, unlike the typical QDs, the large islands with low density formed because the indium adatoms were very mobile and nucleation occurred rapidly resulting in QD coalescence. However, the larger QDs more easily induce dislocations when the other layers are capped. At temperatures of below than 500°C, the cracking efficiencies begin to drop off significantly and the material quality degradation may also rise. In this thesis, all QDs were grown at 580 and 610°C.

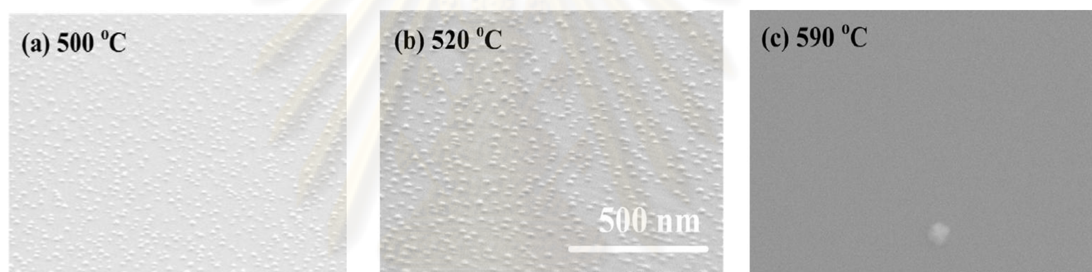

Figure 3.16 Top-view SEM images of $In_{0.5}Ga_{0.5}As$ /GaAs QDs grown at various growth temperatures: (a) 500 °C, (b) 520 °C and (c) 590 °C

3.2.3 Comparison of MBE and MOVPE

In general, devices that are produced by MBE and MOVPE systems have very similar performance characteristics. The major advantages of MOVPE over MBE are their versatility and the suitability for large-scale production. Metal organic chemical vapor deposition is also the most economic technique, particularly for the mass production of devices. Therefore, efforts in the research, development and production of MOVPE have increased rapidly over the last two decades.

The term MOVPE (Metal-organic Vapour Phase Epitaxy) indicates a vapour phase epitaxial deposition which is based on the use of metal-organic precursors (combined in some cases with other types of precursors like hydrides, PH_3 for Phosphorus and

AsH_3, for Arsenic). More general speaking, MOVPE belongs to CVD (chemical vapour deposition) or MOCVD (metalorganic chemical vapour deposition) techniques which not imply an epitaxial growth. The MOVPE technology, developed during the 70ies of 1900, immediately revealed suitable to the growth of a wide range of III-V, II-VI, IV-VI compound semiconductors.

Until nowadays, many types of commercial MOCVD equipment for different purposes have been developed to grow high-quality materials and further fabricate optoelectronic devices. It is also increasingly used in industrial and commercial production, for device applications. MOVPE technology competes with alternative epitaxial growth technique (MBE, molecular beam epitaxy) particularly for large scale producing, in terms of cost savings, higher speed growth, deposition on large areas and adaptability in several types of materials.

Over the years, high purity materials have been obtained, such as GaAs with mobilities over 100000 cm^2/Vs at low temperature and has been clearly demonstrated how this technique is very suitable for producing electronic devices with net interfaces. The MOVPE deposition process takes place with the passage by a vapour phase to a solid one in a growth chamber in which, under opportune constant pressure and temperature conditions, several chemical reactions occur. The precursors that have been transported into the chamber undergo heterogeneous reactions in the vapour phase and homogeneous reactions with the substrate, realising for example, III and V elements that deposit on the substrate forming the III-V compound.

The used pressures are usually around 10-100 mbar while the temperatures range usually from 500 to 700°C. In MBE, on the other hand, a molecular beam produced under Ultra High vacuum (UHV) conditions is exploited. This beam is supplied from holders (called "Knudsen cells”) in the growth chamber, heated by Joule effect and containing elementary states sources. When the slits of the cells are opened the beam can be formed, then arriving on a heated substrate where the deposition occurs. The presence of ultra high vacuum, in the case of MBE, guarantees the growth of high purity samples with sharp interfaces and makes possible the use of in-situ (during growth) analysis techniques like RHEED (Reflection High Energy Electron Diffraction). The advantage of having a rapid source control, since the shutter can be opened and closed in terms of tenths of a second, allows a high compositional control

and good interfaces, guaranteed by a lower temperature growth than in the case of MOVPE, usually around 450-650 ° C, or even lower.

On the other hand, the maintenance of an UHV system in terms of costs is one of the biggest disadvantages of this technique compared with MOVPE and the deposition is normally possible only on limited areas, only recently feasible up to 8 inches, limiting the possible use on an industrial scale. Another disadvantage of MBE is faced in the case of phosphides growth, due to the strong Phosphorous memory effect connected to the difficulty of cleaning a contaminated MBE chamber. In **table 3.2**, drawbacks and vantages of both the techniques are summarized.

Table 3.2: Comparison between MBE and MOVPE.

Growth Techniques	Advantages	Disadvantages
MBE	- High purity - Defined interfaces - In situ monitoring (RHEED)	- Small areas deposition - UHV necessary - High costs - Memory effect for P species
MOVPE	- Not necessary UHV - Possibility of large scale deposition - In-situ monitoring (RAS) - C-self doping	- Toxic sources - Several growth parameters to control - C contamination

Previously, we used MBE for the growth of InP/GaAs material system. Due to the beam-like nature of material transport from injector to substrate at low-pressure (10^{-7} torr) and low temperature (450 °C), fast switching between precursors is enabled. This allows for the epitaxial growth of very thin layers with automatically sharp interfaces. Furthermore, MBE-growth layers are in general uniform, since growth uniformity is not affected by complex gas flow patterns across the substrate. In principle, the thickness of the growth layer can be controlled with monolayer accuracy. The low growth pressure in MBE also enables in-situ growth monitoring, using for example Reflective High Energy Electron Diffraction (RHEED). Compared to MBE, MOVPE is better-established technology and widely used in industrial mass production systems. In my experiment, both MBE and MOVPE are used to growth InP QDs.

3.3 Atomic Force Microscopy (AFM)

The atomic force microscope (AFM) is a very high-resolution type of scanning probe microscope, with demonstrated resolution of fractions of a nanometer. The Atomic Force Microscope is able to measure small variations in surface topography by measuring the detection of a tip (probe) on the end of a cantilever beam, as the sample surface is scanned below the tip. In the microscope, a laser is focused on to the tip of a highly reactive cantilever beam such that the laser is reacted onto the surface of a position sensitive photodetector.

The cantilever is typically silicon or silicon nitride with a tip radius of curvature in the order of nanometers. When the tip is brought into proximity of a sample surface, forces between the tip and the sample lead to a deflection of the cantilever. The sample is scanned underneath the tip via a piezoelectric scanner. Typically, the deflection is measured using a laser spot reflected from the top of cantilever into an array of photodiodes.

The sample is mounted on a piezoelectric tube, which can move the sample in the z direction for maintaining a constant force, and the x and y directions for scanning the sample. A feedback loop is used to maintain either a constant detection (contact mode) or oscillatory amplitude (tapping mode) of the cantilever. In case of the non-contact mode, a feedback loop maintains a constant oscillation amplitude or frequency The mirror is used to increase the path length between the cantilever and the detector in order to amplify detections of the laser beam (**Figure 3.17**) **[91-93]**.

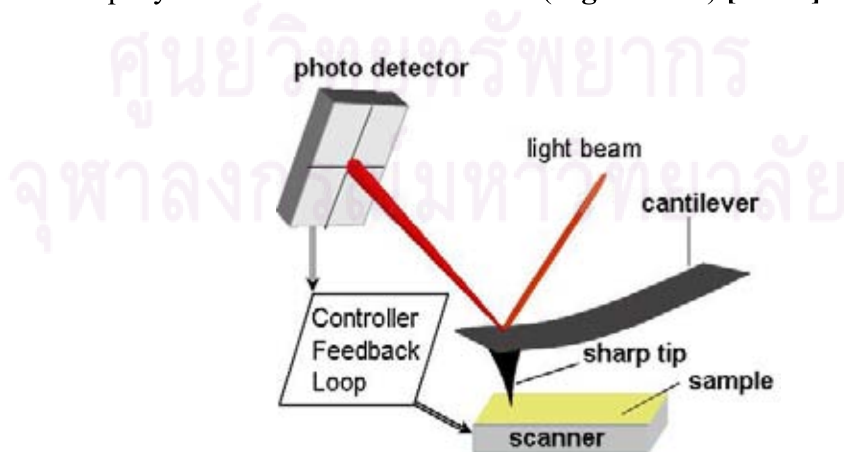

Figure 3.17 A schematic of AFM measurement.

In this work, the AFM images are performed by using SEIKO SPA 400-AFM in tapping mode and Nano-R2^{TM}, Pacific Nanotechnology AFM in close-contact mode. The modes of AFM measurement and photo of AFM tip are shown in **figure 3.18 (a) and (b)**. SEIKO SPA 400-AFM is used to investigate the surface morphology of InP QDs samples growth by MBE and Nano-R2^{TM}, Pacific Nanotechnology AFM is used to investigate the surface morphology of InP QDs samples growth by MOVPE. Photos of AFM system is shown in **figure 3.19** and **3.20**.

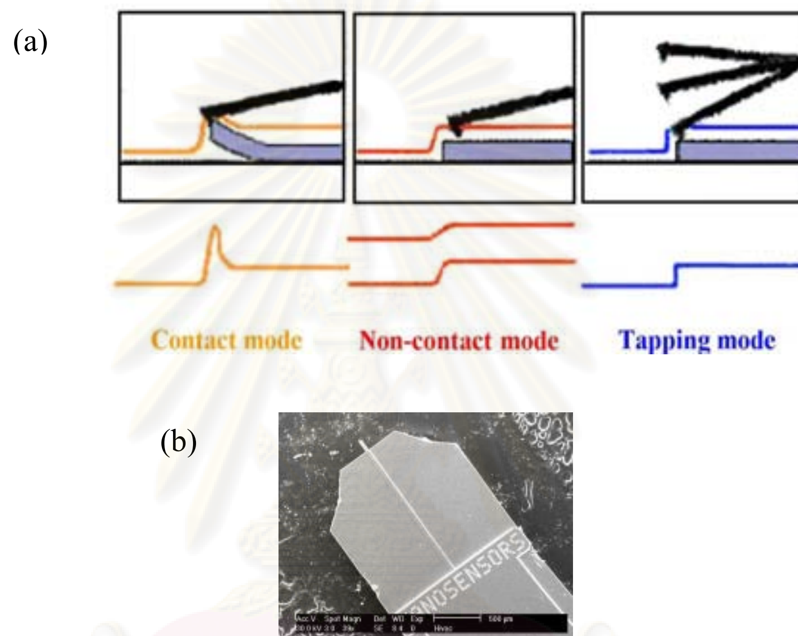

Figure 3.18 (a) Modes of AFM measurement (b) Photo of AFM tip

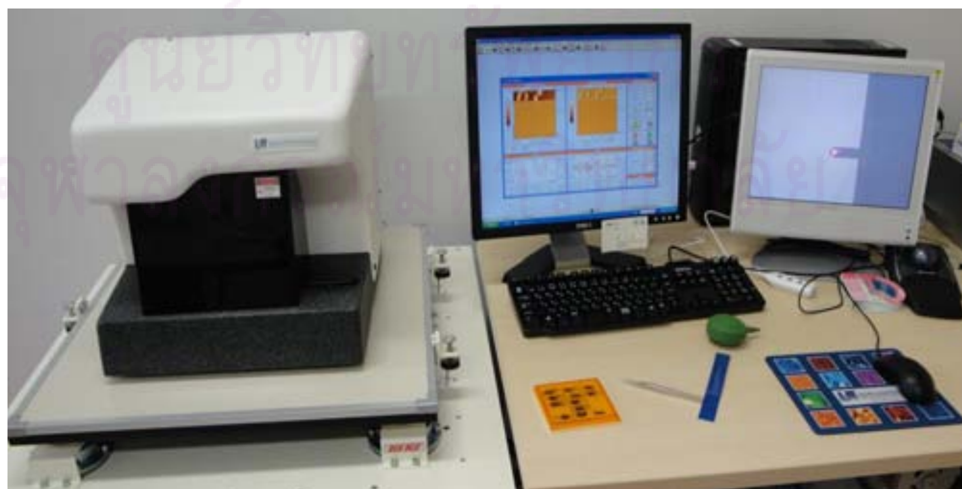

Figure 3.19 Photo of Nano-R2^{TM}, Pacific Nanotechnology AFM Machine

Figure 3.20 Photo of SEIKO SPA 400-AFM Machine

3.4 Photoluminescence (PL)

Although structural information is usually obtained from microscopy data, an important and complementary tool for III–V materials is the photoluminescence (PL) technique. The electronic structure analysed by PL can be used as a probe to detect changes both in the WL and the QD shapes, as well as the effect of surface processes and interface fluctuations on these characteristics.

Photoluminescence (PL) technique is a process in which a sample undergoes an exciting light beam with the energy suitable to generate an excess of free carriers. They recombine producing the emission spectra whose properties are strongly determined by the physical properties of the excited crystal. In the case of semiconductors a radiation with an energy higher than the band gap of the material is used, consequently the optical response can be detected.

The exciting photons generate an excess of holes-electrons pairs and the different generation-recombination processes determine a stationary state or control the decay to the thermodynamic equilibrium. The recombination transitions can be radiative or not-radiative. If the radiative processes involve defects giving rise to levels, which are localized into the forbidden gap, the spectroscopic study of the emitted photons lets to investigate some properties of the related impurities. In fact, the consequence of an interaction with visible or near U.V photons, in the case of semiconductors, originates different possible phenomena **[94]**.

The most common radiative transition, in direct gap semiconductors, is between states in the conduction and valence bands, (interband transitions). If this latter process is clearly associable to a specific feature of the PL spectrum, it lets to estimate the band gap energy, which is particularly useful in case of ternary or quaternary alloys. If shallow impurities are involved in the recombination processes, the radiative recombination of free electrons or holes into the shallow impurity levels give rise to a light emission whose energy and line shape, detected as a function of the temperature, let to investigate their properties. Not radiative transitions are also possible, (phonons-assisted processes): they are typically related to intermediate centres, deeply localized into the forbidden gap and they control the trapping- emission rates (Schokley-Read-Hall regime).

In presence of materials having high purity and excellent structural properties, the band to band recombination processes take place in the PL spectra at sufficient low temperatures, with an excitonic character (narrow and intense emission peak near to the fundamental band edge); so that they are a clear fingerprint of the crystalline quality of the grown epitaxial layers At higher temperature the probability of radiative transitions lowers, the band to band emission peak decreases its intensity and broadens because of the competition with phonon-assisted processes and the thermal broadening effect respectively. On the contrary, lower temperature radiative recombination is favoured. Therefore, at temperatures of few Kelvin degrees, transitions connected to free excitons or bounded impurity excitons are observable.

The most straight information achievable by a PL measurement is, as already discussed, the valuation of the band gap, energy since the band-band transition, in the most cases, is connected to a main emission peak. Since the gap is a function of the alloy composition from the energy of the main estimation peak, the molar fraction of the different elements can be estimated. The photo of room temperature PL setting is shown in **figure 3.21**. Photoluminescence (PL) spectroscopy is also a powerful optical method used for characterizing materials. The PL measurements are particularly useful in the characterizing materials containing quantum dots (QDs) and quantum wells (QWs), and assist in optimization of specific characteristics of InP/GaAs QDs molecules described above PL spectra of InP quantum dots were recorded at room temperature using a diode laser-pumped solid-state laser (532nm).

Figure 3.21 Photo of room temperature photoluminescence setup used for the optical characterization of InP QDs.

The PL signals were collected by an indium gallium arsenide (InGaAs) photo-detector with a built-in preamplifier. A Horiba Jobin Yvon iHR320 imaging spectrometer is used to analyze the wavelength composition of the photoluminescence. The optical design of the iHR320 is depicted in **figure 3.22**. The excitation energy was removed from the measured spectra using long-pass filters following the monochromator (Grating 900 grooves/mm).

In brief, a well-focused beam at the entrance slit is collimated by the collimating mirror. After reflection from the grating attached to the turret, the beam is dispersed such that different wavelength components are spatially separated according to the grating **[95]**. After the grating, the focusing mirror and reflecting mirror then ensure

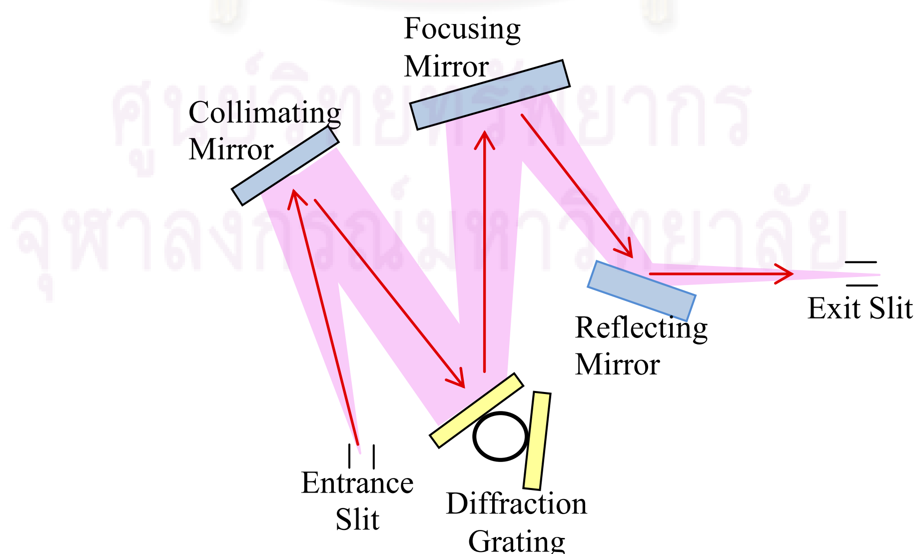

Figure 3.22 Optical design of the iHR320 spectrometer. [Adapted from iHR Fully Automated Imaging Spectrometer User Manual]**[96]**.

ศูนย์วิทยทรัพยากร
จุฬาลงกรณ์มหาวิทยาลัย

that the collimating beam is refocused at the exit slit. An elliptical mirror at the side exit window reflects the beam onto the InGaAs photodetector. For all samples, both the slit width of the emission and excitation are controlled as 5 mm while the integration time was set at 0.5 s. Schematic representation of the room temperature photoluminescence setup used for the optical characterization of InP QDs. The schematic representation of the room temperature photoluminescence setup used for the optical characterization of InP QDs is shown in **figure 3.23**.

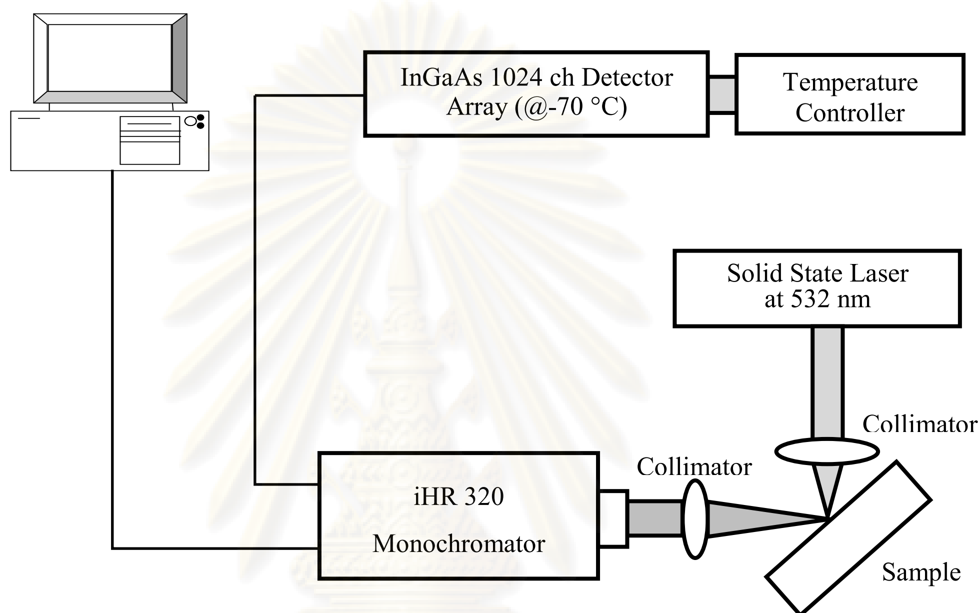

Figure 3.23 Schematic representation of the room temperature photoluminescence setup used for the optical characterization of InP QDs.

From the study of the spectrum at different temperatures, the low-temperature PL measurement was carried out in this work. A photo of PL setup used for low-temperature (20 – 250 K) is shown in **figure 3.24**. The samples were excited by the Ar^{+} laser at wavelength of 427 nm. The laser beam was chopped into pulse signal and focused by focal lens before it is accident on the samples. The dispersed light from the samples is then passed through a monochromator (SPE 1000M) and a detector. The resolved light signal is detected by a liquid-N_2-cooled Ge detector. The intensity of monochromatic light is measured by photomultiplier and signal was amplified and filtered by a lock-in amplifier. The amplified output is subsequently read by a digital multimeter. The sample was mounted on the cold finger of a closed-cycle cryostat. A schematic of the PL measurement system is shown in **figure 3.25**.

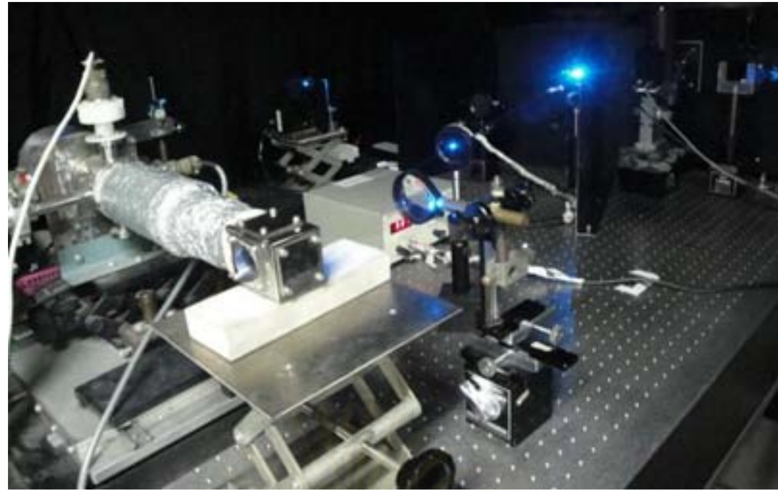

Figure 3.24 Photo of low-temperature photoluminescence setup used for the optical characterization of InP QDs.

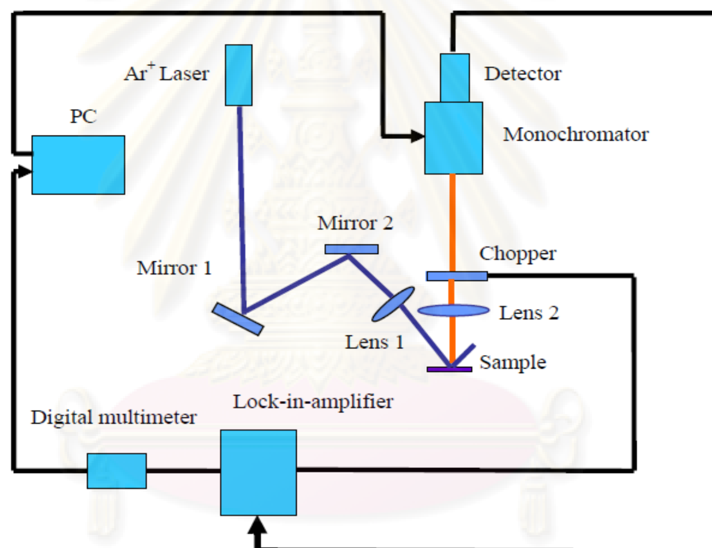

Figure 3.25 Schematic representation of the low-temperature photoluminescence setup used for the optical characterization of InP QDs.

The discussion of this chapter is concerned with growth and characterization techniques to use self-assembling processes in more detail. This description will be an important point of different optimum conditions of the growth parameters for the different deposition techniques and specific materials, significantly affecting the results of the growth experiments. In the following, a more detail discussion about self-assembling the materials combinations InP/ InGaP / GaAs (001) in MBE and MOVPE by analyzing the effect of GaP and InGaP insertion layers. This characterization will be interesting task for future work.

CHAPTER IV

Synthesis and Characterization of InP Nanostructures

4.1 Properties of InP semiconductor compounds

Many so-called compound semiconductors that consist of two or more elements have optical and electrical properties that are absent in silicon, something that has triggered intense research for more expensive materials as well, like for instance, InP and GaAs. These are III-V materials that have direct band gaps, which from an application point of view mean that they are excellent candidates for light emitting devices **[92]**. This discussion will be focus on InP III-V semiconductor compound. InP is a direct band gap semiconductor with a band gap energy of 1.27 eV.

Similar as II-VI semiconductors, InP exhibits quantum size effects and size-dependent optical spectra at the nanometer scale. InP has an electronic velocity higher than Silicon but even than GaAs; for this reason it has possible applications in the high frequency range and power electronic devices **[98]**. It is also characterized by a direct band gap, which encourages its use in optoelectronic devices. It has moreover the highest carriers lifetime among Zinc-blend structures based on III-Vs.

Consequently, phosphorus-containing alloys are widely used for the production of optoelectronic devices. The band gap and lattice parameter can be tuned over a wide range **[99]**. As shown in **table 4.1**, the As and P based semiconductors have also very low effective masses, so that they can present very high electronic mobilities.

In this work, gallium arsenide substates are used to fabricate InP QDs. GaAs (with a lattice parameter of 5.56 Ams and an Energy gap of 1.424 eV at 300K) is an extremely interesting material, thanks to its high mobility, ten times more than Silicon, and its direct energy gap. Moreover, it can be easily grown from the melt, providing relatively cheap wafers, useful for the vapour phase growth. In addition, GaAs based devices can operate at higher power levels than Silicon based ones, allowing applications in mobile telephony, satellite communication, exploiting higher breakdown voltages.

Table 4.1: Some Parameters of P and As based semiconductors compound

Semiconductor	Energy gap (eV) at 300K	Lattice parameter (Å)	Effective mass (m_e/m_0)	Gap's type
Si	1.12	0.54311	0.98	Indirect
Ge	0.66	0.565791 nm	1.64	Indirect
GaAs	1.424	5.65321	0.065	Direct
GaP	2.26	5.45117	0.35	Indirect
GaSb	0.73	6.09593	0.044	Direct
AlSb	1.58	6.1335	0.39	Indirect
AlAs	2.16	5.6622	0.11	Indirect
InP	1.35	5.86875	0.078	Direct
InSb	0.17	6.47937	0.0145	Direct
InAs	0.36	6.0584	0.022	Direct

After this brief overview on indium phosphite semiconductors, we focus particular attention to those materials studied in this PhD work and about which the experimental aspects, features and properties will be treated in the following sections. A particular technological interest regards the InP/GaAs structure, in which an GaP and InGaP layer is deposited on a GaAs substrate. The two semiconductors that form this structure have different properties, which optimally fit for defined applications, like the already mentioned photodetector, laser and solar cells for examples.

4.2 Structural and Optical Properties of Quantum Dots

Structural and optical properties of self-assembled QDs were investigated by using a lot of different methods such as transmission electron microscopy (TEM), high resolution electron microscopy (HREM), scanning tunnelling microscopy (STM), atomic force microscopy (AFM), cathode luminescence (CL), and

photoluminescence (PL). In this work, InP/InGaP/GaAs systems were fabricated by using MBE and MOVPE to characterize the structural and optical properties of InP QDs. This chapter will be provided the review of the activities related to the InP/InGaP/GaAs QDs. The chapter starts with the structural and optical properties of InP QDs before concentrating on the current status of InP QDs by insertion of GaP and InGaP layers.

Although most work concentrates on InAs/GaAs quantum dots, wavelength for the visible range must be obtained with other material systems like InP/InGaP/GaAs **[100]** or InAlAs/AlGaAs **[101]** for the red spectral part or InGaN for even shorter wavelengths**[102,103]**. InP/InGaP/GaAs have been fabricated with different epitaxial techniques such as molecular beam epitaxy (MBE) and metal organic vapor phase epitaxy (MOVPE). Depending on the different fabrication methods, the structural and optical properties of InP QDs have been observed and analyzed.

The controlled seeding method that we report here has potential as a generic means of forming better size, uniformity and optical properties of InP QDs, and may also offer opportunities for applications, such as single-photon detector and laser in optoelectronic devices.

4.2.1 Size, Shape, Homogeneity and Density

Vast research has been done in the field of quantum dot formation. A necessary condition for applications of self-assembling is to have control over densities and sizes of quantum dots. These quantities are not independent from each other. For device applications, requirements of homogeneity and site-control of the dots have been, and are, challenging tasks. Using self-assembling for fabrication of quantum dot structures, one has to accept that the result will always be an ensemble of dots with a certain size distribution. However, there are some rules to reduce this disadvantageous effect to a minimum. Besides finding the optimum for the deposited amount, deposition temperature and deposition rate, one important rule is to use the right timing for the process. Right timing means to initiate the 2D-3D transition in such a way that, in as short as possible a time interval, the necessary density of nucleation sites will be created and the islands can grow.

In other words, the density of dots increases with increasing deposition rate (supersaturation), while it decreases with increasing temperature. Note that the deposited material is distributed over the stable growing nuclei, thus one can expect an increase in size of the dots with decreasing density **[104]**. Another way of affecting the sizes of the dots, which can increase the size homogeneity of the dots, is to insert an interface layer before the deposition of the dot material **[105]**. In this research work, GaP and InGaP interface layers were inserted before the growth of InP QDs. From these significant results, the effect of GaP and InGaP insertion layers will result in good size homogeneities and density of InP structural properties. The detail explanation of these layers effect will be discussed in the next sections.

A common tool for measuring densities and sizes of self-assembled islands is atomic force microscopy. To get further information on the homogeneity of the dots, photoluminescence is often used, the narrower the emission linewidth the better the homogeneity and the more suitable for applications, like lasers for instance. For an overview of the field of quantum dot lasers, Grundmann's review article can be recommended **[106]**. If the quantum dots are ordered in shape, size, and position, the highest degree of ordering will be reached.

4.2.2 Optical Properties

In this section optical properties of InP QDs are discussed. The optical properties of other III-V and II-VI QDs exhibit the same general behavior as InP QDs, and the latter is used to examplify some of the important features of this behavior. In order to study the optical properties, single dots spectroscopy is widely used to eliminate ambiguity originating from nonuniformities in the size, shape, interface and interesting phenomena hidden behind the inhomogeneous distribution have been revealed, such as many carrier effects **[107]**, strong optical anisotropy **[108]**, fluorescence intermittency **[109]**, spectral diffusion and photon anti-bunching **[110]**. The single QDs measurements need to be carried out on several QDs in a sample to understand the general nature of the zero-dimensional systems.

In this work, the optical properties of InP QDs investigated by using the room temperature PL measurement. InP QDs embedded in $In_{0.49}Ga_{0.51}P$ matrix were grown on nominally (001) oriented GaAs substrate. In these structures, the different

thickness of GaP and InGaP layers were inserted to improve InP QDs properties. The PL measurement can be used in the current study to establish the the influence of the GaP and InGaP insertion layers on the optical properties of the InP QDs.

The perfect analog would be InP dots in a GaP matrix. However, due to the indirect character of GaP, this material is less attractive for optoelectronic applications. Therefore, most of the research concentrated on InP dots in a InGaP matrix, a ternary compound which is lattice match to GaAs for nearly equal parts of Ga and In. The larger bandgap of the phosphides opens another interesting part of the spectrum for quantum dots laser diodes: InGaP is the material of choice for high brightness red and yellow light emitting LEDs as well as for red light emitting laser diodes with emission wavelengths around 650 nm. That's kind of optical properties, InP and phosphide alloy quantum dots can be used in many optical device applications.

Characterization of QDs, especially optical properties, was reduced to the quantum confinement effect and the surface effect. PL characterization is important for understanding the optical properties of the QD structures. In addition to photoluminescence (PL) measurements, the images that show the integrated PL intensity are useful for efficient measurements and also help to isolate interesting exceptions. It was found that the InP QDs gave strong photoluminescence, which in fact dominated the spectrum from the samples.

4.3 Effect of Insertion Layers on InP Nanostructures

The shape, size and optical properties of InP QDs can be strongly influenced by the growth parameters. In this work, the InP QDs were grown on lattice matched InGaP on GaAs. Between the InGaP layer and the InP QDs layer 0-4 ML thin GaP and InGaP layers were introduced to improve the properties of InP QDs. The effect of these GaP and InGaP insertion layers on the structural optical properties of InP QDs will be discussed in the following sections.

4.3.1 GaP Insertion Layer

In this section, the brief explanation of GaP insertion layer effect on the properties of InP QDs will be described. GaP has a smaller lattice constant than $In_{0.48}Ga_{0.52}P$ and,

hence, compared to an InP/ $In_{0.48}Ga_{0.52}P$ interface, the InP/GaP interface is higher strained (lattice mismatch of about 7.7%). Consequently, the growth of a thin layer of GaP between $In_{0.48}Ga_{0.52}P$ and InP layers affects the formation of InP QDs. Our observations coincide with the common belief that a higher lattice mismatch favors the Stranski-Krastanow QD formation. From this work, AFM images of samples containing 3 ML InP grown on GaP interface 1-4 ML by MBE; here the area density of QDs is about 10^{10} cm^{-2} and the dots have a maximum base length of 50 nm. (Note that AFM images cannot give exact information on the dots smaller than 30 nm.)

On the other hand, for samples grown in the same way but without GaP interface layer, the maximum base length of the dots 45 nm was observed. Consequently, the improvements of size homogeneity and optical properties of MOVPE InP QDs on and in $In_{0.49}Ga_{0.51}P$ via growth of an inserted GaP layer have been reported. The area density of the InP QDs is about 10^9 cm^{-2} and the dots have a maximum base length of 79 nm. In the same growth conditions, the sample without GaP insertion layer shows less area density and bigger size compare with GaP inserted samples. The maximum base length of the dots without GaP insertion layer was 88 nm was observed.

4.3.2 InGaP Insertion Layer

InP QDs grown on InGaP by insertion of InGaP layer is less well studied than InP QDs grown by insertion of GaP insertion layer. Most research works have been concentrated on the characterization of InP QDs by insertion of GaP layer. We will here review the understanding of the less studied, but equally interesting, system of InP QDs by insertion of single and double InGaP insertion layer by MOVPE. We will briefly touch the effect of InGaP insertion layers on the fabrication aspect and instead concentrate on the physics of InP QDs.

It was found that the InP QDs with InGaP give smaller QDs size and better uniformity compare with GaP insertion layer samples. This is the best improvement of QDs properties. The evolution of the spectra of photoluminescence, generally the intensity of InGaP insertion layer samples is better than GaP insertion layer. As a comparison of double and single InGaP insertion layers, the size of QDs with double InGaP insertion layer is smaller than single layer and also the PL intensity is higher

than single InGaP insertion layer. It should be noted that InGaP insertion layer can improve properties of InP QDs than GaP insertion layer.

4.4 Effect of GaP Insertion Layer on Structural Characterization of $InP/In_{0.48}Ga_{0.52}P/GaAs$ System by MBE

Quantum dots composed of InP within an $In_{0.48}Ga_{0.52}P$ matrix were elaborated by molecular beam epitaxy on semi-insulating (100) oriented GaAs substrates using a Riber 32P system. The lattice mismatch of 3.8% between InP and $In_{0.48}Ga_{0.52}P$ (lattice matched to GaAs) drives the strain-induced the formation of QDs via Stranski-Krastanow growth mechanism. InGaP can be matched to GaAs, when the Indium molar fraction is 48% and Gallium, consequentially, is the 52%, yielding an Energy gap of 1.88 eV (at room temperature). $In_{0.48}Ga_{0.52}P$, has interesting properties like a low electron effective mass, 0.111 m_0, high mobility (1850 cm^2/Vs at room temperature) and a direct band gap [1.11]. It can be mainly used in HEMTs, HCTs, pumping lasers for optical fibre amplifiers, doped with Erbium [1.12], but also for tandem cells in space applications and in combination with Al (AlGaInP) for high efficiency LEDs (emitting in green, yellow, orange and orange-red colours light). In this InP QDs structure, other growth parameters are kept the same and only change the thickness of GaP layer. The GaP insertion layer was inserted before the growth of InP QDs and the effect of this insertion layer was observed in this section.

Figures 4.1 (a)-(e) show AFM images of InP quantum dots grown without and with 1-4 ML GaP. AFM images of five samples grown at the same growth condition and the same InP coverage of 3 MLs at about 450°C growth observed for all samples with the changes of the thickness of GaP insertion layer.

We note the AFM images of 500×500 nm^2 area that size (diameter), height, uniformity and density of InP QDs. The study of quantum dot formation and distribution of their size and height for different thickness reveals that average height and diameter of smaller (bigger) QDs are 1 nm (6 nm) and 37 nm (56 nm), respectively. Both size and height are increased while increasing the thickness of GaP insertion layer. The surface morphology of InP is also revealed that the insertion of GaP improves the uniformity when the GaP thickness is over 3 ML. The density of

all the QDs (smaller and bigger) is in the range of 2-5×10^{10} cm^{-2} **[111]**. The density of coalesced InP QDs decreases with the increase of thickness of GaP insertion layers. InP QD on $In_{0.48}Ga_{0.52}P$ is the highest density of about 4.8×10^{10} cm^{-2}.

In order to investigate the role of GaP contamination layer, we perform the characterization of size and height by AFM. **Figure 4.1** shows the size (diameter) distribution histogram of the quantum dots with a various thickness of GaP insertion layer. The lateral size of these structures is increased while increasing the GaP layer thickness. For comparison, the average diameter of the sample with 3 ML GaP insertion layer is larger than the other samples at about 52 nm. For sample without GaP layer, the largest dot diameter is about 42 nm and QDs uniformity is good at that condition. The sample with 1 ML GaP layer, the average dots size increases to 45 nm and dots uniformity is declined. For samples with GaP insertion layers thickness of 2 to 4 ML, the average dots size also increases to 45, 49, and 48 nm, respectively and dots uniformity is declined.

However the increasing GaP insertion layer thickness, the size of the quantum dot is increased and the uniformity is reduced as shown the regularity of their distributions in **figure 4.1**. The sample of 4 ML GaP insertion layer, the QDs size is not clearly different from the sample of 3 ML GaP layer. Although this may be due to thicker insertion layer, it is likely that most of the extra material comes from the exposed GaP surface through In/Ga exchange which may be further enhanced by strain as As/P exchange **[112]**.

In addition to the indium segregation, the In/Ga exchange reaction affects the energy to decrease the total system energy and form excess InP QDs nucleation on GaP layer. The exchange reaction occurs at the places through the thin GaP insertion layer which are covered by the dots. The free InP recombining with P atoms. This leads to bigger QDs as noted in the AFM images. **Figure 4.2** shows height histograms of InP QDs that extracted from 500×500 nm^2 AFM images. The average height of all samples was nearly the same. A comparison of samples with 0 and 1 MLs of GaP insertion layer, they are the same average height at about 4 nm. The heights of 2, 3 and 4 MLs GaP insertion layer samples are slightly decreased. When the thicker GaP insertion layer is grown between QDs and $In_{0.48}Ga_{0.52}P$ layer, the height of InP QDs

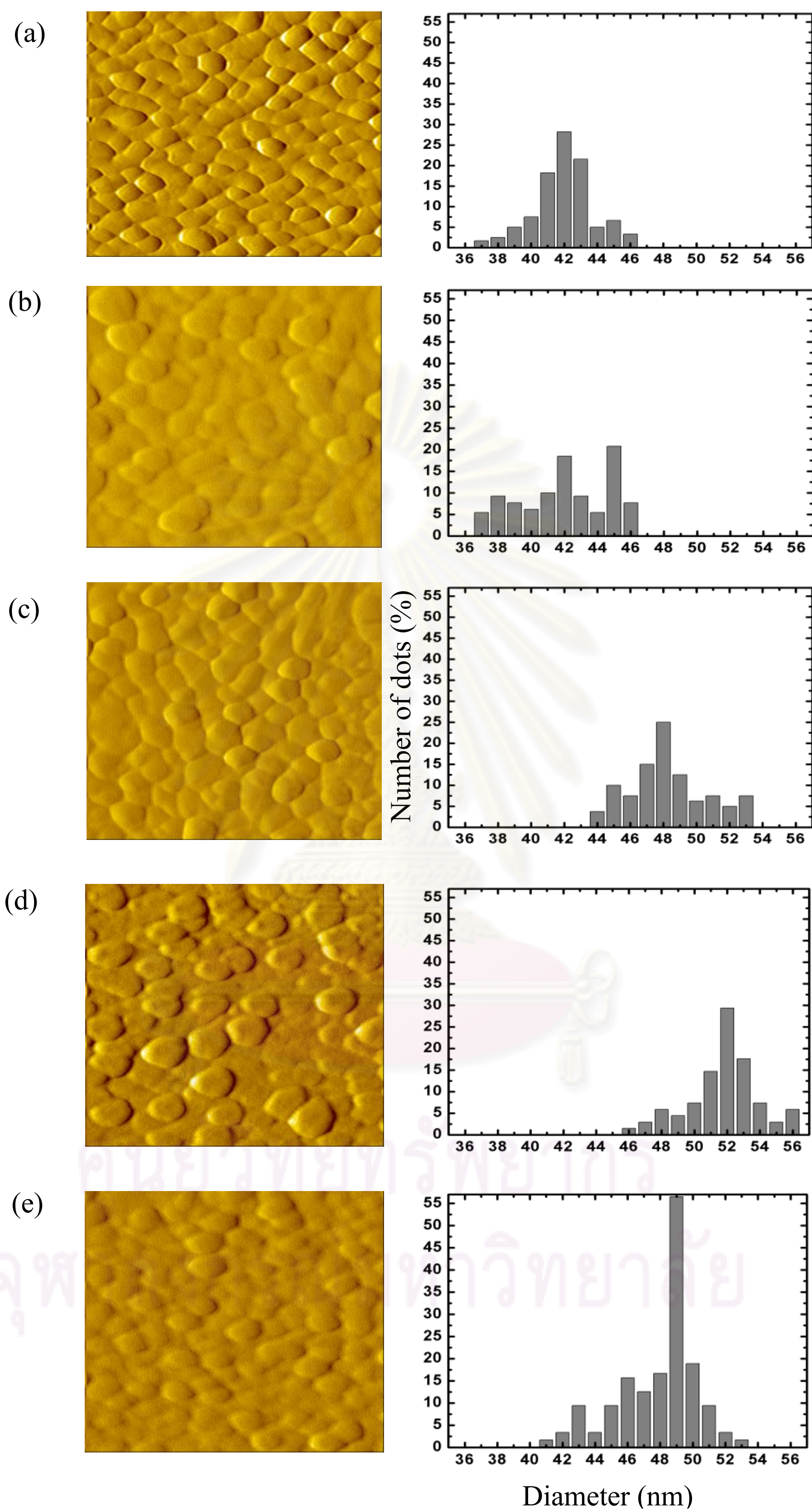

Figure 4.1 Typical AFM images of InP QDs with diameter distribution histogram graph grown on (a) 0 ML (b) 1 ML (c) 2 ML (d) 3 ML (e) 4 ML GaP layers

ศูนย์วิทยทรัพยากร
จุฬาลงกรณ์มหาวิทยาลัย

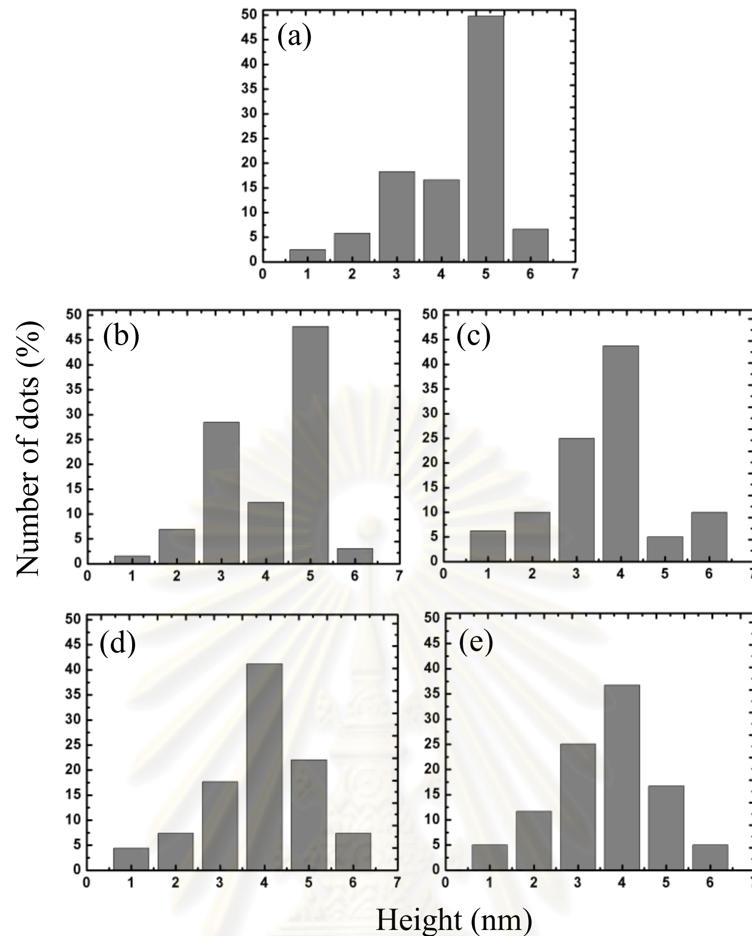

Figure 4.2 Height distribution histograms of InP QDs grown on (a) 0 ML (b) 1 ML (c) 2 ML (d) 3 ML and (e) 4 ML GaP layers

increase and the dots become less uniform in terms of size and composition distribution due to suppression of the exchange reaction as noted in the AFM images.

The sample without GaP insertion layer showed a significantly improved size, height dispersion and homogeneity. According to the similar effect of QDs diameter, the segregated indium atom may react with P bond during the growth of InP QDs and forms additional InP which increased the QD height and its non-uniformity. Furthermore, the size and height fluctuation was minimal under the effect of strain compensation layer.

Another important parameter in the growth of semiconductor III-V quantum dots is the dots density. The dot density decreases approximately from 4.8×10^{10} cm^{-2} to 2.7×10^{10} cm^{-2} due to the insertion of 0-4 ML GaP layers. Figure 4.3 shows the relation of dot density of InP QDs as a function of the GaP insertion layer thickness.

It is observed that with increasing GaP thickness, the QDs density decreases and the height and diameter increase [**113]** as shown in **figure 4.3**. This is also an expected result and is due to a decreased supersaturation at the onset of nucleation which leads to a lower nucleation density. Since the QDs growth conditions are the same, the bigger QD height and diameter and reduced density for the sample grown directly on $In_{0.48}Ga_{0.52}P$ interlayer indicates that the insertion of the 0-4 MLs GaP layer results in more incorporation of the material. The incorporation efficiency of In during the deposition of an GaP layer reduces as strain increases **[113]**. The further conclusion is that the density of 3 ML InP QDs depends on GaP thickness because the diffusion length of In atoms on GaP layer is shorten when increasing these parameters [**114**].

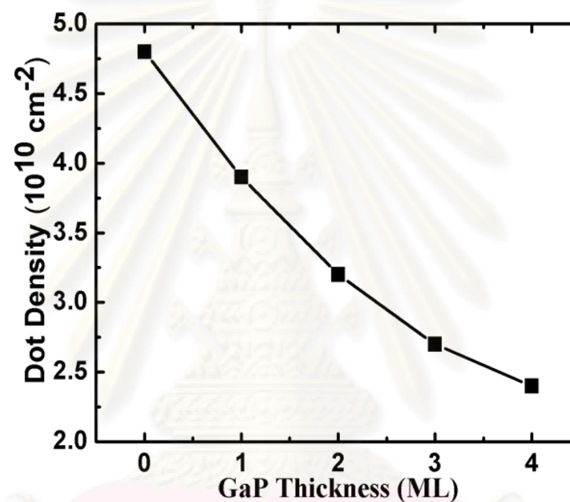

Figure 4.3 InP QDs density plotted as a function of 0-4 ML GaP thickness.

4.5 InP/$In_{0.49}Ga_{0.51}$P/GaAs System by MOVPE

QDs composed of InP embedded in $In_{0.49}Ga_{0.51}P$ matrix were carried out in a horizontal MOVPE reactor _AIXTRON, AIX200/4 with a rotating substrate holder on nominally (001) oriented GaAs substrate. MOVPE grown islands are larger and exhibit an anisotropic shape. The shape and size can be strongly influenced by the growth parameters. Lattice-matched $In_{0.49}Ga_{0.51}P$/GaAs structures are becoming major III-V semiconductor systems because, compared to AlGaAs/GaAs systems, they have lower reactivity with oxygen, and more reduced DX centers and lower interfacial recombination rates. Fabrication of InP SAQDs in InGaP/GaAs systems is difficult by metal organic vapor phase epitaxy (MOVPE), mainly due to the exchange between As and P. The other causes that contribute to the difficulty include the ordering effect of InGaP and the segregation of In in the InGaP layer. The lattice

mismatch of 3.8% between InP and $In_{0.49}Ga_{0.51}P$ (lattice match to GaAs) drives the strain-induced formation of QDs via Stranski-Krastanow growth mechanism. The GaP and InGaP layers are inserted in the above InP/InGaP/GaAs system and the influence of these layers on InP QDs will be discussed in the following sections.

4.5.1 Effect of GaP Insertion Layer

Insertion of GaP layer in the materials system InP/InGaP/GaAs by the Stranski-Krastanow technique in MOVPE technique is less well studied than other material systems. We here review the structural, morphological and optical properties of InP QDs due to insertion of 0 – 4 MLs GaP insertion layer by using atomic force microscopy (AFM) and photoluminescence (PL) measurements. The AFM measurements were performed by using a Nanoscope in close-contact mode. PL measurement was carried out using the 532 nm line of solid state laser. The PL signal was collected by an InGaAs photo-detector with a built-in preamplifier.

4.5.1.1 Structural Characterization

In order to investigate the role of GaP insertion layer on the characterization of size and density of InP SAQDs, we performed the measurement of AFM. **Figures 4.4 (a), (b), (c), (d) and (e)** show 1×1 μm^2 area AFM images of InP quantum dots grown with 0 - 4 ML GaP insertion layer. The study of nanostructure formation and distribution of their size and height for insertion of GaP layer thickness reveals that average height and diameter of smaller (bigger) QDs are 13 nm (28 nm) and 66 nm (87 nm), respectively. The average height and diameter of InP QDs without GaP IL are 25 nm and 85 nm. Both size and height are generally decrease by increasing the thickness of GaP insertion layer. The sample with 2 ML GaP insertion layer showed a significantly improved size, height dispersion and homogeneity. The dot density increases from 2.3×10^9 cm^{-2} to 4.2×10^9 cm^{-2} due to insertion of 0 ML - 2 ML GaP layers and then decrease again to 3.3×10^9 cm^{-2} due to inseriton of 3 ML- 4 ML GaP layer.

The maximum density in 4.2×10^9 cm^{-2} and smallest uniform InP QDs were obtained with 2 ML thickness of a GaP insertion layer. After insertion of the 2 ML GaP layer

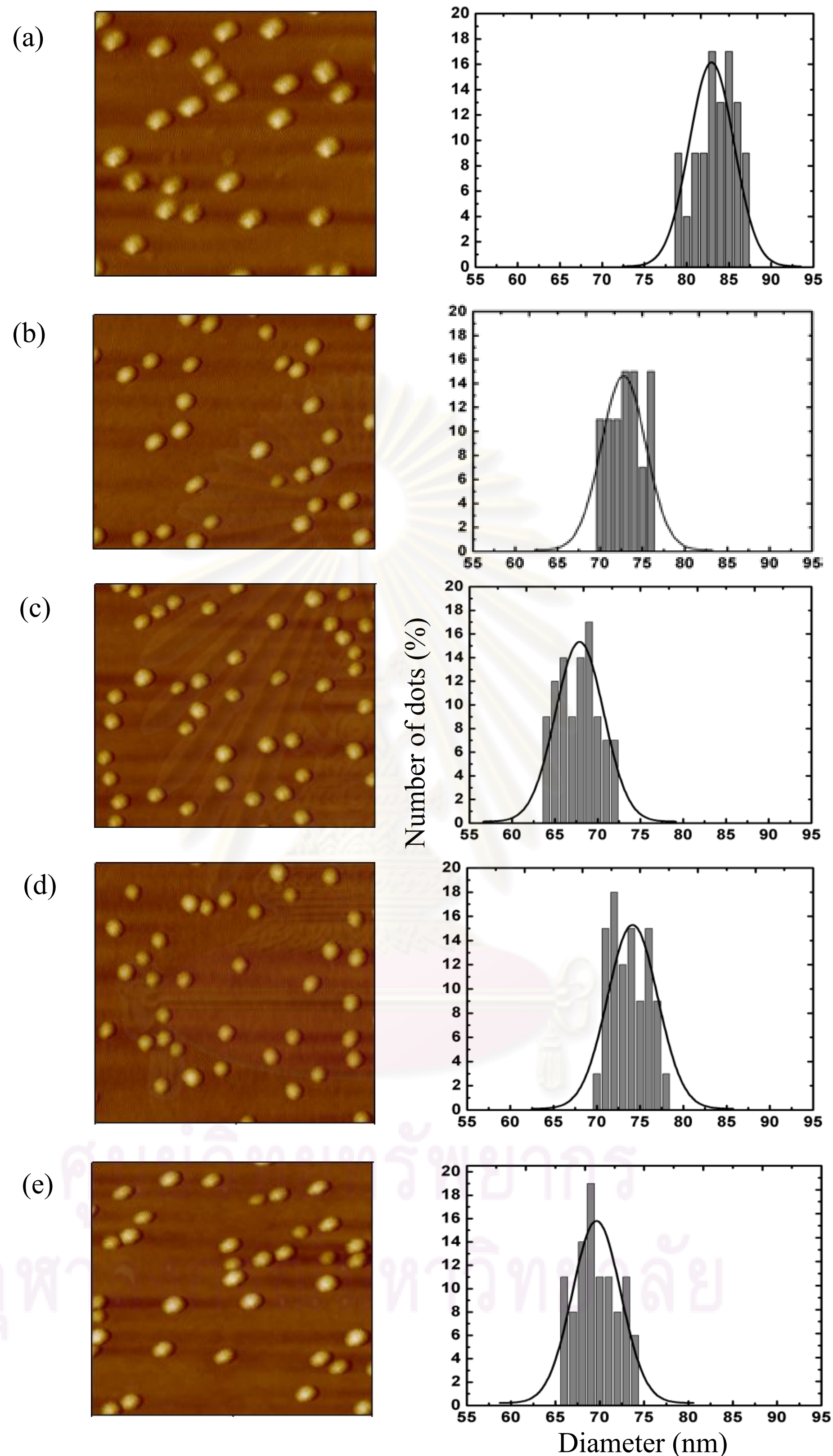

Figure 4.4 Typical (1μm × 1μm) scan range AFM images of InP QDs embedded in InGaP barrier with (a) 0 ML (b) 1 ML (c) 2 ML (d) 3 ML (e) 4 ML GaP layers.

thickness, the QDs size was quite increase and density was decrease again. This observation indicated that QDs density first increased with increasing of GaP insertion layer thickness and then it saturated at 2 ML GaP insertion layer thickness. Such behavior showed the nuclei centers first increased with the increase of GaP insertion layer thickness from 0 ML to 2 ML, afterwards nucleation was completed and further increased in the thickness did not significantly increase the density of QDs. It is likely that the incorporation efficiency of In during the deposition of GaP layer reduces as the strain increases.

Figure 4.5 shows height histograms of InP QDs that were extracted from 1μm × 1μm AFM images. It was found that heights are decrease and homogeneity were generally increase by increasing the thickness of GaP insertion layer. The sample with 2 ML

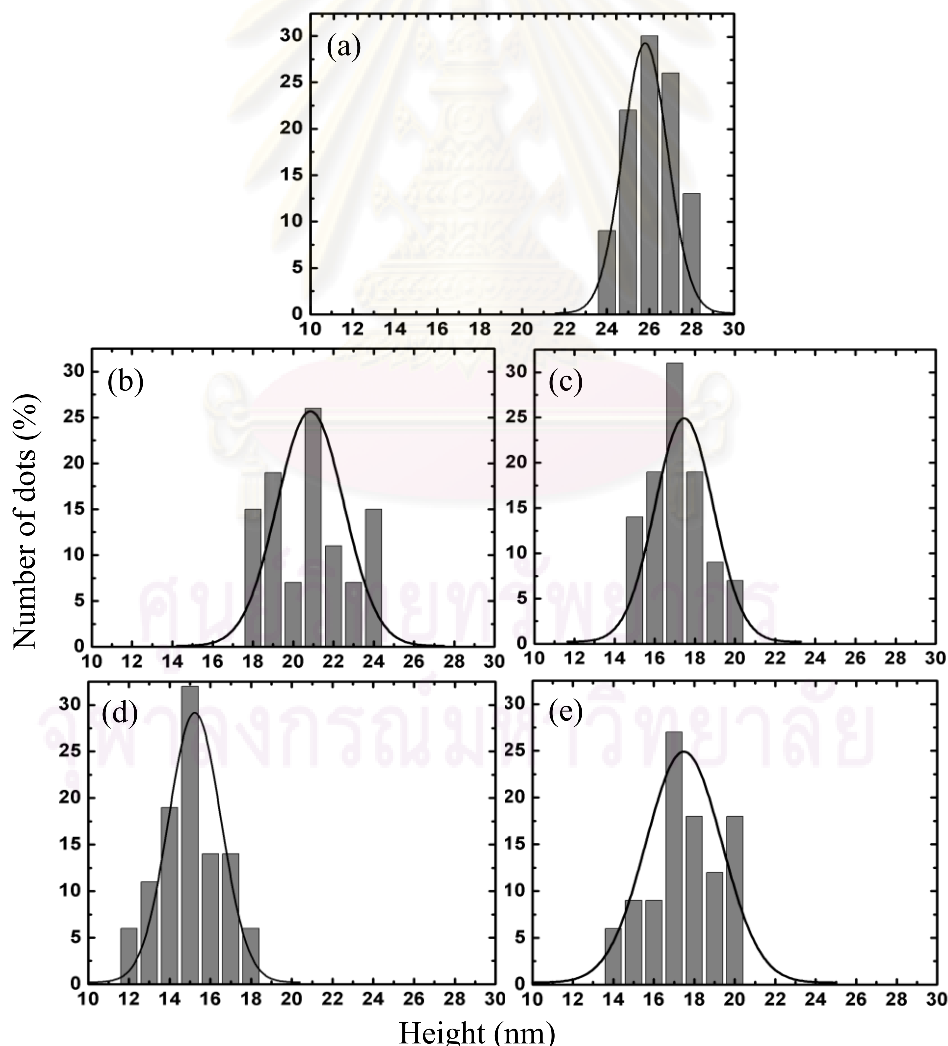

Figure 4.5 Height distribution histograms of InP QDs on (a) 0 ML (b) 1 ML (c) 2 ML (d) 3 ML and (e) 4 ML GaP insertion layers

GaP insertion layer showed a significantly improved size, height dispersion and homogeneity. The maximum density in 4.2×10^{9} cm^{-2} and smallest uniform InP QDs were obtained with 2 ML thickness of GaP insertion layer. After insertion of 2 ML GaP layer thickness, the QDs size was quite increase again. This observation indicated that QDs height first increased with increasing of GaP insertion layer thickness and then it saturated at 2 ML GaP insertion layer thickness. Such behavior showed that the nuclei centers first increased with the increase of GaP insertion layer thickness from 0 ML to 2 ML, afterwards nucleation was complete and further increase in the thickness did not significantly increase the height of QDs. However, it could also be seen that GaP insertion layer caused a reduction in the QDs size fluctuation.

Another important parameter in the growth of semiconductor III-V quantum dots is the dots density. **Figure 4.6** summarizes the changes in the QDs density and QDs mean height with the GaP insertion layer thickness. Since the growth conditions were the same in all cases, decrease in QDs height, diameter and increase in density with GaP insertion layer indicates that the insertion of thin GaP layer resulted in more material deposition. The dot density increases from 2.3×10^{9} cm^{-2} to 4.2×10^{9} cm^{-2} due to the insertion of 0 ML - 2 ML GaP layers and then decrease again to 3.3×10^{9} cm^{-2} due to insertion of 3 ML- 4 ML GaP layer. The improvement of GaP insertion layer effect on InP QDs can be seen at 2 ML GaP layer thickness.

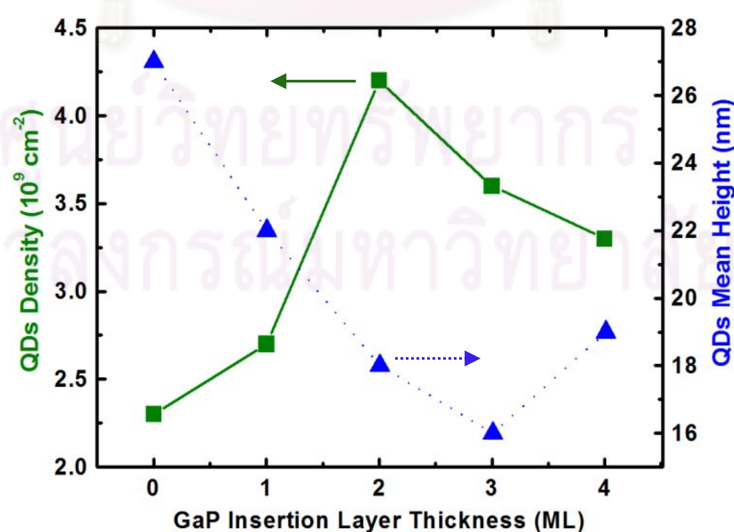

Figure 4.6 Effect of GaP insertion layer on QDs average size and density for InP SAQDs embedded in InGaP grown at 610 °C.

4.5.1.2 Optical Characterization

Optical characterization of InP/InGaP/GaAs structures containing different GaP insertion layer thickness of InP embedded in InGaP (lattice matched to GaAs) and grown at 610°C by low-pressure MOVPE was discussed. Regarding the growth technique, realization of wavelength tunable InP/GaAs QDs by MOVPE is highly desirable, which is the most common growth technique for InP based photonic devices.

The evolution of the photoluminescence (PL) spectra of InP QDs as a function of the thickness of the GaP insertion layer is shown in **figure 4.7**. These samples above were grown continuously, i.e., there was no growth interruption after InP deposition. It was found that the InP QDs gave strong photoluminescence (PL), which in fact dominated the spectrum from the samples. These experiments illustrate that 3D islands develop at 610°C within a time span of only a few seconds. This happens obviously by reorganization of material deposited primarily two-dimensionally at the surface, since the islands in this case grow without further materials supply.

It was found that the InP QDs without any GaP insertion layer shows PL peak at 814 nm and this InP QDs PL peak is overlapping with GaAs buffer photoluminescence peak. After insertion of 1-4 ML GaP layers, InP QDs photoluminescence peaks were observed separately with GaAs buffer layer photoluminescence peaks. When a 1 ML GaP insertion layer is introduced, the PL intensity decreases and blue-shift noticeably with a peak at 786 nm. As the GaP insertion layer thickness increases from 1 ML to 2 ML, the PL intensity increases again and the PL peak blue shifts to 781 nm. But the InP QDs with a 3 ML GaP insertion layer show slightly red shifted PL centered at 780 nm and intensity is decrease again. The insertion of 4 ML GaP insertion layer thickness, the PL peak intensity is red-shifted at 783 nm and PL intensity is higher than other GaP insertion layers thickness. The observed blue and red shifts with GaP insertion layer thickness are due to the reduction and increase in the QDs height respectively.

From the above experimental review, it can concentrate on an approach of GaP insertion layer effect on the structural and optical properties of InP QDs by using MOVPE. The combination of structural and optical results for a given sample is very

useful to analyze the properties of those nanostructures. The insertion of 0 - 4 ML GaP layer achieves increase density and it also reduces the size and height of QDs that were the better conditions for InP QDs. The QDs density increment of 2.3×10^9 cm^{-2} to 4.2×10^9 cm^{-2} has been achieved at a growth temperature of 610°C with a growth rate of 0.5 ML/s.

A thin GaP insertion layer on InP QDs led to a blue-shift of the PL peak. By depositing ultrathin GaP layers on the InGaP barrier before InP QD growth, the PL peak wavelength is continuously reduced with increase of the GaP insertion layer thickness from 0 ML – 2 ML. And then there was no further blue-shift with further increase of the GaP insertion layer thickness from 3 ML to 4 ML. We find that under the same growth conditions, a GaP insertion layer thickness of 2 ML is the optimum where QDs mean size and fluctuation are minimum while giving the higher PL intensity than other thickness of GaP insertion layers.

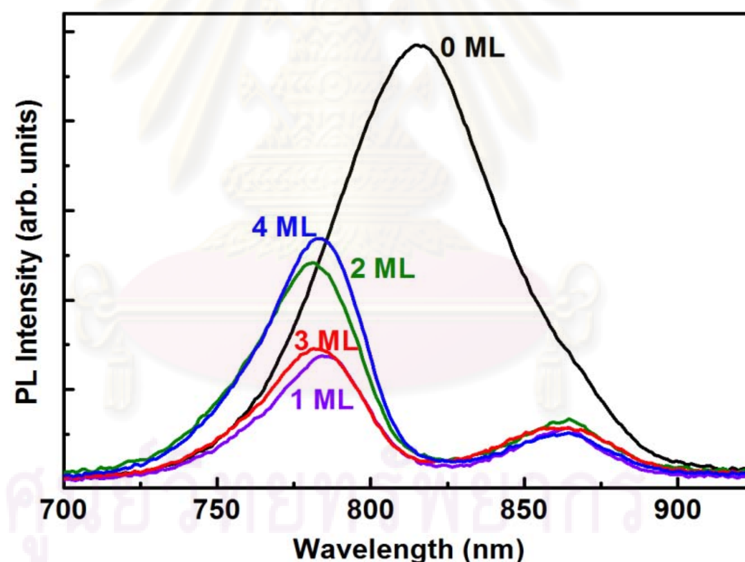

Figure 4.7 The room temperature PL spectra of the InP QDs grown on the InGaP barrier with 0 – 4 ML thick GaP insertion layer between the InP QDs and the InGaP barrier.

In order to investigate the internal quantum efficiency (QE) and the origin of the emission lines, temperature dependent PL measurements were carried out. Low temperature PL spectra were measured over temperatures range (20 – 250 K) using Ar ion laser, a cooled Ge detector and excitation power was carried out 30 mW. The temperature dependent InP QDs PL spectra for 0-4 ML GaP insertion layers are

shown in **figure 4.8 (a), (b), (c), (d) and (e)**. These spectra are shown that the temperature is increased, the decrease in intensity and the redshift of PL peak are observed. **Figure 4.9** shows series of the PL spectra of InP QDs with 0-4 ML GaP insertion layers under various temperatures. It was observed that the emission spectra at 150, 180 and 250 K temperatures for 0-4 MLs GaP insertion layers samples are very similar in shape. With increasing temperature, the total emission intensity decreases, with various temperatures range, which is presumably due to the interplay

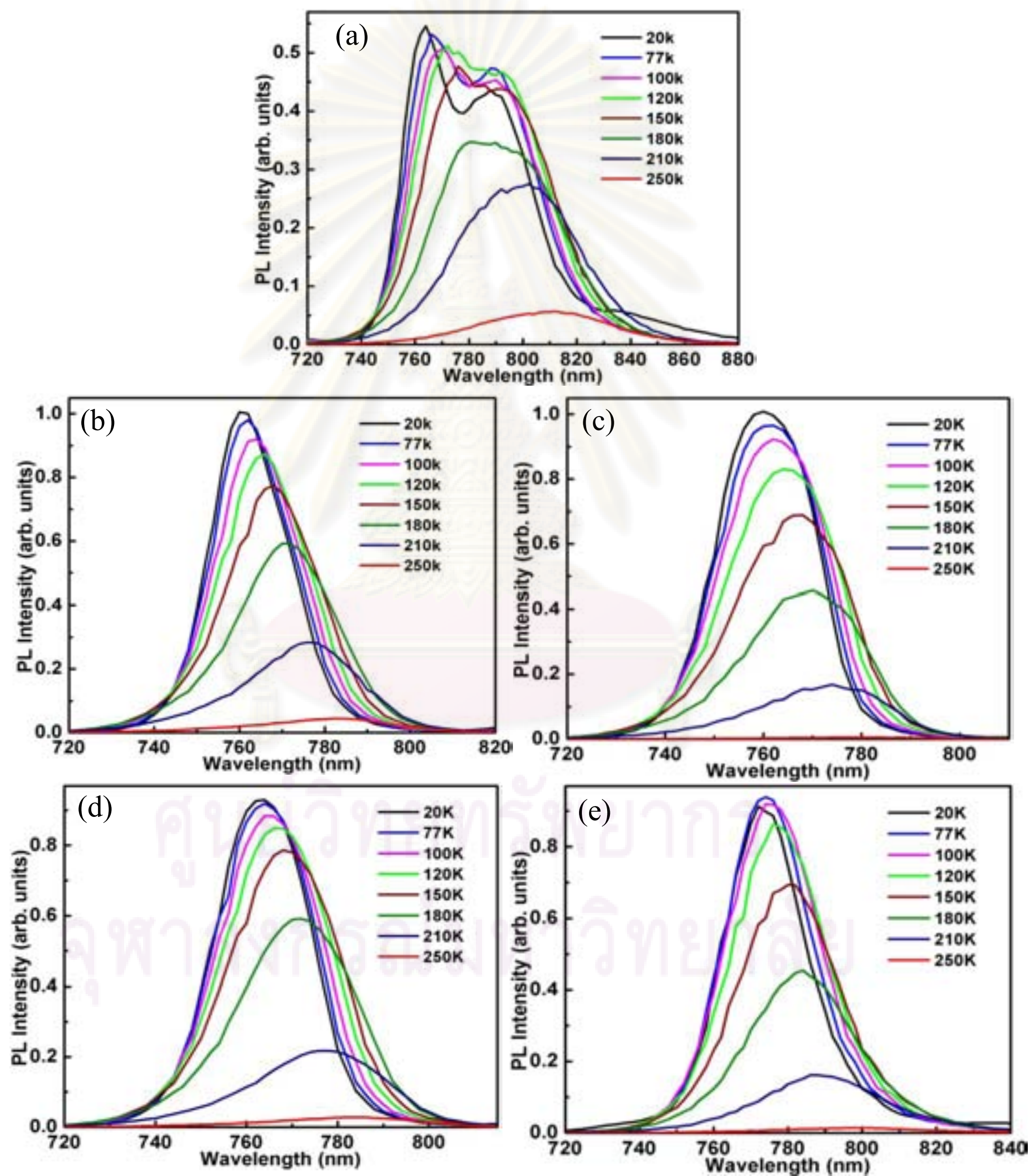

Figure 4.8 The Temperature dependent PL spectra of InP QDs at temperatures range 20-250 K with GaP insertion layers (a) 0 ML (b) 1 ML (c) 2 ML (d) 3 ML (e) 4 ML.

between various capture and recombination channels. Indeed, the spectra of GaP insertion layer samples differ in their energy position, in their spectral width and in their relative intensities from the spectra of no GaP insertion layer sample. It was observed at individual temperature, the PL peak was blueshifted and FWHM was reduced by insertion of GaP layers. This result can be understood in terms of the strain-induced interdiffusion between InP and GaP insertion layers, resulting in the size of the quantum dots becoming smaller.

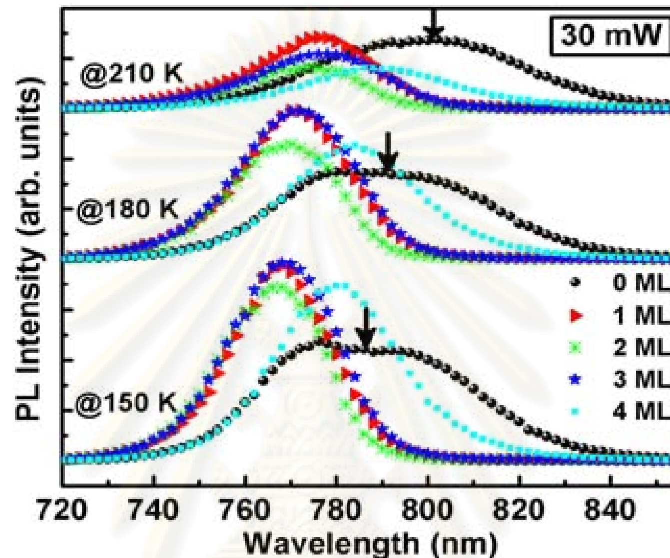

Figure 4.9 Series of the PL spectra of InP QDs with 0-4 ML GaP insertion layers at temperatures range 150, 180 and 210 K.

Figure 4.10 displays the temperature dependence of the PL intensity for InP QDs with 0-4 ML GaP insertion layers. The energy position is quite stable in the range of 20-120 K, which can be attributed to very strong localization of exciton in the QDs. However, when the temperature is above 120 K, the drop off the intensity is notably reduced. The results may reflect a reduction of carrier leakage from the QDs. It is clearly observed that insertion of GaP layers can increase luminescence intensity significantly in the temperature range under ~150 K.

The PL emission wavelength as a function of temperature and the thickness of GaP insertion layers is shown in **Figure 4.11**. The emission wavelength is blue shifted by insertion of GaP layers and it was significantly improved at higher temperatures. The blue shift was significantly observed at 1 and 2 MLs after that a shift was red shifted

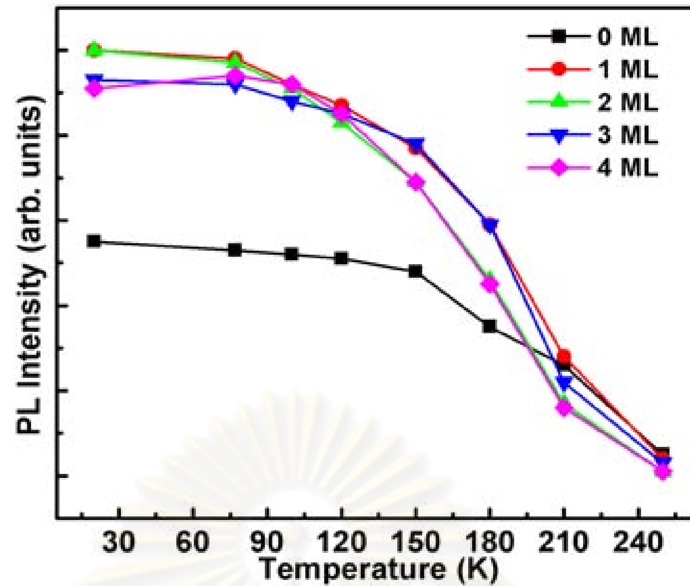

Figure 4.10 The evolution of the temperature dependence of the PL intensity for InP QDs with 0-4 ML GaP insertion layers.

at 3 and 4 MLs due to the effect of dots size fluctuation. The emission shift can be affected by energy barrier height, stress and strain-induced interdiffusion during the GaP insertion layer growth. The shift is affected not only these factors but also by the QDs size and composition. In addition, the insertion of GaP layer enables to tune the QDs luminescence transition within the 0.76-0.81 μm red spectral range.

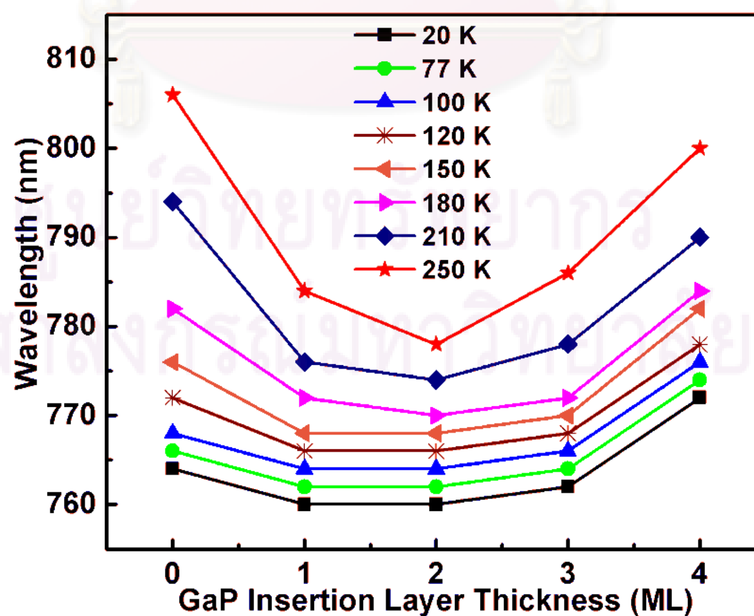

Figure 4.11 The PL emission wavelengths as a function of GaP insertion layers thickness and temperature.

In the review of the results from the above growth conditions, the InP QDs sizes are still large. PL peak intensity is also low and width is still big. So some growth parameters like temperature, growth rate and V-III ratio to improve the size and luminescence properties of InP QDs. The results of these parameters changes will be discussed in the following sections.

4.5.2 Influence of Growth Parameters on InP QDs by MOVPE

In order to control the growth of the self-assembled quantum dots, a lot of effort is put in both theoretical and empirical investigation of the SK growth mechanism. Combinations of many growth parameters like the V/III ratio, the growth rate, the substrate temperature, and the amount of material delivery at the surface are investigated in order to control the shape, size and density of the dots. A brief overview of the effect of temperature, growth rate and V-III ratio are given below.

4.5.2.1 Evolution of InP QDs formation by changing QDs Growth Temperature

The large InP QDs are less commonly observed for MBE grown sample. The main reason is due to the lower growth temperature. Whereas for MOVPE grown samples temperatures beyond 550 °C are frequently used, MBE grown InP/GaAs QDs are usually deposited at temperatures below 500 °C. However, recently larger InP QDs have also been fabricated by MBE at 500 °C. For numerous material systems the effect of growth temperature on the dot size and density has been studied. Common observation is that with lower growth temperature the dot density increases **[115-117]** and smaller dots can be grown **[118-120]**.

The density of the islands decreases with increasing deposition temperature as a consequence of a shorter nucleation period due to faster materials diffusion and island growth. Due to the lower initial density of islands, the excess material distributes over fewer islands and, consequently, the size of the islands increases with temperature. Consequently, at even more reduced growth temperature the dot formation may be suppressed. Furthermore, shape transition of QDs in the InP/GaAs system at different growth temperature has been reported by most of the researchers **[121]**. According to AFM studies of InP QDs samples grown at different

temperatures, the dot density increases for samples with lower growth temperature; at the same time, the base length of dots becomes smaller.

These experiments were done by deposition of 4ML InP on GaAs. InP QDs embedded in $In_{0.49}Ga_{0.51}P$ matrix was carried out in a horizontal MOVPE reactor _AIXTRON, AIX200/4 with a rotating substrate holder on nominally (001) oriented GaAs substrate. All parameters keep at the same growth conditions of the samples grown at 610 °C. The size of the samples grown at 610 °C is still large and density is low. To improve InP QDs properties like decreasing size, increasing density and luminescence intensity with different temperature changes at 475 °C, 500 °C and 550 °C, these three temperature changes samples have been grown.

The parameters of the different temperatures grown samples are shown in **table 4.2**. Actually we have grown these samples to find out the best growth temperature to decrease size and increase density. From these AFM images, the results of temperature changes could not give well InP QDs formation. So, we try to fabricate another InP QDs samples by changing the growth rate and V/III ratio. About these samples results will be discuss in the next section. **Figure 4.12** shows AFM images of three samples (1 × 1 μm^2) having the same InP coverage of about 4 ML but grown at 475 °C and 500 °C and 550 °C respectively.

Table 4.2: The parameters of the samples grown with different temperatures

No:	Samples	QDs Growth Temperature	Growth Rate	V/III Ratio
(a)	No GaP Layer/ No rotation	**475 °C**	0.04 ML/s	18
(b)	No GaP Layer/ No rotation	**500 °C**	0.04 ML/s	18
(c)	No GaP Layer/ No rotation	**550 °C**	0.04 ML/s	18

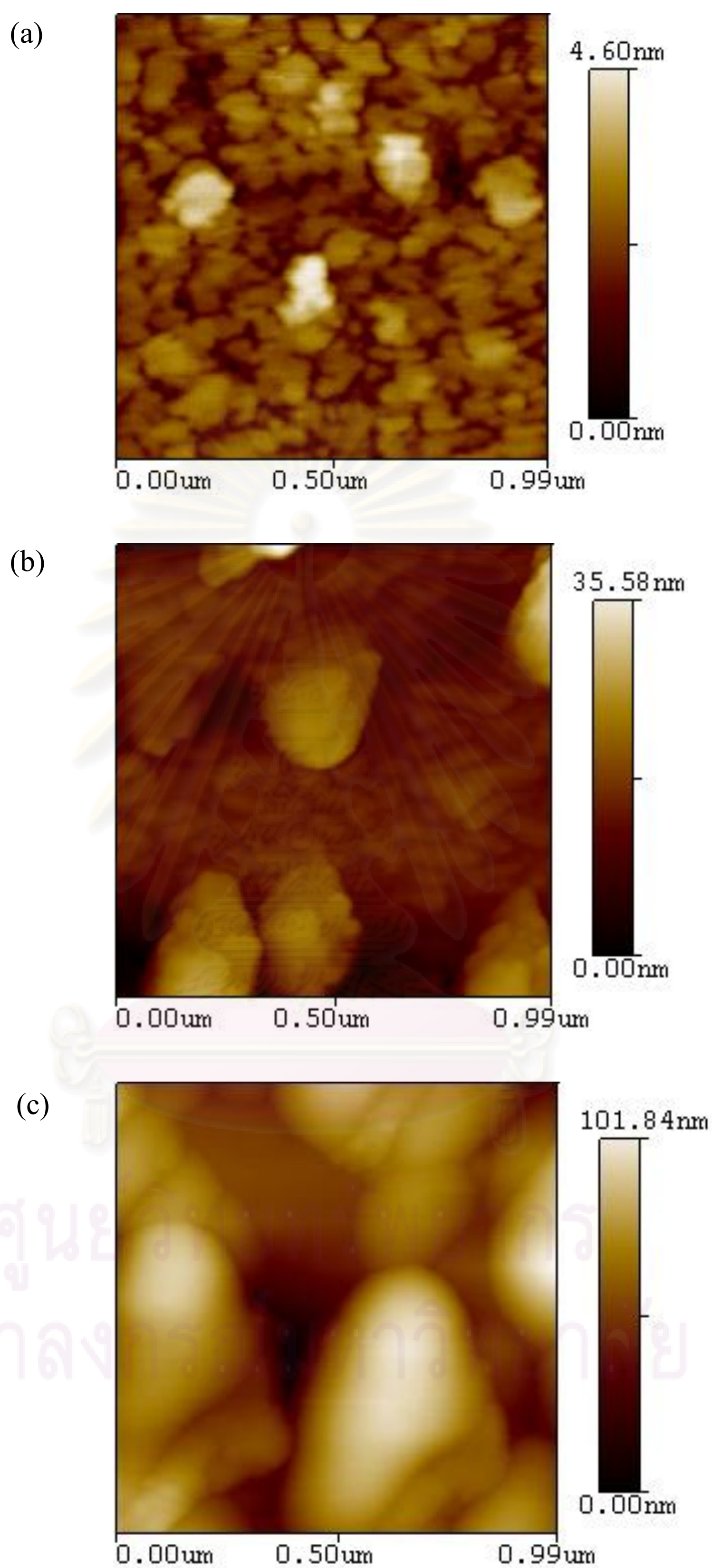

Figure 4.12 The different growth temperature changes of InP QDs grown at (a) 475 °C (b) 500 °C (c) 550 °C

4.5.2.2 Evolution of InP QDs formation by changing III-V Ratio and Growth Rate

Most of the research have been concentrated the effect of growth rate and V/III ratio on the QDs formation. Johansson et al. **[122]** have investigated the growth of InP MOVPE quantum dots on $In_{0.48}Ga_{0.52}P$ for different InP growth rates. According to their observation, the dot density becomes higher with increasing deposition rate. Actually, for low deposition rates the density is linearly proportional to the deposition rate, whereas for high deposition rates a saturation effect of density is observed **[123]**.

Investigation of $InP/In_{0.48}Ga_{0.52}P$ quantum dots grown by MBE with different III/V ratios exhibits that higher phosphorus pressure (lower III/V ratio) results in more homogeneous dot arrays with lower density. This decrease in the dot density is accompanied by an increase of the dot size, involving a shape transition of dots **[124]**. Apparently, lower III/V ratio enhances the ripening rate, which has also been observed for InP/GaP MOVPE QDs **[125]**. The same behavior has been reported for MOVPE $In_xGa_{1-x}P/GaAs$ **[126]**, and for MBE $In_xGa_{1-x}P/GaAs$ QDs **[127]** by most of researchers. On the impact of the ratio between the group V (P) and group III (In and Ga) fluxes, the so-called V/III flux ratio, there are two approaches: The In migration is considered either (i) between the 3D islands **[128, 129]** or (ii) during the 2D growth of the wetting layer **[130]**.

InP QDs embedded in $In_{0.49}Ga_{0.51}P$ matrix was carried out in a horizontal MOVPE reactor _AIXTRON, AIX200/4 with a rotating substrate holder on nominally (001) oriented GaAs substrate. All parameters keep at the same growth conditions of the samples from section 4.5.1. The size of the samples grown at these conditions is still large and density is low. To improve InP QDs properties like decreasing size, increasing density and luminescence intensity, the growth rate of first two samples at 0.04 ML/s and 0.5 ML/s and V/III ratio change of first and third samples at 18 and the second sample at 36 have been grown.

Figure 4.13 shows AFM images of three samples (1×1 μm^2) having the same InP coverage of about 4 ML. Actually we have grown these samples to find out the best conditions for growth rate and V/III ratio to decrease size and increase density. From

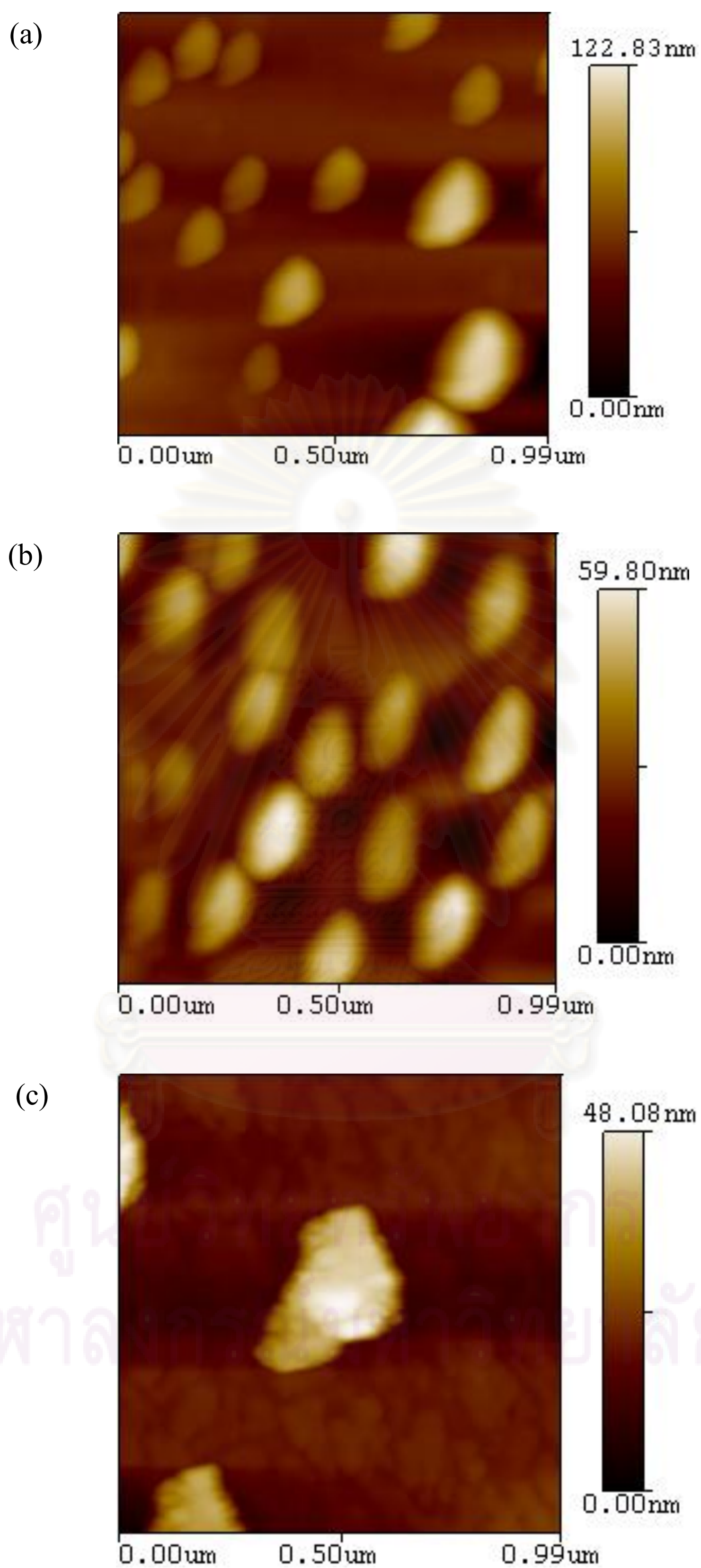

Figure 4.13 The different growth growth rate and V/III ratio changes changes of InP QDs grown at (a) 0.04 ML/s, 16 (b) 0.04 ML/s, 36 (c) 0.04 ML/s, 16.

these AFM images, the results of growth rate and V/III ratio changes could not give well InP QDs formation.

Table 4.3: The parameters of the samples grown with different growth rate and V/III ratio

No:	Samples	Temperature	Growth Rate	V/III Ratio
(a)	No GaP Layer/ No rotation	610 °C	**0.04 ML/s**	**18**
(b)	No GaP Layer/ No rotation	550 °C	**0.04 ML/s**	**36**
(c)	No GaP Layer/ No rotation	550 °C	**0.5 ML/s**	**18**

4.5.3 Effect of InGaP Insertion Layer

For the materials combination InP/InGaP/GaAs the objects for investigation are larger and geometrical differences are more easily visible. Growths of InP embedded in $In_{0.49}Ga_{0.51}P$ matrix were carried out in a horizontal MOVPE reactor _AIXTRON, AIX200/4 with a rotating substrate holder on nominally (001) oriented GaAs substrate. We will focus here two growth structures of InP QDs growth systems by insertion of InGaP layers. In the first structure, the (0-4 ML) InGaP layers are inserted between GaP and InGaP buffer layer like double InGaP layers (figure 3.13, section 3.2.2). In the second structure, the (0, 2, 4 ML) InGaP layers are inserted before the growth of InP QDs (figure 3.12, section 3.2.2).

4.5.3.1 Structural Characterization

The AFM measurement was done to characterize the structural properties of InP QDs by insertion of InGaP insertion layers. The AFM images of the first structure InP QDs samples (1×1 μm^2) having the same InP coverage of about 4 ML are shown in **figure 4.14(a), (b), (c), (d) and (e)**. The average height and diameter of InP QDs

without $In_{0.4}Ga_{0.6}P$ IL are 17 nm and 70 nm. Generally, both size and height are generally decrease by increasing the thickness of GaP insertion layer. The sample with 2 ML GaP insertion layer showed a significantly improved size, height dispersion and homogeneity.

The dot density without $In_{0.4}Ga_{0.6}P$ IL is 4.2×10^9 cm^{-2}. After insertion of 1 ML $In_{0.4}Ga_{0.6}P$ IL, QDs density change to 3.1 $\times10^9$ cm^{-2} and then slightly increase again to 3.3 $\times10^9$ cm^{-2} by increasing the thickness of $In_{0.4}Ga_{0.6}P$ IL to 2 ML. After insertion of 2 ML $In_{0.4}Ga_{0.6}P$ IL thicknesses, the QDs size was quite increase and density was also slightly increase again. This observation indicated that the thickness of $In_{0.4}Ga_{0.6}P$ IL did not significantly increase the density of QDs. It is likely that the incorporation efficiency of In during the deposition of $In_{0.4}Ga_{0.6}P$ IL layer reduces as the strain increases. The smaller and better uniformity of InP QDs at 2 ML $In_{0.4}Ga_{0.6}P$ IL is around 16 nm height and 50 nm diameter. The height distribution histogram is shown in **figure 4.15**.

The comparison of density and diameter of InP QDs grown with $In_{0.4}Ga_{0.6}P$ insertion layers are shown in **figure 4.16**. By using an InGaP IL, the average InP QD height and diameter are reduced to 16 nm and 50 nm and these are also good for QDs quality **[131]**. The introduced strain in the lower $In_{0.49}Ga_{0.51}P$ barrier strongly influences the InP QD growth, in a sense that the same amount of material is deposited but is rearranged in more and smaller QDs. This behavior becomes also obvious in the QD density, compared to the case without $In_{0.4}Ga_{0.6}P$ IL (highest InP QD density: 4.2×10^9 cm^{-2}) the density is reduced to 3.3 $\times10^9$ cm^{-2}. Since the QDs growth conditions are the same, the smaller the QDs size and reduced density for the samples grown with InGaP IL results in less incorporation of the material. On the InGaP surface, there could be an indium segregated layer which may be favorable for the nucleation of InP QDs leading to increased QDs density. The $In_{0.49}Ga_{0.51}P$ insertion layer may consume this segregated indium layer thereby block preferential nucleation sites. As a result, besides the QDs density slightly increase and mean QDs height, the QDs size fluctuation is also increases. By increasing of $In_{0.49}Ga_{0.51}P$ insertion layer thickness, InP QDs density increases, not too much changes of size and QDs uniformity is improved. This is also a result of the influence of $In_{0.49}Ga_{0.51}P$ IL on the topmost layer InP QDs.

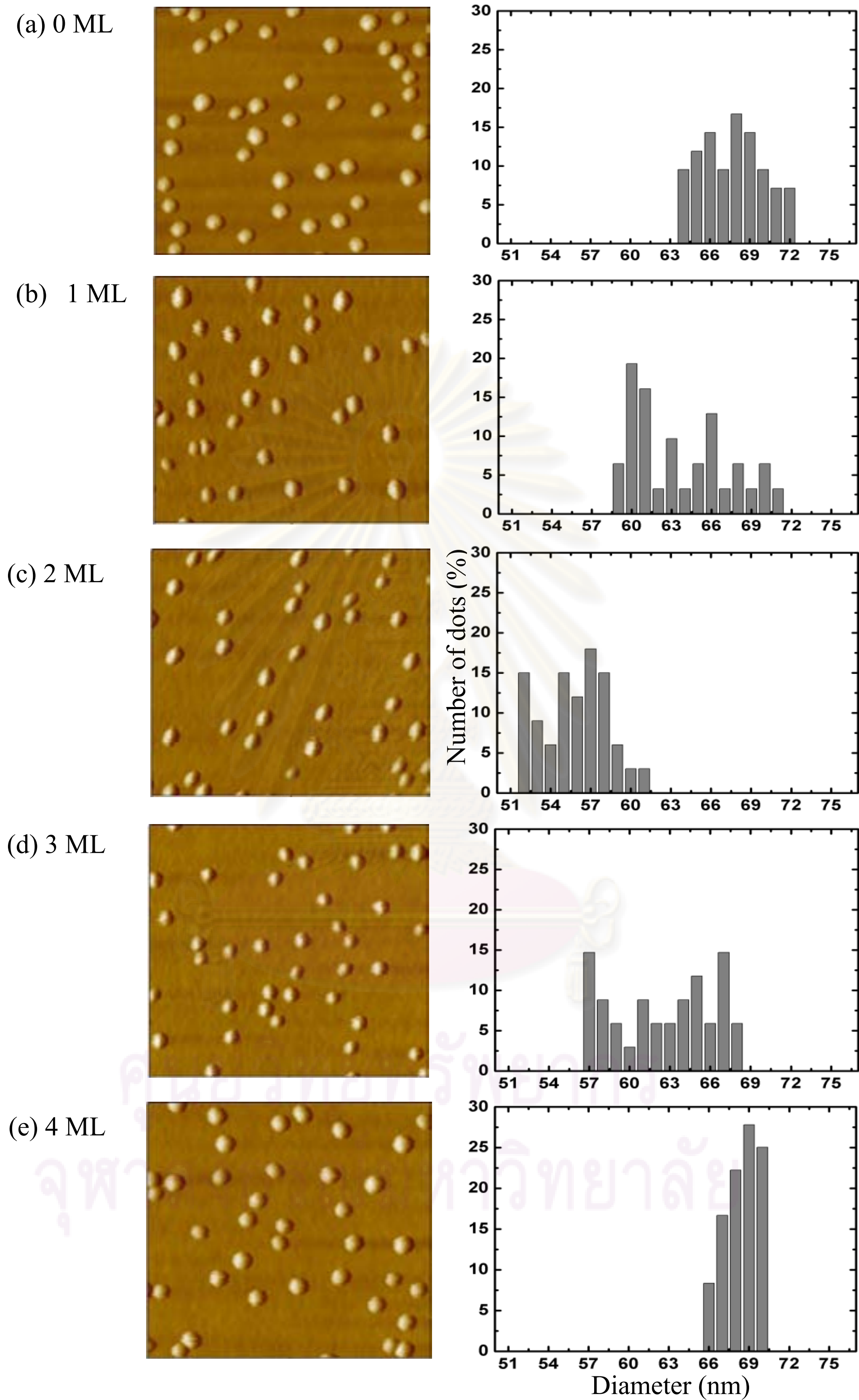

Figure 4.14 Typical (1μm × 1μm) scan range AFM images and diameter histogram graph of InP QDs embedded in InGaP barrier with $In_{0.4}Ga_{0.6}P$ insertion layers (a) 0 ML (b) 1 ML (c) 2 ML (d) 3 ML and (d) 4 ML.

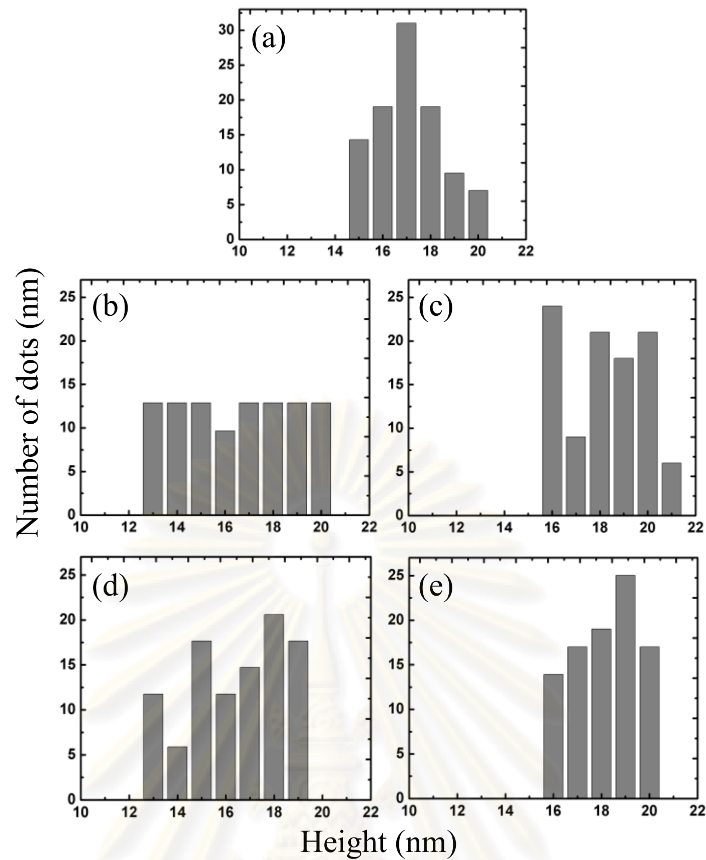

Figure 4.15 Height distribution histogram graph of InP QDs embedded in InGaP barrier with $In_{0.4}Ga_{0.6}P$ insertion layers (a) 0 ML (b) 1 ML (c) 2 ML (d) 3 ML and (d) 4 ML.

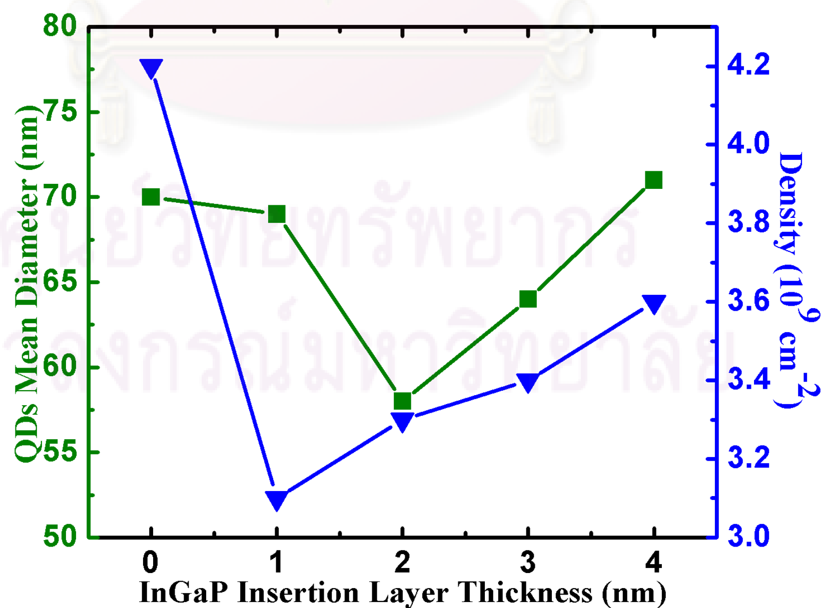

Figure 4.16 Effect of size and density of $In_{0.49}Ga_{0.51}P$ insertion layers on InP SAQDs embedded in InGaP grown at 610 °C

As a characterization of the structural properties of the second structure InP QDs growth system by insertion of (0, 2, 4 ML) InGaP layers before the growth of InP QDs, the AFM measurement has been performed. The average height and diameter of InP QDs without InGaP IL are 25 nm and 85 nm. Both size and height are generally increase by increasing the thickness of InGaP insertion layer. The sample with 2 ML InGaP insertion layer showed average diameter at 93 nm and average height at 17 nm. The dot density decreases from 2.3×10^9 cm^{-2} to 1.6×10^9 cm^{-2} due to insertion of 0 ML to 2 ML GaP layers and then density is a little bit increase again to 2.1×10^9 cm^{-2} due to insertion of 4 ML GaP layer. After insertion of 2 ML and 4 ML InGaP layer thickness, the QDs size was quite increase and density was decrease. This observation indicated that QDs density decreased with increasing of InGaP insertion layer thickness. It is likely that the incorporation efficiency of In during the deposition of GaP layer reduces as the strain increases.

Actually, these InGaP insertion layer grown samples have been fabricated as a reason of comparison of GaP insertion layer samples. Although all the growth conditions are the same, the effect of GaP and InGaP insertion layers are different. AFM images of InGaP insertion layer grown samples are shown in **figure 4.17**. In the comparison of density and diameter of InP QDs grown with GaP and InGaP insertion layers, the better improvement of InP QDs properties can be observed in GaP insertion layer samples.

By using an GaP IL, the average InP QD height and diameter are reduced and these values are also less than the size of InGaP IL samples **[132]**. The introduced strain in the $In_{0.4}Ga_{0.6}P$ insertion layer strongly influences the InP QD growth, in a sense that the same amount of material is deposited but is rearranged in less and bigger QDs. This behavior becomes also obvious in the QD density, compared to the case with GaP IL (highest InP QD density at 2 ML GaP layer: 4.2×10^9 cm^{-2}) the density is reduced to 1.6×10^9 cm^{-2} at 2 ML $In_{0.4}Ga_{0.6}P$ insertion layer. Since the QDs growth conditions are the same, the bit increase the QDs size and reduced density for the samples grown with InGaP IL results in less incorporation of the material. The $In_{0.4}Ga_{0.6}P$ insertion layer may consume segregated InP QDs layer thereby block preferential nucleation sites. As a result, besides the QDs density decreases and mean QDs height, the QDs size fluctuation is also decreases.

Height histograms of InP QDs that were extracted from 1×1 μm^2 AFM images are shown in **figure 4.18**. Generally, it can be concluded that $In_{0.4}Ga_{0.6}P$ insertion layer cannot improve size uniformity, fluctuation and density of InP QDs like GaP IL. The GaP IL samples show more uniformity and fluctuate to compare that the results of InGaP ILs. Therefore, InP quantum dots size and densities depend on the thickness of GaP and InGaP insertion layers at the same growth conditions. **Figure 4.19** shows the relation of dot density and diameter of InP QDs as a function of the InGaP insertion layer thickness. It is observed that with the increasing InGaP ILs thickness,

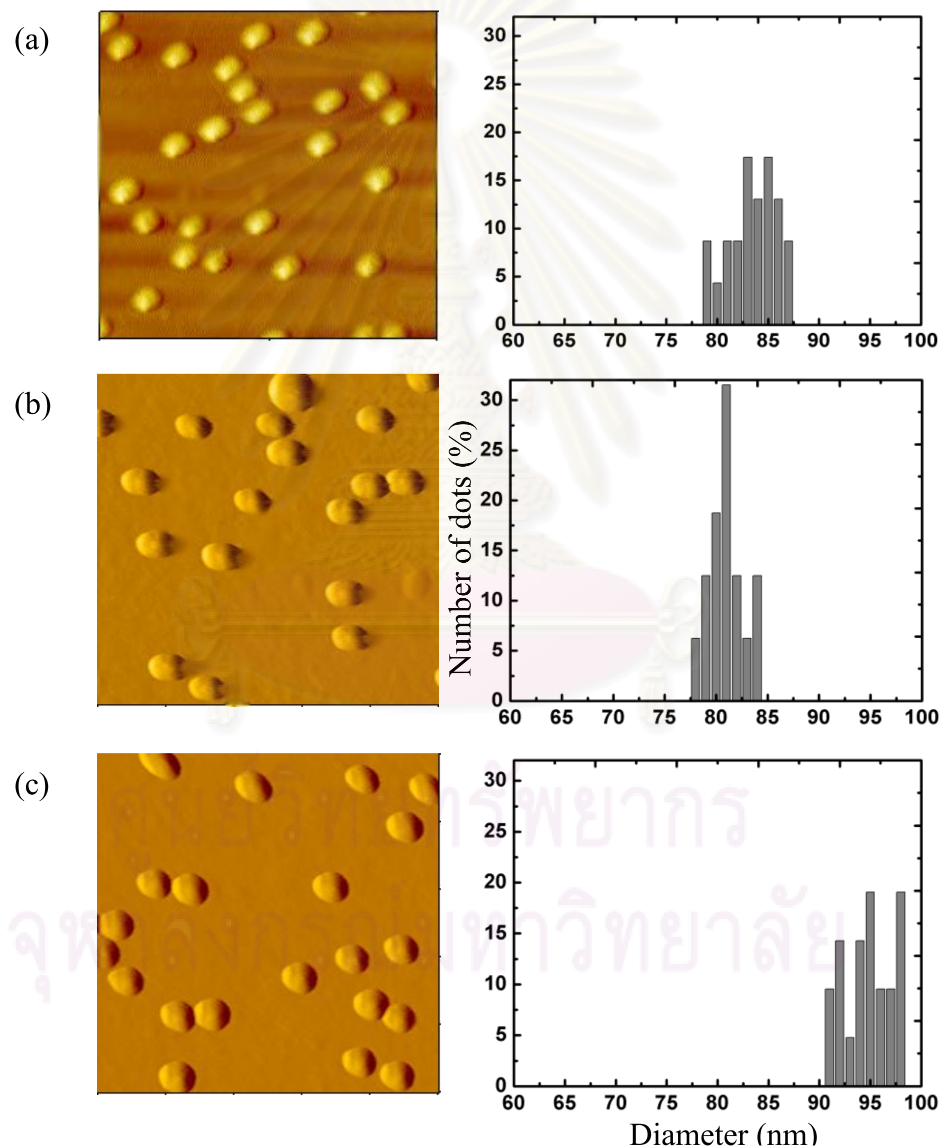

Figure 4.17 Typical (1µm × 1µm) scan range AFM images and diameter histogram graph of InP QDs embedded in InGaP barrier with $In_{0.4}Ga_{0.6}P$ insertion layers (0, 2, 4) MLs.

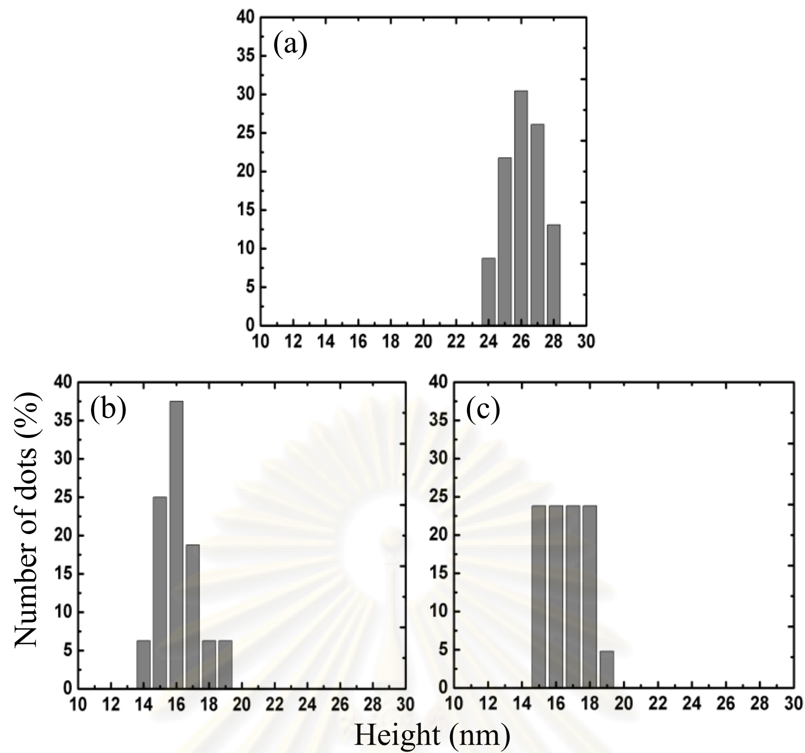

Figure 4.18 Height distribution histogram graph of InP QDs embedded in InGaP barrier before the growth of InP QDs (a) 0 ML (b) 2 ML (c) 4 ML.

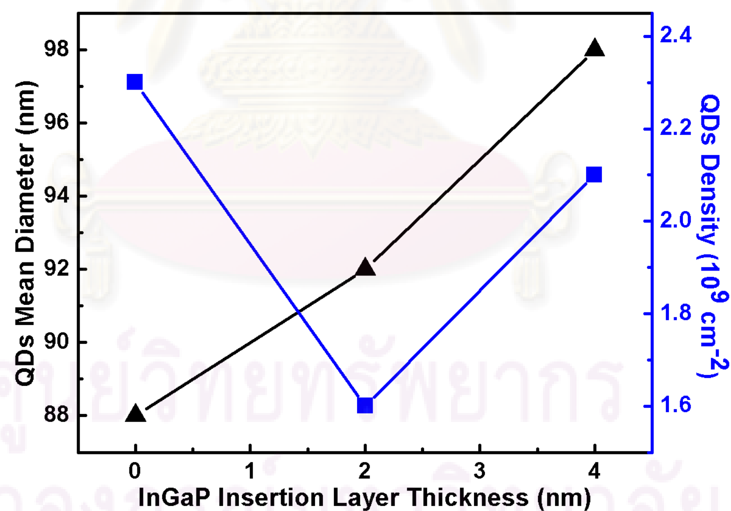

Figure 4.19 Effect of size and density of $In_{0.4}Ga_{0.6}P$ insertion layers on InP SAQDs embedded in InGaP grown at 610 °C

the QDs density decreases and size increase **[131]**. Although this is also an reasonable result, it is not good improvement for InP QDs properties. The optical properties of these InGaP insertion layer effect will be discussed in the next section.

4.5.3.2 Optical Characterization

Photoluminescence measurement is the best way to reveal the unique zero-dimensional systems of single dots. The density of states is revealed by the very narrow spectral lines that are emitted by single QDs. The visible spectral range is accessible with InP quantum dots. Red-emitting islands can be grown either with OMCVD or with MBE at temperatures beyond 550 °C or around 500 °C, respectively. Typically, GaAs (001) substrates are used, on which lattice-matched $In_{0.49}Ga_{0.51}P$ buffer layers are deposited prior to island growth. The PL spectrum was obtained at room temperature and was excited by the 532 nm line of solid state laser. The PL signal was collected by an InGaAs photo-detector with solid-state laser. The optical characterization of two InGaP insertion layers samples result will be described in the following section.

Figure 4.20 shows the normalized PL spectra of InP QDs by insertion of $In_{0.4}Ga_{0.6}P$ layers between GaP layer and $In_{0.49}Ga_{0.51}P$ layer that emitting at various emission wavelengths. The ensemble PL measurements reveal already drastically changed optical properties of the InP QDs grown with $In_{0.4}Ga_{0.6}P$ IL thickness. The PL spectrum of InP without $In_{0.4}Ga_{0.6}P$ insertion layer shows PL peak at 781 nm. When

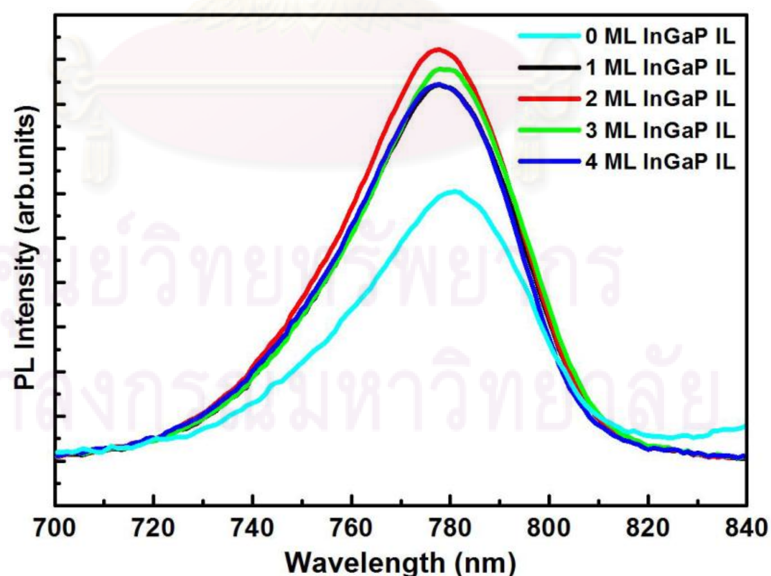

Figure 4.20 The room temperature PL spectra of the InP QDs grown on the $In_{0.49}Ga_{0.51}P$ barrier with 0- 4 ML thick $In_{0.4}Ga_{0.6}P$ insertion layers between GaP and InGaP layers

the InGaP layer is inserted between the GaP buffer and the underneath InGaP buffer, a significant increase in PL intensity is observed while the linewidth of the spectrum remained almost unchanged from the PL peak without $In_{0.4}Ga_{0.6}P$ IL.

Since the less QDs size fluctuation of $In_{0.4}Ga_{0.6}P$ IL samples, the better PL linewidth as can be seen from the PL spectra. Since the less QDs size fluctuation of $In_{0.4}Ga_{0.6}P$ IL samples, the better PL linewidth as can be seen from the PL spectra. In $In_{0.4}Ga_{0.6}P$ ILs, 2 ML thickness is noticeably improved intensity among other thicknesses. It indicates that an increased number of optically active InP QDs at this layer thickness. In the PL spectra of $In_{0.4}Ga_{0.6}P$ IL samples, the PL emission of InP QDs is at 777 nm. This red spectral range is also preferable to generate highest photon detection efficiency for single-photon detectors. Additionally, the InP QDs with $In_{0.4}Ga_{0.6}P$ ILs must influence the optical properties of possible quantum optic devices which have to be carried out in future work.

Similarly, low temperature PL spectra were measured over temperatures range (20 – 250 K) for 0-4 ML InGaP insertion layers samples. PL measurements were carried out by using Ar ion laser, a cooled Ge detector and excitation power was used 10 mW. The temperature dependent InP QDs PL spectra for 0-4 ML InGaP insertion layers are shown in **figure 4.21 (a), (b), (c), (d) and (e)**. These spectra are shown that the temperature is increased, the decrease in intensity and the redshift of PL peak are observed. **Figure 4.22** shows series of the PL spectra of InP QDs with 0-4 ML InGaP insertion layers under various temperatures. It was observed that the emission spectra at 150, 180 and 250 K temperatures for 0-4 MLs InGaP insertion layers samples are very similar in shape.

With increasing temperature, the total emission intensity decreases, with various temperatures range, which is presumably due to the interplay between various capture and recombination channels. Indeed, the spectra of InGaP insertion layer samples differ in their energy position, in their spectral width and in their relative intensities from the spectra of no InGaP insertion layer sample. It was observed at individual temperature, the PL peak was blueshifted and FWHM was invaried by insertion of InGaP layers. This result can be understood in terms of the strain-induced interdiffusion between InP and InGaP insertion layers, resulting in the size of the quantum dots becoming smaller.

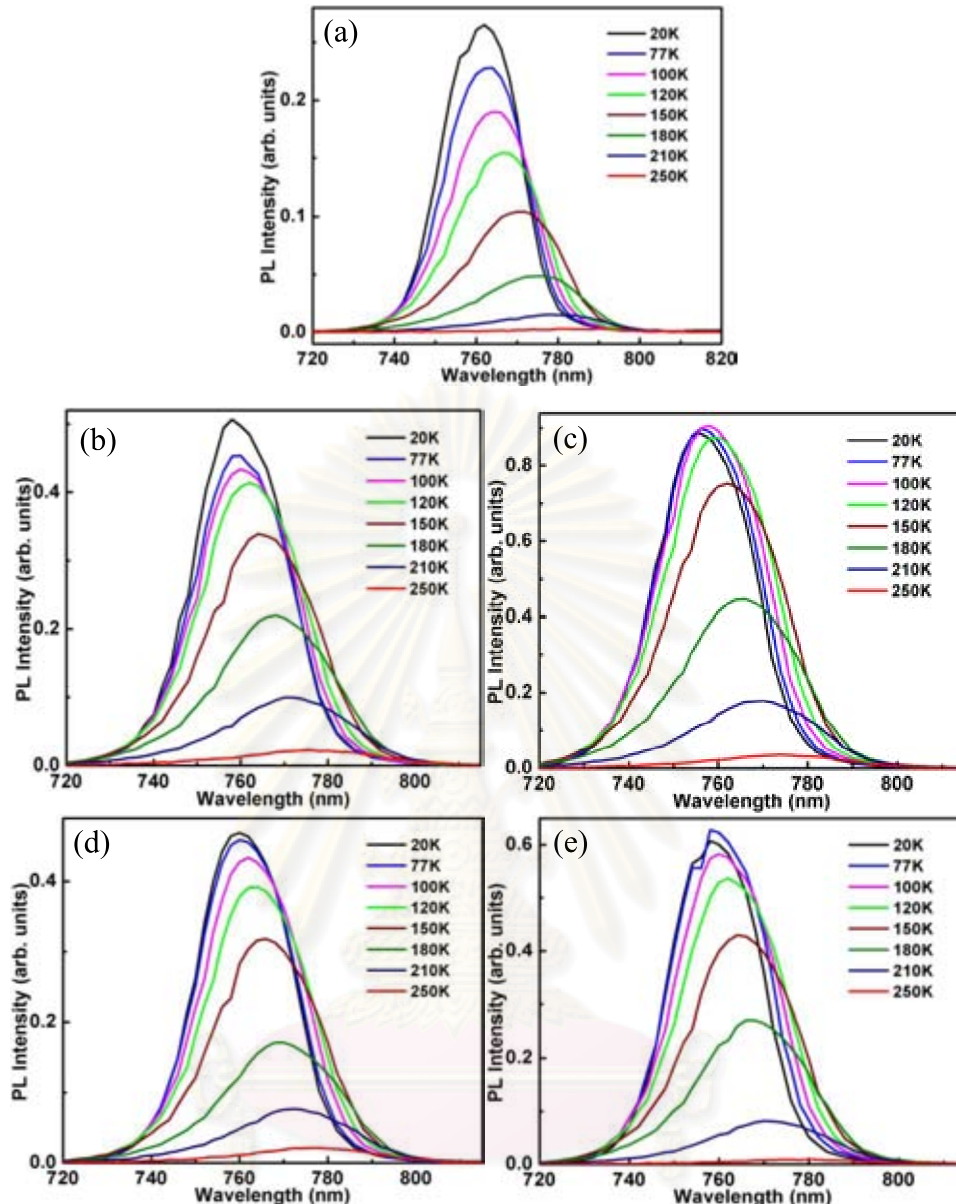

Figure 4.21 The Temperature dependent PL spectra of InP QDs at temperatures range 20-250 K with InGaP insertion layers (a) 0 ML (b) 1 ML (c) 2 ML (d) 3 ML (e) 4 ML.

ศูนย์วิทยทรัพยากร
จุฬาลงกรณ์มหาวิทยาลัย

Figure 4.23 displays the temperature dependence of the PL intensity for InP QDs with 0-4 ML InGaP insertion layers. The energy position is quite stable in the range of 20-120 K, which can be attributed to very strong localization of exciton in the QDs. However, when the temperature is above 120 K, the drop off the intensity is notably reduced. The results may reflect a reduction of carrier leakage from the QDs. It is clearly observed that insertion of InGaP layers can increase luminescence intensity significantly in the temperature range under ~150 K.

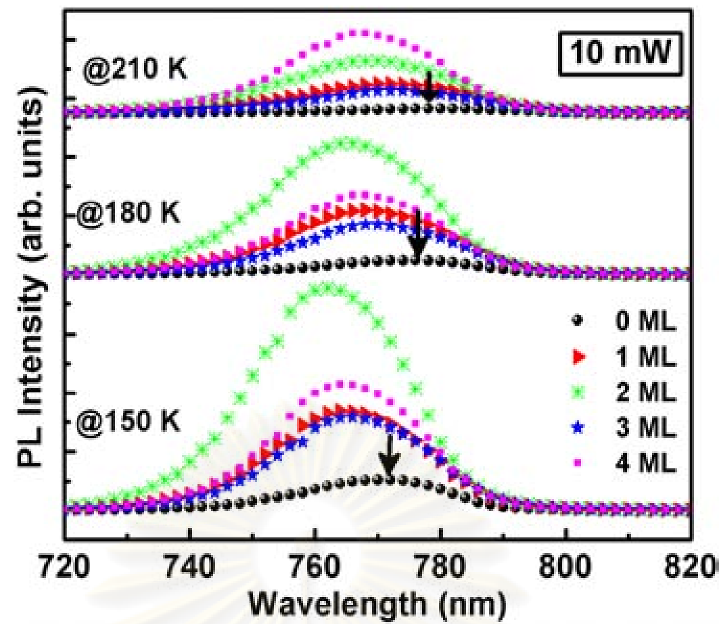

Figure 4.22 Series of the PL spectra of InP QDs with 0-4 ML InGaP insertion layers at temperatures range 150, 180 and 210 K.

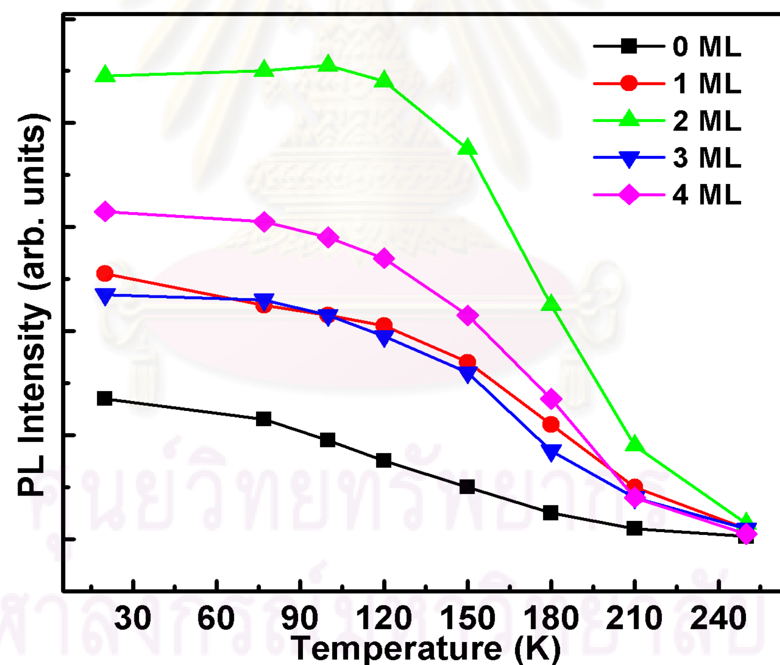

Figure 4.23 The evolution of the temperature dependence of the PL intensity for InP QDs with 0-4 ML InGaP insertion layers.

The PL emission wavelength as a function of temperature and the thickness of InGaP insertion layers is shown in **Figure 4.24**. The emission wavelength is blue shifted by insertion of InGaP layers and it was significantly improved at higher temperatures. The blue shift was significantly observed at 1 and 2 MLs after that there was no

shifted at 3 and 4 MLs due to the effect of dots size fluctuation. The emission shift can be affected by energy barrier height, stress and strain-induced interdiffusion during the InGaP insertion layer growth. Thus, the insertion of InGaP layer enables to tune the QDs luminescence transition within the 0.75-0.79 μm red spectral range.

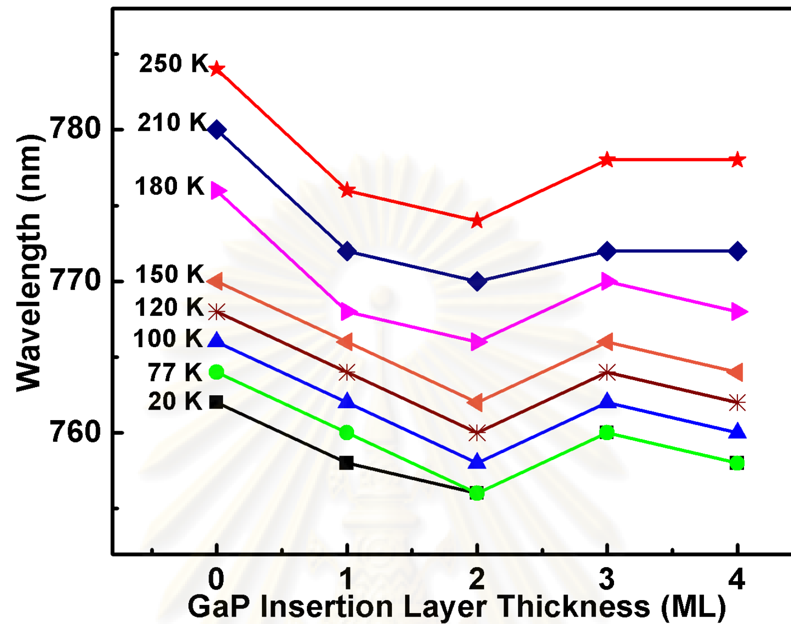

Figure 4.24 The PL emission wavelengths as a function of InGaP insertion layers thickness and temperature.

Thin $In_{0.4}Ga_{0.6}P$ insertion layers effect on InP QDs led to improve intensity of the PL peak. As a result of $In_{0.4}Ga_{0.6}P$ IL samples, besides the increase of QDs density and mean diameter, the QDs size fluctuation also decreases and thus the broad of PL linewidth reduces and PL intensity increases. Under the same growth conditions, 2 ML ILs thickness is the optimum where QDs mean size and fluctuation are minimum while giving the higher PL intensity than other thickness of $In_{0.4}Ga_{0.6}P$ ILs. Since InGaP ILs improve the structure and PL quality of the InP QDs.

In the optical characterization of second growth structure, the PL spectra of InP QDs by Insertion $In_{0.4}Ga_{0.6}P$ Layer before the growth of InP QDs will be discussed. The room temperature (RT) PL spectra of InP QDs grown on $In_{0.4}Ga_{0.6}P$ Layer are shown in **figure 4.25**. The ensemble PL measurements reveal already drastically changed optical properties of the InP QDs grown with $In_{0.4}Ga_{0.6}P$ Layer compared to samples with GaP IL. The PL spectrum without insertion layer shows PL peak at 814 nm and this InP QDs PL peak is overlapping with GaAs buffer photoluminescence peak.

After insertion of 2and 4 ML $In_{0.4}Ga_{0.6}P$ Layers, the PL intensity decreases and blue-shift could not shown in this PL spectra. Since the more QDs size fluctuation of $In_{0.4}Ga_{0.6}P$ Layer, broader the PL linewidth as can be seen from the PL spectra.

The spectrum (of OR from) InP QDs with 0.4 indium content comprises a broad peak at 803 nm and 806 nm for 2 ML and 4 ML $In_{0.4}Ga_{0.6}P$ insertion layers. Comparing this result with InP QDs by insertion of GaP layer samples, the PL intensity is lower than GaP insertion layer samples. The QDs size fluctuation also increases and thus the broad of PL linewidth increases and PL intensity decreases. Since insertion of InGaP ILs before the growth of InP QDs could not improve significantly the structure and PL quality of the InP QDs like GaP insertion layer samples.

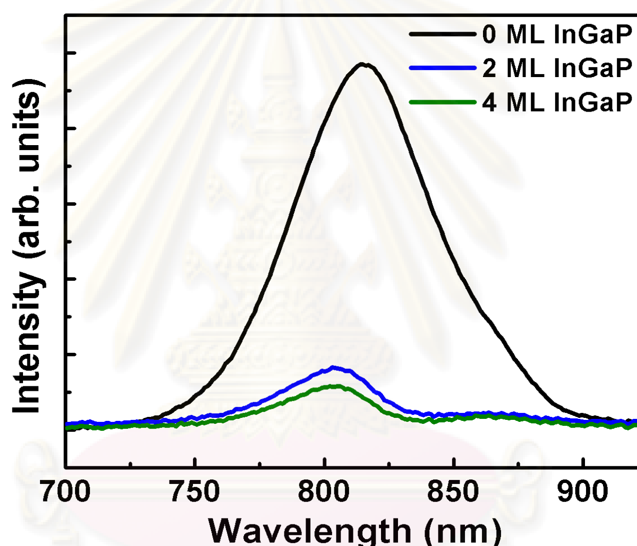

Figure 4.25 The room temperature PL spectra of the InP QDs grown on the $In_{0.49}Ga_{0.51}P$ barrier by insertion of 0, 2, 4 ML thick $In_{0.4}Ga_{0.6}P$ layers before the growth of InP QDs

Low temperature PL spectra were measured over temperatures range (20 – 250 K). PL measurements were carried out the same set-up like previous measurement. The temperature dependent InP QDs PL spectra for 0, 2, 4 ML InGaP insertion layers are shown in **figure 4.26 (a), (b) and (c)**. These spectra are shown that the temperature is increased, the decrease in intensity and the redshift of PL peak are observed. **Figure 4.27** shows series of the PL spectra of InP QDs with 0, 2, 4 ML InGaP insertion layers at 150, 180 and 250 K temperatures. The blue shift was observed at 2 ML InGaP IL and the significantly red shift was observed at 4 ML InGaP IL.

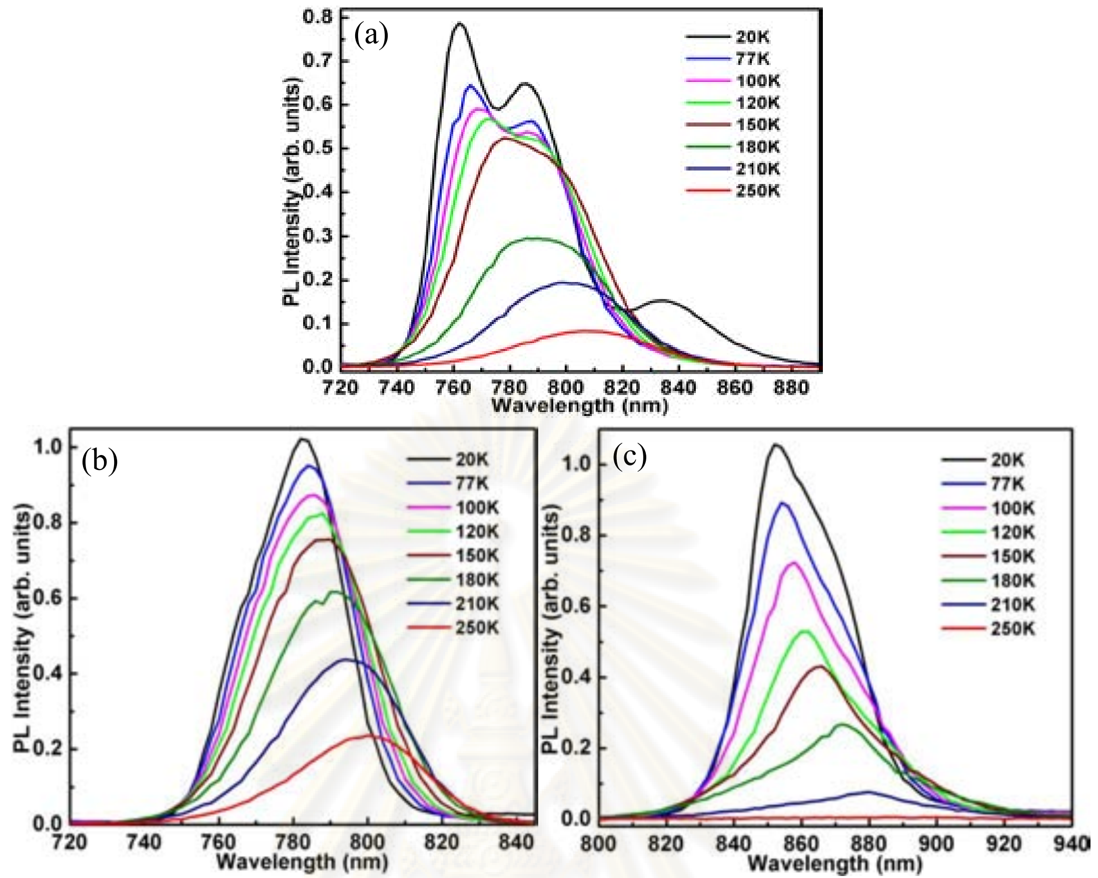

Figure 4.26 The Temperature dependent PL spectra of InP QDs at temperatures range 20-250 K with InGaP insertion layers (a) 0 ML (b) 2 ML (c) 4 ML

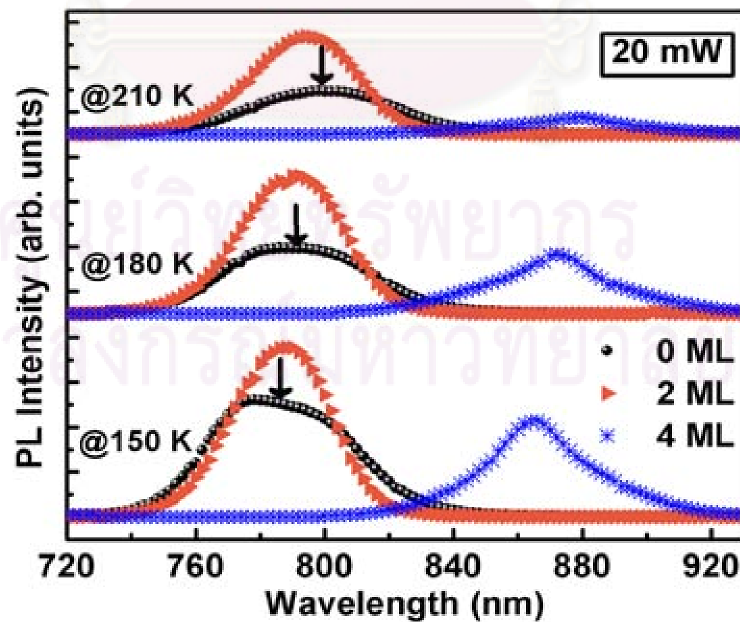

Figure 4.27 Series of the PL spectra of InP QDs with 0, 2, 4 ML InGaP insertion layers at temperatures range 150, 180 and 210 K.

The origin of these PL spectra was observed the same trend like previous InGaP insertion layers. **Figure 4.28** displays the temperature dependence of the PL intensity for InP QDs with 0, 2, 4 ML InGaP insertion layers. When the temperature is increased, the drop off the intensity is reduced. The results may reflect a reduction of carrier leakage from the QDs. It is clearly observed that insertion of 2 ML InGaP layers can increase luminescence intensity significantly.

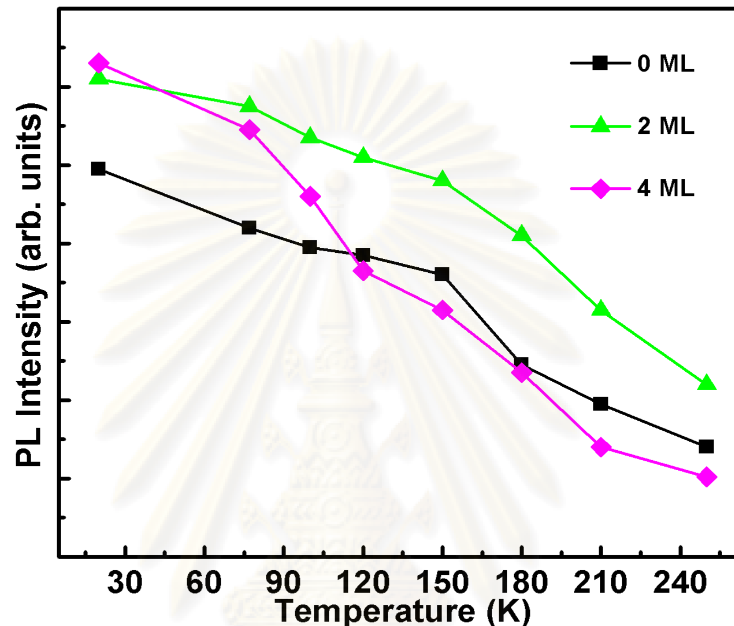

Figure 4.28 The evolution of the temperature dependence of the PL intensity for InP QDs with 0, 2, 4 ML InGaP insertion layers.

The PL emission wavelength as a function of temperature and the thickness of InGaP insertion layers is shown in **Figure 4.29**. The emission wavelength is blue shifted by insertion of 2 ML InGaP layers and it was significantly improved at higher temperatures. The emission shift can be affected by energy barrier height, stress and strain-induced interdiffusion during the InGaP insertion layer growth. Thus, the insertion of InGaP layer enables to tune the QDs luminescence transition within the 0.765-0.886 μm red spectral range. Indeed, the spectra of InGaP insertion layer samples differ in their energy position, in their spectral width and in their relative intensities from the spectra of no InGaP insertion layer sample.

The effect of the GaP and InGaP insertion layers can also be understood in terms of strength of interaction between the InP QDs layer and strain / relaxation of insertion

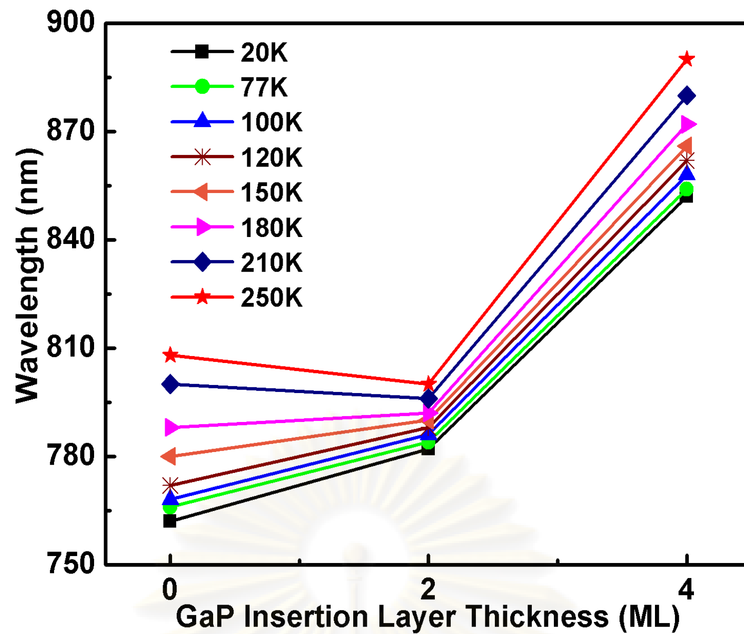

Figure 4.29 The PL emission wavelengths as a function of InGaP insertion layers thickness and temperature.

layer. Measurements of the luminescence intensity of emission from these structures in relation to temperature (20-250 K) demonstrated that the PL spectra are a superposition of emissions from QDs.

In order to get the more complete information of the InP QDs by insertion of GaP and InGaP layers, we performed InP embedded in $In_{0.49}Ga_{0.51}P$ matrix in GaAs substrate with Stranski-Krastanow mode by MBE and MOVPE. The AFM and PL measurements were used to characterize the structural and optical properties of InP QDs. The results and discussion of these GaP and InGaP insertion samples are described in this chapter.

ศูนย์วิทยทรัพยากร
จุฬาลงกรณ์มหาวิทยาลัย

CHAPTER V

Conclusions

Within this work growth of self-assembled InP QDs embedded in $In_{0.49}Ga_{0.51}P$ matrix on GaAs substrates was presented and discussed. The growth was performed both molecular beam epitaxy (MBE) and metal organic vapour phase epitaxy (MOVPE) systems by using Stranski-Krastanow technique. InP QDs formed in the Stranski-Krastanow mode were investigated with the purpose of implementation as an active zone of single photon detector and laser. The effect of GaP and InGaP insertion layers on self-assembled InP quantum dots are presented and discussed, together with their growth, structural and optical properties. It has demonstrated that the understanding of self-assembling InP QDs as the dependence of sizes and densities of QDs on GaP and InGaP insertion layers finds its natural properties. Most studies had been concentrated on InAs or InGaAs quantum dots in GaAs. This work had been reviewed the understanding of the less studied, but equally interesting, system of InP quantum dots in InGaP.

The InP QDs are grown using molecular-beam epitaxy (MBE) and metal-organic vapor phase epitaxy (MOVPE) on the two materials $In_{0.49}Ga_{0.51}P$ (lattice matched to GaAs) and $In_{0.48}Ga_{0.52}P$. In the growth of InP/InGaP/GaAs self-assembled quantum dots (SAQDs), even though the bimodal size distribution for the coherent islands can be overcome by using GaP and InGaP insertion layers, the island size is still large and the areal density of dots is low. Since large dots may introduce dislocations and low density leads to poor optical efficiency, growth of small size, high density and uniformity of InP dots becomes imperative. For this reason, the growth of InP QDs by GaP and InGaP insertion layers had been observed in this work.

Under the proper growth conditions, formation of InP QDs via the Stranski-Krastanow mechanism was observed. The critical InP coverage for insertion of GaP layer is found to be 3 ML for the InP/ $In_{0.48}Ga_{0.52}P$/GaAs system in MBE growth system and 2 ML for the InP/ $In_{0.49}Ga_{0.51}P$/GaAs system. The structural characterization from atomic force microscopy (AFM) measurements indicates that the MBE growth of InP/ $In_{0.48}Ga_{0.52}P$ QDs are larger and, consequently, more dense

compared to the MOVPE growth of InP/ $In_{0.49}Ga_{0.51}P$ QDs. Hence, InP dots on $In_{0.48}Ga_{0.52}P$ tend to be strain-relaxed when GaP insertion layer thickness is increased. The InP/$In_{0.49}Ga_{0.51}P$ QDs tend to form small QDs when InGaP insertion layer thickness is increased.

The research work was focused on two main parts: The first part emphasizes on the properties of linearly aligned quantum dots from the experimental point of view. The second part deals with the investigation of linearly aligned quantum dots from the theoretical point of view. The QD growth was also investigated from a point of view how different growth parameters, such as growth temperature, V/III ratio, growth rate and others influence the optical and structural properties of InP QDs by insertion of GaP and InGaP layers.

A significant difference was found between MBE and MOCVD growth concerning the evolution of InP QDs by changing the GaP and InGaP insertion layer thickness. Some parameter could not keep at the same conditions in these two systems. The composition of InP QDs by changing the GaP and InGaP insertion layer thickness was found to have a great impact on QD parameters such as size and density. InP QDs have generally a bimodal size distribution and often contain dislocated clusters.

Altogether, InP QDs are an attractive system for optical application. The optical gain and lasing in InP/$In_{0.48}Ga_{0.52}P$ QDs has been demonstrated by Moritz et al.; the vertical-cavity surface-emitting laser based on InP/$In_{0.48}Ga_{0.52}P$ QDs has recently been fabricated. Ryou et al. succeeded in fabricating photopumped red-emitting laser using aluminum in the matrix ($In_{0.5}Al_{0.3}Ga_{0.2}P$). All of these structures were grown on GaAs substrate. Initial study of the growth of InP QDs was done by Petroff *et al* and Carlsson *et al* using metal-organic vapor phase epitaxy (MOVPE). In this work, the InP QDs was grown on the two materials $In_{0.48}Ga_{0.52}P$ and $In_{0.49}Ga_{0.51}P$ matrix (lattice matched to GaAs) and the GaAs substrate was used to fabricate all these samples.

For dots of InP on InGaP/GaAs, we discussed some peculiarities – for instance, the evolution of the morphology, structure and optical properties of InP QDs by insertion of GaP and InGaP layers. There were a few other interesting aspects of self-assembled InP QDs that unfortunately could not be succeeded in these works. These include

especially the influence of temperature, growth rate and V/III ratio. These are also important parameters on the size and density of quantum dots. In this work, these parameters changes could not give good result for InP QDs properties although these works were done under the same condition like other growth process.

Under the proper growth conditions, formation of InP dots via the Stranski-Krastanow mechanism was observed as already mention above. The critical InP coverage for 2D-3D transition was found to be 3 ML for the InP/$In_{0.48}Ga_{0.52}P$ system by MBE and 4 ML for the InP/ $In_{0.49}Ga_{0.51}P$ system by MOVPE. It was found from the structural characterization that the InP/$In_{0.48}Ga_{0.52}P$ QDs are larger and, consequently, high dense compared to the InP/$In_{0.48}Ga_{0.52}P$ QDs; hence, InP dots on InGaP tend to be strain-relaxed.

To characterize the structural properties of InP QDs, the AFM measurement was performed. Variation of the InP QDs size occurred due to the changes of the thickness of the GaP and InGaP insertion layers. Smaller dots and higher size distribution were generated when the dots density on the surface increased. The strain accumulation of the InP QDs had a strong influence on the quality of the GaP and InGaP insertion layers. Formation of the on the spacer layer was believed to be determined by the strain formed from the InP dots in the under-layer. The shape transition and size equalization of the InP QDs observed from the AFM characterization were also apparent in the photoluminescence PL spectra.

The different of the insertion layer thickness had influence on the morphology, structure and optical properties of InP QDs. Intense photoluminescence from InP quantum dots in InP/ $In_{0.49}Ga_{0.51}P$ system by MOVPE was observed. PL measurement was carried out using the 532 nm line of solid state laser. The PL signal was collected by an InGaAs photo-detector with a built-in preamplifier. The optical emission from dots is attributed to direct transitions between the electrons and heavy-holes confined in the InP dots. The PL from InP/InGaP QDs peaks between 770 and 810 nm mainly due to the different thickness of GaP and InGaP insertion layers. Blue-shift was observed by insertion of GaP and InGaP insertion layers. Generally, the PL intensity increased toward the thicker insertion layers.

The quality and quantity of the dots formation under the insertion of GaP and InGaP have a strong influence on the dots formation and the luminescence feature of the InP QDs structures. Most of the work had been done in MOVPE, in a few work also using MBE. Further progress in the effect of GaP and InGaP insertion layers will open the doors for completely new aspects of InP QDs nanostructures. This ability to control size and density of InP QDs GaP and InGaP insertion layers will be useful for employing as quantum dots. Also, further investigation on the influence of GaP and InGaP insertion layers on the phosphide material quality can be useful to realize higher performances of the single InP QDs. It can be consider as an interesting task for future work. In the future, one can think of a single quantum dot (QD) device for coding in computer and networking application. Therefore, optically or electrically addressable single QDs are needed on a mass production scale due to several advantages.

REFERENCES

[1] Carcia, J.M. and others **Appl. Phys. Lett.** 115 (1997): 2014.

[2] Eberl, K. Quantum-dot Lasers, **Physics World**: 10 (1997): 47.

[3] Arakawa, Y. and Sakaki, H., **Appl. Phys. Lett.** 40 (1982): 939.

[4] Asada, M., Miyamoto, Y. and Suematsu, Y. **IEEE J. Quantum Electron** QE-22 (1986): 1915-1912.

[5] Mitin, V., Kochelap, V. and Stroscio, M.: Quantum Heterostructures. **Cambridge: Cambridge University Press**, 1999.

[6] Bimberg, D., Grundmann, M., and Ledentsov, N., the quantum dot heterostructures.:**Wiley**, 1999.

[7] Ribeiro, E., Maltez, R. L., Carvalho, W., Jr., Ugarte, D. and Medeiros-Ribeiro, G., Optical and structural properties of InAsP ternary self-assembled quantum dots embedded in GaAs, **Appl. Phys. Lett.** 81 (2002): 2953-2955.

[8] Den-Baars, S.P., Reaves, C.M., Bressler-Hill, V., Varma, S., Weinberg, W.H. and Petroff, P.M. **J. Cryst. Growth** 145 (1994): 721.

[9] Tsang, W. T. **J. Cryst. Growth** 120 (1992):1.

[10] Thompson, A. G., Stall, R. A., Kroll, W., Armour, E., Beckham, C., Zawadzki, P., Aina, L. and Siepel, K. **J. Cryst. Growth** 170 (1997): 92.

[11] Richter, D and others **Appl. Phys. Lett.** 97 (2010): 63107.

[12] Zwiller, V. and others **Appl. Phys. Lett.** 78 (2001): 2476.

[13] Ren, H.-W., Nishi, K., Sugou, S., Sugisaki, M. and Masumoto, Y. **Jpn. J. Appl. Phys.** 36 (1997): 4118.

[14] Leonard, D. Pond, K. and Petroff, P.M. **Phys. Rev. B** 50 (1994):11687.

[15] DenBaars, S. P., Reaves, C. M., Bressler-Hill, V., Krishnamurthy, M. and Weinberg, W.H. **J. Cryst. Growth** 145 (1994): 721.

[16] Carlsson, N., Georgsson, K., Montelius, L., Samuelson, L., Seifert, W. and Wallenberg, R. **J. Cryst. Growth** 156 (1995): 23.

[17] Cui, J., He, Q., Jiang, X.M., Kawazu, T. and Sakaki, H. **Jpn. J. Appl. Phys.** 83 (2003): 2907.

[18] Carcia, J.M. and others **Appl. Phys. Lett.** 115 (1997): 2014.

[19] Cui, J., He, Q., Jiang, X.M., Kawazu, T. and Sakaki, H. **Jpn. J. Appl.Phys.Lett.** 83 (2003): 2907.

[20] Kobayashi, S., Jiang, C., Kawazu, T. and Sakaki, H. **Jpn. J. Appl.Phys.Lett.** 43 (2004): 662.

[21] Jackson, E.D., Trans. Conf. on the Use of Solar Energy, 5, **Univ. of Arizona Press, Tucson,** pp 122 :1955.

[22] Ren, H-W, Sugisaki, M., Lee, J-S, Sugou, S. and Masumoto, Y. **Jpn. J. Appl. Phys.** 38 (1999): 507.

[23] Aharonov, Y. and Bohm, D. **Physics Review** 115 (1959): 485.

[24] Bimberg, D., Grundmann, M., and Ledentsov, N. The quantum dot heterostructures: **Wiley**: 1999.

[25] Bimberg, D., Grundmann, M. and Ledentsov, N.N. Quantum Dot Heterostructures, **John Wiley & Sons**: Chichester: 1998.

[26] Arakawa, Y., Someya, T. and Tachibana, K. **Progress in Growth and Physics of Nitride-Based Quantum Dots**: 1982.

[27] Goronkin, H., Allmen, P., Tsui, R., Zhu, T. **Functional Nanoscale Devices**: ch.5.

[28] Rafailov, E. U., Cataluna, M. A. and Sibbett, W. Mode-locked quantum-dot lasers, **Nat. Photonics** 1(7) (2007): 395.

[29] Lu, Z. G. and others, Ultra-broadband quantum-dot semiconductor optical amplifier and its applications, **The Proceedings of the Optical Fiber Communication Conference, Anaheim, CA, USA**, pp JThA33: 2007.

[30] Brenot, R. and others, Quantum dots semiconductor optical amplifier with 3-dB bandwidth of up to 120 nm in semi-cooled operation, **The Proceedings of the Optical Fiber Communication Conference, San Diego, CA, USA**, pp OTuC1: 2008.

[31] Tanaka, Y. and others, High-speed and temperature-insensitive operation in 1.3-μm InAs/GaAs highdensity quantum dot lasers, **The Proceedings of the Optical Fiber Communication Conference, San Diego, CA, USA**, pp OWJ1: 2009.

[32] Liu, G. T., Stintz, A., Li, H., Malloy, K. J. and Lester, L. F. Extremely low room-temperature threshold current density diode lasers using lnAs dots in In0.05Ga0.85As quantum well, **Electron. Lett.** 35 (1999): 1163.

[33] Zilkie, A. J. and others, Femtosecond gain and index dynamics in an InAs/InGaAsP quantum dot amplifier operating at 1.55 microm, **Opt. Express** 14 (2006): 11453.

[34] Huang, X. D., Stintz, A., Li, H., Lester, F., Cheng, J. L. and Malloy, K. J. Passive mode-locking in 1.3 μm twosection InAs quantum dot lasers, **Appl. Phys. Lett.** 78 (2001): 2825.

[35] Renaudier, J. and others, 45 GHz self-pulsation with narrow linewidth in quantum dot Fabry-Perot semiconductor lasers at 1.5 μm, **Electron. Lett.** 41 (2005): 1007.

[36] Heck, M. J. R. and others, Observation of Q-switching and mode-locking in two-section InAs/InP (100) quantum dot lasers around 1.55 mum, **Opt. Express** 15 (2007): 16292.

[37] Lu, Z. G., Liu, J. R., Raymond, S., Poole, P. J.,. Barrios, P. J and Poitras, D., 312-fs pulse generation from a passive C-band InAs/InP quantum dot mode-locked laser, **Opt. Express** 16 (2008): 10835.

[38] Lu, Z. G., Liu, J. R., Raymond, S., Poole, P. J., Barrios, P. J. and Poitras, D., Femtosecond pulse generation in a Cband quantum dot laser," **The Proceedings of SPIE: Optoelectronic Materials and Devices III** (edited by Yi Luo, Jens Buus, Fumio Koyama, and Yu-Hwa Lo), 7135 (2008): 71352.

[39] Tang, X. F., Cartledge, J. C., Shen, A., Akrout, A. and Duan, G. H. Low-timing-jitter all-optical clock recovery for 40 Gbits/s RZ-DPSK and NRZ-DPSK signals using a passively mode-locked quantum-dot Fabry-Perot semiconductor laser, **Opt. Lett.** 34 (2009): 899.

[40] Jackson, E.D., Trans. Conf. on the Use of Solar Energy, 5, **Univ. of Arizona Press, Tucson**, pp 122: 1955.

[41] Wolf, M., **Proc. IRE** 48 (1960): 1246.

[42] Hutcuby, J.A., Markunas, R.J. and Bedair, S.M. **Proc. of the SPIE, Photovoltaics, S.K. Ded Ed.**, 543 (1985):. 543.

[43] Ludowise, M.J., LaRue, R.A., Borden, P.G., Gregory, P.E. and Dietz, W.T. **Appl. Phys. Lett.** 41 (1982): 550.

[44] Chung, B.-C., Virshup, G.E., Hikido, S. and Kaminar, N.R. **Appl. Phys. Lett.** 55 (1989): 1741.

[45] Ando, K., Amano, C., Sugiura, H., Yamaguchi, M. and Saletes, A. **Jpn. J.Appl. Phys.** 26 (1987): 266.

[46] Goldstein, L., Glas, F., Marzin, J. Y., Charasse, M. N., Roux, G. L. **Appl. Phys. Lett** 47 (1985): 1099.

[47] Ventra, M. D., Evoy, S. et al., **Introduction to nanoscale science and technology**: 2004.

[48] Matthews, J.W. and Blackslee, A.E. **J. Crystal Growth** 29 (1975): 273; 32 (1976): 265.

[49] Snyder, B.G. Orr, Kessler, D. and Sander, L.M. **Phys. Rev. Lett.** 66 (1991): 3032.

[50] Seifert, W., Carlsson, N., Miller, M., Pistol, M.-E., Samuelson, L., Wallenberg, L. R. **Prog. Crystal. Growth and charact** 33 (1996): 423.

[51] Walton, D., **J. Chem. Phys** 37 (1962): 2182.

[52] Kobayashi, N.P., Ramachandran, T.R., Chen, P. and. Madhukar, A **Appl. Phys. Lett.** 68 (1996): 3299.

[53] DenBaars, S. P., Reaves, S. P., Bressler-Hill, V., Varma, S, Weinberg, H. and Petroff, P. M. **J. Crystal Growth** 145 (1994): 721.

[54] Carlsson, N., Seifert, W., Petersson, A., Castrillo, P., Pistol, M.-E. and Samuelson, L. **Appl. Phys. Lett.** 65 (1994): 3093.

[55] Sopanen, M., Lipsanen, H. and and Shitara, J. **Appl. Phys. Lett.** 67 (1995): 3768.

[56] Kurtenbach, A., Eberl, K. and Shitara, T. **Appl. Phys. Lett.** 66 (1995): 361.

[57] Matthews, J. W. Epitaxial growth, **Chapter 8, Academic Press, New York**: 1975.

[58] Ahopelto, J., Lipsanen, H. and Sopanen, M.: **Proc. 7th Indium Phosphide and Related Materials**, pp 311: 1995.

[59] Angulo Barros, C. **J. Appl. Phys. Lett.** 92 (2002).

[60] Masafumi, Y., Okuda,T., Taylor,S.J., Takamoto,T., Ikeda,E. and Kurita,H. **Appl. Phys. Lett.** 70 (1997): 1566.

[61] Mattews J.W and Blakeslee A. E., **J.Crystal Growth** 27 (118): 1974

[62] Razeghi M., **The MOCVD Challenge Vol.2 Institute of Publishing Bristol and Philadelphia**: 1995.

[63] Schulz, W.-M., Roßbach, R., Reischle, M., Beirne, G. J., Bommer, M., Jetter, M. and Michler, P. **Phys. Rev. B** 79 (2009): 35329.

[64] Okuno, Y., Uomi, K., Aoki, M. and Tsuchiya, T. Direct wafer bonding of III-V compound semiconductors for free-material and free-orientation integration, **IEEE Quantum Electron.** 33 (1997): 959.

[65] Matthews, J.W. and Blakeslee, A.E., Defects in Epitaxial Multilayers.1. Misfit Dislocations **J. Crystal Growth** 27 (1974): 118.

[66] Matthews, J.W. and Blakeslee, A.E., Defects in Epitaxial Multilayers.2. Dislocations Pile-Ups, Threading Dislocation, Slip Lines and Cracks, **J. Crystal Growth**, 29 (1975): 273.

[67] Matthews, J.W. and Blakeslee, A.E., Defects in Epitaxial Multilayers.3.Preparation of Almost Perfect Multilayers, **J. Crystal Growth**, 32 (1976): 265.

[68] Burenkov, Y.A., et al., **Sov. Phys. Solid State**, 15 (1973): 1175.

[69] Nichols, D.N., Rimai, D.S. and Sladek, R.J. Elastic Anharmonicity of InP –Its Relationship to the High-Pressure Transition. **Solid State Communications**, 36 (1980): 667.

[70] Burenkov, Y.A., Davydov, S.Y. and Nikanorov, S.P. **Sov. Phys. Solid State** 17 (1975): 1446.

[71] Yogurtcu, Y., Miller, A. and Saunders, G. Pressure Dependent of Elastic Behavior and force constants of GaP, **J. Phys. Chem Solids** 42 (1981): 49.

[72] Black, K. A., Fused long-wavelength vertical cavity lasers, **Ph.D. Dissertation in Materials, University of California, Santa Barbara**: 2000.

[73] Pompe, W., Gong, X., Suo, Z. and Speck, J.S. **J. Appl. Phys.** 74 (1993): 6012.

[74] Borovitskaya, E. and Shur, M., Quantum dots., **World Scientific Publishing:** 2002.

[75] Ustinov, V. M., Zhukov, A. E., Egorov, A. Y., and Maleev, N. A. Quantum Dot Lasers. **Oxford Science Publications**: 2003.

[76] Ustinov, V. M., Zhukov, A. E., Egorov, A. Y., and Maleev, N. A. Quantum Dot Lasers**. Oxford Science Publications**: 2003.

[77] Heckmann, G. Die gittertheorie der festen korper, **Ergeb. Exakten. Naturwiss** 4 (1925): 100.

[78] Zhu, J., Liang, Z., Li, Y. R., Zhang, Y. and Wei, X. H. Epitaxial growth of BaTiO3 thin films at a low temperature under 300 ^{o}C with temperature-controlled BaTiO3 buffer layer **J. Crystal Growth** 294 (2006): 236.

[79] Robach, R., Schulz, W.-M., Reischle, M., Beirne, G. J., Jetter, M. and Michler, P. **J. Crystal Growth** 298 (2007): 595.

[80] Foo Cheng Yit, Fabrication of Monolithically Integrated Interferometer Switches by Selective Area MOVPE and their All-Optical Signal Processing Applications, **Ph.D thesis**: 2006.

[81] Mattews J.W and A.E.Blakeslee **J. Chrystal Growth** 27 (1974): 118.

[82] Stoltz W. **Compound Semiconductors** 5 (1999):.29.

[83] Tanaka, H., Kikkawa, T., Kasai, K. and Komeno, J. **Jpn. J. Appl. Phys.** 28 (1989): 901.

[84] Srivastava , G.P. and Jenkins, S. J. Atomic geometry and bonding on the GaAs (001) –beta 2(2 × 4) surface from ab initio pseudopotential calculations. **Phys. Review B** 53 (1996): 12589.

[85] Moll, N., et al., GaAs equilibrium crystal shape from first principles. **Physical Review B**, 54 (1996): 8844.

[86] Okuno, Y., Kawano, T., Study of threading dislocation reduction by strained interlayer in InP layers grown on GaAs substrates, **J. Crystal Growth** 145 (1994):.338.

[87] G. A. Fish, InGaAsP/InP based photonic integrated circuits for optical switching, **Ph.D. Dissertation in *Electrical and Computer Engineering*, University of California, Santa Barbara**: 1999

[88] Taub, M. ; Menzel, B. ; Khanna, G. ; Lilleodden, E., SPM Training Manual Version 2.0. Laboratory for Advanced Materials, **Stanford University**: 2003.

[89] Veeco Instruments Inc. (Hrsg.): **SPM training notebook. Veeco Instruments Inc.**: 2003.

[90] Pierret, R.F., **Advanced Semiconductor Fundamentals, Volume VI, Series Editor**.

[91] Fish, G. A., InGaAsP/InP based photonic integrated circuits for optical switching, **Ph.D. Dissertation in *Electrical and Computer Engineering*, University of California, Santa Barbara**: 1999.

[92] Singh, S. D., Sharma, T. K., Mukherjee, C. and Oak, S. M., **IEEE**, 978 (2007):. 1728.

ศูนย์วิทยทรัพยากร จุฬาลงกรณ์มหาวิทยาลัย

[93] Sormunen, J., Riikonen, J., Mattila, M., Sopanen, M. and Lipsanen, H. **IOP. Nanotechnology** 16 (2005): 1630.

[94] Barik, S., Tan, H. H. and Jagadish, C. **IEEE** 4244 (2006): 454.

[95] Ustinov, V.M, Maleev, N.A., Zhukov, A.E., Kovsh, A.R., Yu., A., Egorov, A.V. Lunev, B.V. Volovik, I.L. Krestnikov, Yu.G. Musikhin, N.A. Bert, P.S. Kop'ev, Z.h.I. Alferov, N.N. Ledentsov, D. Bimberg, **Appl. Phys. Lett.** 74 (1999): 2815.

[96] Zundel, M.K., Specht, P., Eberl, K., Jin-Phillipp, N.Y., Phillipp, F. **Appl. Phys. Lett.** 71 (1997): 2972.

[97] Gfroerer, T., **Photoluminescence in Analysis of Surfaces and Interfaces** [online] (n.d). Available from: http://webphysics.davidson.edu/faculty/thg/Welcome_files/EAC-PL.pdf [2008, October 2].

[98] Gammon, D. Quantum dots: An optical point of view, **Nature Physics** 3 (2007): 761.

[99] Purohit, V. **Photoluminescence spectroscopy: New technique for detecting explosives** [online] (n.d). Available from: http://www.buzzle.com/editorials/10-11-2004-60363.asp [2007, December 21].

[100] McQuarrie, D. A., Simon, J. D., **Physical Chemistry a molecular approach, University Science Books**: 1997.

[101] Chen, P., Xie, Q., Madhukar, A., Chen, L., Konkar, A. **J. Vac. Sci. Technol. B** 12 (1994): 2568.

[102] Solomon, G. S., Trezza, J. A., Harris, J. J S, **Appl. Phys. Lett**. 66 (1995): 991.

[103] Sopanen, M., Lipsanen, H., Ahopelto, J., **Appl. Phys. Lett.** 67 (1995): 3768.

[104] Welser, R. E., Guido, L. J., **Appl. Phys. Lett.** 68 (1996): 912.

[105] Johansson, J., Carlsson, N., Seifert, W. **Physica E** 2 (1998): 667.

[106] Seifert, W., Carlsson, N., Miller, M., Pistol, M.-E., Samuelson, L., Wallenberg, L. R, **Crystal. Growth and charact** 33 (1996): 423.

[107] Johansson, J., Seifert, W., Zwiller, V., Junno, T., Samuelson, L. **Appl. Surf. Sci.** 134 (1998): 47.

[108] Grundmann, M., **Physica E**, 5 (2000): 167.

[109] Mi´ci´c, OI, Sprague, JR, Lu, Z, Nozik, AJ., **Appl. Phys. Lett**, 68 (1996): 3150.

[110]Mi´ci´c, OI, Cheong, HM, Fu, H, Zunger, A, Sprague JR, et al., **J. Phys. Chem. B**: 1997.

[111]Fu, H, Zunger, A. **Phys. Rev. B** 55 (1997): 1642.

[112]Fu, H, Zunger, A. **Phys. Rev. B** 56 (1997): 1496.

[113]Nirmal, M, Norris, DJ, Kuno, M, Bawendi, MG, Efros, AL, Rosen, M., **Phys. Rev.Lett.**, 75 (1995): 3728.

[114]Efros, AL, Rosen, M, Kuno, M, Nirmal, M, Norris, DJ, Bawendi, M., **Phys. Rev. B** , 54 (1996): 4843.

[115]Empedocles, SA, Norris, DJ, Bawendi, MG., **Phys. Rev. Lett**., 77 (1996): 3873.

[116]Forchel, A., Steffen, R., Koch, T., Michel, M., Albrecht, M, Reinecke, TL. **Semicond. Sci. Technol.** 11 (1996): 1529.

[117]Gammon, D., Snow, ES, Katzer, D.S. **Appl. Phys. Lett.** 67 (1996): 2391.

[118]Grundmann, M., Christen, J., Ledentsov, N.N., Bohrer, J., Bimberg, D., et al., **Phys. Rev. Lett**. 74 (1995): 4043.

[119]Samuelson L, Carlsson N, Castrillo P, Gustafsson A, Hessman D, et al., **Jpn. J. Appl. Phys.** 34 (1995): 4392.

[120]Nagamune Y, Watabe H, Nishioka M, Arakawa Y **Appl. Phys. Lett.** 67 (1995): 3257.

[121]Ksharma, T. et.al. **J. Crystal Growth** 221 (2000): 509.

[122]Masafumi, Y., Takeshi, O., Stephen, J. T., Tatsuya, T., Eiji, I., and Hiroshi, K. **Appl. Phys. Lett.** 70 (1997): 1566.

[123]Carlsson, N., Seifert, W., Petersson, A., Castrillo, P., Pistol, M.-E. and Samuelson, L. **Appl. Phys. Lett**. 65 (1994): 3093.

[124]Leon, R., Lobo, C., Clark, A., Bozek, R., Wysmolek, A., Kurpiewski, A. and Kaminska. M., Different paths to tunability in III-V quantum dots., **J. Appl. Phys.** 84 (1998): 248.

[125]Johansson, J., Carlsson, N. and Seifert, W. Manipulations of size and density of self-assembled quantum dots grown by MOVPE. **Physica E** 2 (1998): 667.

[126]Oshinowo, J., Nishioka, M., Ishida, S. and Arakawa., Y. Area density control of quantum-size InGaAs/Ga(Al)As dots by metalorganic chemical vapor deposition **Jpn. J. Appl. Phys.** 33 (1994) Part2(11B):L1634–L1637.

[127]Xie, Q., Kobayashi, N.P.,. Ramachandran, T.M, Kalburge, A., Chen, P. and Madhukar., A. Strained coherent InAs quantum box islands on

GaAs(100): Size equalization, vertical self-organization and optical properties. **J. Vac. Sci. Technol. B** 14 (1996): 2203.

[128]Nabetani, Y., Sawada, K., Furukawa, Y., Wakahara, A., Noda, S. and Sasaki., A. Self-assembled InP islands grown on GaP substrate., **J. Crystal Growth** 193 (1998): 470.

[129]Saito, H., Nishi, K. and Sugou, S., Shape transition of InAs quantum dots by growth at high temperature., **Appl. Phys. Lett.**, 74 (1999): 1224.

[130]Ballet, P., Smathers, J.B., Yang, H., Workman, C.L. and Salamo, G.J. Scanning tunneling microscopy investigation of truncated InP/GaInP2 self-assembled islands. **Appl. Phys. Lett.** 77 (2000): 3406.

[131]Leon, R., Lobo, C., Zou, J., Romeo, T. and Cockayne, D.J.H. Stable and metastable InGaAs/GaAs island shapes and surfactantlike suppression of the wetting transformation. **Phys. Rev. Lett.**, 81 (1998): 2486.

[132]Okuno, Y., Kawano, T., Study of threading dislocation reduction by strained interlayer in InP layers grown on GaAs substrates **J. Cryst. Growth** 145 (1994): 338.

ศูนย์วิทยทรัพยากร
จุฬาลงกรณ์มหาวิทยาลัย

Vitae

Ms. Soe Soe Han was born in Kyaiklat, Ayeyarwaddy Divison, Myanmar, on 1st October, 1974. She received her first degree in B.Sc (Hons) Physics from Yangon University, 2000 and then continued studies in engineering physics leading to Master degree. She was received master degree in M.Sc (Eng) Physics from Yangon University in 2002. In October 2007, she was awarded a scholarship by AUN/SEED-Net to study at semiconductor device research laboratory (SDRL), Chulalongkorn University as a Ph.D student. Her interest and expertise are related to nanotechnology for III-V compound semiconductors, especially in fabrication and characterization of quantum dots.

<u>Conference Contributions</u>

1. **Soe Soe Han,** Somsak Panyakeow and Somchai Ratanathammaphan, "Effect of Thickness of GaP Ultra-thin Insertion Layer on the Structure Property of InP Quantum Dots", *Proceedings of Symposium O of the International Conference on Materials for Advanced Technologies (ICMAT 2009)*, Vol. 133, pp.176-178, December 2009.
2. **Soe Soe Han,** Somsak Panyakeow and Somchai Ratanathammaphan, "The Role of Thickness of GaP Ultra-thin Insertion Layer on Characterization of the Structure Property of InP Quantum Dots", *Proceedings of the 32th Thailand's National Electrical Engineering Conference*, Vol.1, pp.863-866, October 2009.
3. **Soe Soe Han,** Somsak Panyakeow and Somchai Ratanathammaphan, "Influence of Ultra-thin GaP Insertion Layer on the Structure of InP Quantum Dots Grown by Solid Source Molecular Beam Epitaxy", *Proceedings of the 1st International Conference on Science and Engineering (ICSE 2009)*, Vol.1, pp.12-15, December 2009.
4. **Soe Soe Han,** Somsak Panyakeow and Somchai Ratanathammaphan, Akio Higo, Wang Yunpeng, Momoko Deura, Masakasu Sugiyama, Yoshiaki Nakano, "Effect of GaP and $In_{0.4}Ga_{0.6}P$ Insertion Layers on the Properties of InP Nanostructures Metal-Organic Vapor Phase Epitaxy", *Proceedings of the 2st International Conference on Science and Engineering(ICSE 2010)*, Vol.1, pp.7-11, December 2010.